SAPIENZA
UNIVERSITÀ DI ROMA

Department of Mechanical and Aerospace Engineering

PhD degree in Theoretical and Applied Mechanics

2022

Microfluidic systems for artificial biological barriers

Supervisor: Prof. Carlo Massimo Casciola

Tutors: Dr. Giovanna Peruzzi
Dr. Giorgia Sinibaldi

Candidate: Giulia Grisanti

ISTITUTO ITALIANO
DI TECNOLOGIA
CENTER FOR LIFE NANO- & NEURO-SCIENCE

Contents

List of Figures

List of Abbreviations

2D	Two-Dimensional
3D	Three-Dimensional
AJs	**A**dherens **J**unctions
ATP	**A**denosine **T**riphosphate
BBB	**B**lood-**B**rain **B**arrier
BLMs	**B**lack **L**ipid **M**embranes
BSA	**B**ovine **S**erum **A**lbumin
CAD	**C**omputer-**A**ided **D**esign
CFD	**C**omputational **F**luid **D**ynamics
DC	**D**uty **C**ycle
DDS	**D**rug **D**elivery **S**ystems
DIC	**D**ifferential **I**nterference **C**ontrast
EBM	**E**ndothelial **B**asal **M**edium
ECs	**E**ndothelial **C**ells
ECFC-ECs	**E**ndothelial **C**olony **F**orming **C**ell-derived **E**ndothelial **C**ells
EE	**E**ncapsulation **E**fficiency
EGM	**E**ndothelial **G**rowth **M**edium
FBS	**F**etal **B**ovine **S**erum
FDA	**F**ood and **D**rug **A**dministration
F-MMM	**F**luid-**M**osaic **M**embrane **M**odel
FRAP	**F**luorescence **R**ecovery **A**fter **P**hotobleaching
FRET	**F**örster **R**esonance **En**ergy **T**ransfer
GJs	**G**ap **J**unctions
GUVs	**G**iant **U**nilamellar **V**esicles
HFF	**H**ydrodynamic **F**low **F**ocusing
HIFU	**H**igh **I**ntensity **F**ocused **U**ltrasound
HMEC-1	**H**uman **M**icrovascular **E**ndothelial **C**ells-1
HMVEC-ad	**H**uman **a**dult **d**ermal **M**icrovascular **E**ndothelial **C**ells

HUVECs	**H**uman **U**mbilical **V**ascular **E**ndothelial **C**ells
JAIL	**J**unction-**A**ssociated **I**ntermittent **L**amellipodia
LoC	**L**ab-**o**n-**C**hip
LUVs	**L**arge **U**nilamellar **V**esicles
MBs	**M**icro**b**ubbles
MEMS	**M**icro **E**lectro-**M**echanical **S**ystems
MI	**M**echanical **I**ndex
MLVs	**M**ulti **L**amellar **V**esicles
MPS	**M**icro**p**hysiological **S**ystems
μTAS	**micro**-**T**otal **A**nalysis **S**ystems
NHLFs	**N**ormal **L**ung **H**uman **F**ibroblasts
NO	**N**itric **O**xide
OLVs	**O**ligo**L**amellar **V**esicles
OoC	**O**rgan(s)-**o**n-**C**hip
PBS	**P**hosphate **B**uffer **S**aline
PD	**P**ulse **D**uration
PDF	**P**robability **D**ensity **F**unction
PDMS	**P**oly(**dim**ethyl**s**iloxane)
PEB	**P**ost **E**xposure **B**ake
PEG	**P**oly**e**thylene **G**lycol
PFA	**P**ara**f**orm**a**ldehyde
PGMEA	**P**ropylene **G**lycol **M**onomethyl **E**ther **A**cetate
PI	**P**ropidium **I**odide
PID	**P**roportional **I**ntegral **D**erivative
PM	**P**lasma **M**embrane
POPC	1-**P**almitoyl-2-**O**leoyl-*sn*-glycero-3-**P**hospho**c**holine
PRF	**P**ulse **R**epetition **F**requency
PVA	**P**oly**v**inyl **A**lcohol
REM	**Re**plica **M**oulding
ROI	**R**egion **O**f **I**nterest
ROS	**R**eactive **O**xygen **S**pecies
RT	**R**oom **T**emperature
SLBs	**S**upported **L**ipid **B**ilayers
SUVs	**S**mall **U**nilamellar **V**esicles
TC	**T**issue **C**ompartment
TI	**T**hermal **I**ndex
TJs	**T**ight **J**unctions
TMC	**T**rans**M**embrane **C**urrent

TME	**T**umour **M**icro**E**nvironment
TNS	**T**rypsin **N**eutralising **S**olution
UCAs	**U**ltrasound **C**ontrast **A**gents
US	**U**ltra**s**ound
UV	**U**ltra**v**iolet
VC	**V**ascular **C**hannel
VE-Cadherin	**V**ascular **E**ndothelial-Cadherin
VECs	**V**ascular **E**ndothelial **C**ells
W/O	**W**ater-in-**O**il
W/O/W	**W**ater-in-**O**il-in-**W**ater

Chapter 1

Introduction

The efficacy of therapeutic strategies is not only based on their specific activity against diseases, but also on their selectivity in targeting the pathological district of the organism. Traditional therapeutic approaches are based on drug even distribution within the body, mostly through the cardiocirculatory route. This entails the interaction of the pharmaceutical agent with the biological barriers of the organism, i.e. specialised structures regulating the exchanges between different compartments of the living systems and preventing the passage of exogenous molecules [1]. Among them, the endothelial barrier is composed of a compact monolayer of endothelial cells (ECs) lining the internal lumen of blood vessels [2]. ECs are tightened together by interendothelial junction complexes, where the adhesion protein vascular endothelial (VE)-cadherin accounts for direct contact between adjacent cells and is thus mostly responsible for the barrier activity [3, 4]. Given its organisation, the endothelium is one of the main obstacles to drug accumulation at the target site. Moreover, once in the pathological tissue, pharmaceutical agents need to interact with another barrier, i.e. the plasma membrane (PM). It is mainly composed of lipid molecules, organised in a continuous bilayer that encloses cell interior and metabolic processes, isolating them from the surrounding environment and regulating the passage of substances. Cell membrane is a highly dynamic structure, whose functioning is deeply associated with its biomechanical features [5, 6]. Such a complex scenario implies two main risks for therapeutic approaches: either drugs undergo chemical modifications and inactivation, or they accumulate in other districts of the organism, where they can provoke off-target side effects. As a result, since only a small drug amount does reach the target side, greater doses need to be administered in

order to obtain the therapeutic effect. This, in turn, might raise the risk of causing undesirable side effects [1].

Pharmaceutical research has addressed these issues through the development of targeted drug delivery systems (DDS), i.e. strategies and formulations aimed at controlling drug pharmacokinetics and biodistribution, to maximise drug transport to the pathological site and increase its therapeutic effect, also allowing the administration of smaller doses [7, 8, 9]. Since Paul Ehrlich's first theorisation of the "magic bullet" concept, according to which drugs can be directed straight to their target site, advancement in pharmacology has brought to the development of different drug delivery strategies [10, 11]. They include methods to increase the permeability of biological barriers [12], such as cavitation, i.e. bubble nucleation in a fluid due to pressure decrease (homogeneous cavitation) and to the presence of inhomogeneities (heterogeneous cavitation) [13]. Heterogeneous cavitation can be induced in biological tissues through the oscillatory pressure generated by ultrasound (US), currently employed in clinics for imaging, diagnostic and therapeutic purposes. The microbubbles (MBs) used as ultrasound contrast agents (UCAs) in imaging, which are air- or gas-filled micrometre-sized bubbles covered by a stabilising lipid shell, sense the acoustic pressure and oscillate in accordance with the acoustic field [14]. This further favours cavitation occurrence (USMB-mediated cavitation) and exerts a mechanical stress on biological barriers. In particular, USMB-induced bioeffects determine the reorganisation of membrane lipids, causing the opening of pores on cell surface [15, 16], as well as the rearrangement of interendothelial junction complexes, leading to a temporary and reversible increase in endothelial permeability [17]. USMB-mediated cavitation has thus gained increasing attention as an effective strategy to enhance endothelial permeability and drug delivery efficiency [18].

In this context, *in vitro* experimental models faithfully reproducing biological barriers are required to characterise their features, with a particular focus on their biomechanics, and recapitulate their behaviour. In particular, endothelial monolayers have been so far obtained through two-dimensional (2D) traditional cell cultures techniques. However, they lack biological relevance as they do not include some stimuli, e.g. mechanical cues like the shear stress, which have been proven crucial for the maturation of a functioning barrier [19, 20]. Among PM models, giant unilamellar vesicles (GUVs) are vesicular models ($10 - 100\,\mu$m in diameter) with adjustable size and composition, which mimic cell membrane features [21]. They are particularly useful

for the characterisation of membrane biomechanics and rigidity, described by the bending rigidity modulus κ, which influences membrane response to external mechanical stimuli [22]. Microfluidics, consisting in fluid manipulation at the microscale within micro-sized devices of customisable geometries, provides a cost-effective, easy to handle and versatile technology for the realisation of such models [23]. Microfluidic platforms offer a confined microenvironment where the experimental conditions can be finely tuned in terms of flow rates as well as mechanical and chemical properties [24]. Within these platforms, cells can be cultured to realise three-dimensional (3D) endothelial models, possibly entailing flow-induced shear stress to recreate physiological-like conditions [25]. Analogously, membrane models such as GUVs can be produced through microfluidics, with precise control over their composition as well as over biochemical and biomechanical features [26, 27].

The goal of this PhD project consists in employing two microfluidic systems for the realisation of these biological models, i.e. an endothelial layer and GUVs. The aim of the first experimental model concerns the investigation of the endothelial dynamic response to USMB-mediated cavitation, while the second platform is intended for high-throughput production of GUVs as an experimental model of phospholipid bilayers, for the successive characterisation of some biomechanical properties.

As far as the endothelial model is concerned, previous work from our group led to the realisation of a blood vessel-on-chip model, recapitulating physiological-like conditions, to investigate the effects of its exposure to US in presence or in absence of MBs [28, 29]. The resulting cavitation phenomena are indeed shown to crucially affect VE-cadherin organisation, leading to endothelial permeabilisation through the opening of interendothelial gaps. In the present work, this effects will be initially investigated in a "static" way, through immunofluorescence assays performed after the end of the insonation. Endothelial permeabilisation will be quantitatively evaluated through an image analysis code for interendothelial gap identification and measurement. Moreover, since endothelial permeabilisation has been proven to be transient and reversible, with the full recovery of barrier integrity, attention will be successively paid to the time scale of this process. The aim is to investigate the early events after the exposure to US and characterise the dynamics of interendothelial junctions opening and closure. For this purpose, the blood vessel-on-chip system will be adapted for the real-time characterisation of cell response to USMB-induced mechanical stimuli. This is achieved using a genetically modified ECs population, expressing flu-

orescent VE-cadherin. The developed system, mimicking blood vessel physiological characteristics, will be employed to follow VE-cadherin and junction dynamics over time, in response to endothelial exposure to US in presence or in absence of MBs.

In parallel, the other aim of this PhD project is to develop a microfluidic system for GUVs production. This will involve the choice of a suitable geometry to allow controlled interactions among three immiscible solutions for the formation of a water-in-oil-in-water (W/O/W) double emulsion [27]. Indeed, this template allows phospholipid molecules to organise into a continuous bilayer enclosing an aqueous environment, ultimately forming GUVs. This project is intended to design and test the microfluidic platform as well as the experimental protocol. The composition of the three solutions will be initially determined for the formation of stable vesicular systems and for the extraction of oil residues from the phospholipid bilayer. Then, the microfluidic protocol will be established, identifying suitable flow rate values for vesicle formation. The GUVs obtained through this approach will be initially characterised with optical microscopy. An image acquisition protocol is thus to be established, in light of the next characterisation of membrane biomechanical properties through thermal fluctuation analysis.

The present PhD thesis offers a theoretical overview of the different topics mentioned so far, together with the detailed description of the experimental work that was carried out. Chapter 2 describes biological barriers, focusing on the PM and on the vascular endothelium, from a biological, chemical and mechanical viewpoints. Moreover, information about experimental models reproducing PM features will be provided. In Chapter 3, the basic principles and physics of cavitation are reported, along with the description of MBs and their interaction with US. The effects of these interactions on biological barriers and how they are exploited to enhance drug delivery are also discussed. Chapter 4 is devoted to the description of microfluidics and its employment in biomedical research. In particular, an overview is provided on microfluidic platforms for the realisation of biological barrier models, i.e. the endothelium and the PM. Moving from this theoretical background, Chapter 5 is focused on the experimental work for this PhD project, with the description of the blood vessel-on-chip model and of the microfluidic platform for GUVs production. Initially, the soft lithography technique for the fabrication of the microfluidic devices is presented. The successive section provides a thorough description of the USMB-mediated cavitation experiments, carried out to en-

hance the permeabilisation of the endothelial barrier and its dynamics. The relative results are presented and discussed. The last part of Chapter 5 is devoted to illustrate the experimental set-up developed for the realisation of GUVs through microfluidics, with the obtained results. Finally, in Chapter 6 the presented project is summarised and some possible future developments are pointed out and discussed.

Chapter 2

Biological barriers: structure, mechanical properties and biological relevance

The definition of biological barriers is deeply related to their function in living organisms. They guarantee compartmentalisation in cells, tissues and organs, separating their internal from the external environment, as well as different areas within the same biological entity. Yet still, they also allow communications between the areas they isolate, thanks to their capability to control the passage of substances by highly selective transport routes. Their role is crucial for cell/tissue integrity and homeostasis [30, 31].

Their biological structure accounts for their crucial functions, as it will be discussed throughout this chapter.

2.1 The plasma membrane

2.1.1 Plasma membrane structure and functions

The plasma membrane (PM) is the biological barrier constituting the outer boundary of living cells. With its thickness ranging from 5 to 10 nm [32], it plays the crucial role of enclosing and isolating cell metabolism and biochemical processes from the surrounding environment, while still allowing interactions with it [31].

PM is shortly defined as a lipid bilayer with embedded proteins; it is

sketched in Fig. 2.1A. Indeed, its main structural component is represented by lipid molecules, mostly phospholipids (Fig. 2.1B). They are composed of a hydrophilic "head", consisting in a phosphate group linked to another polar group (most commonly choline, ethanolamine or inositol), and two hydrophobic "tails" of fatty acid chains (acyl chains). These can show variable

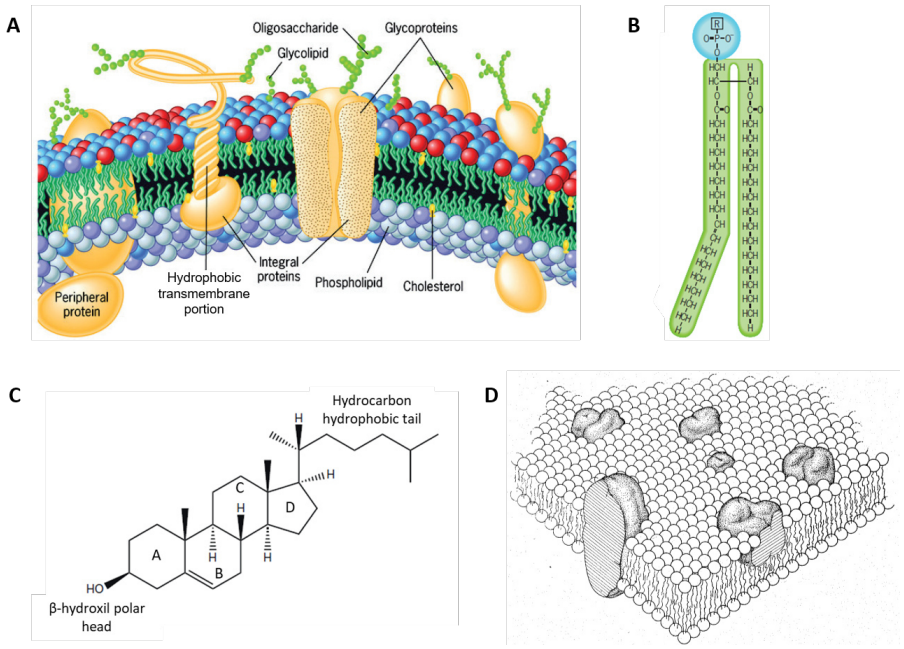

Figure 2.1: **Plasma membrane and its constituents. A.** Sketch of the PM structure, described as a phospholipid bilayer with embedded proteins. Proteins interacting with the bilayer can be transmembrane (integral) or peripheral. Carbohydrates (oligosaccharides) are another PM component and can be attached to proteins (glycoproteins) or lipids (glycolipids). Modified from [31]. **B.** Phospholipids structure. The hydrophilic "head" comprises a phosphate group connected to a polar "R" group of different kinds (details are in the main text). The hydrophobic "tail" is composed of two fatty acid chains (acyl chains), which can differ in length and number of unsaturated bonds. Modified from [31]. **C.** Cholesterol is constituted by the steroid ring system of 4 fused carbon rings (from A to D), which is linked to a hydrophobic hydrocarbon tail and to a hydrophilic hydroxyl group. Modified from [33]. **D.** The Fluid-Mosaic Membrane Model proposed by Singer and Nicolson in 1972, describing cell membrane as a two-dimensional fluid phospholipid bilayer with embedded and associated proteins. Taken from [34].

lengths and be either saturated or unsaturated - the latter having one or more double bonds between the carbons of the chain [34, 35]. Cholesterol is another fundamental lipid constituting the PM of mammalian cells. Rigid and planar, it is composed of 4 fused carbon rings (named from A to D), the steroid ring system, which is linked, on one side, to a short non-polar hydrocarbon tail and, on the other side, to a polar hydroxyl group, as shown in Fig. 2.1C [33, 36].

The lipids composing the PM are amphiphatic molecules. This characteristic is crucial for membrane structure and function. Indeed, since both the extracellular and intracellular environments are hydrophilic, lipid molecules self-assemble to minimise energetically unfavourable interactions between the hydrophobic fatty acid chains and the surrounding water molecules. This results in the formation of two lipid leaflets (layers) one against the other, with the heads directed outward, in contact with the polar environment, whereas the acyl chains are isolated in the internal structure [35, 31]. According to the thermodynamics of this system, cholesterol molecules are embedded in the membrane, with the planar steroid ring system parallel to fatty acid chains and the small polar head oriented toward the aqueous surroundings [33, 37, 38].

Proteins are the other fundamental component of PM [39]. They can be associated with its surface on either side (i.e. peripheral proteins), or directly inserted within the lipid bilayer (i.e. integral or transmembrane proteins). Their presence is crucial for several membrane functions, such as signal transduction, cell-cell interactions as well as transport of molecules and compounds across the PM [5, 34].

Finally, carbohydrates interact with the membrane surface on both sides and are mostly linked to membrane proteins [40, 41, 42].

PM molecular arrangement, mostly based on non-covalent interactions, was firstly described by the Fluid-Mosaic Membrane Model (F-MMM), see Fig. 2.1D, proposed by Singer and Nicolson in 1972 [34], which was successively integrated with new experimental evidence, resulting in the current accepted model [5]. According to it, cell membrane is a two-dimensional fluid system composed of a phospholipid bilayer with embedded proteins and associated carbohydrates. Lipid and protein compositions can differ between the two leaflets, resulting in an asymmetric membrane [5, 43, 44]. In this system, molecular lateral diffusion, albeit allowed, is restrained by the existence of confined domains within each leaflet. They are delimited by specific lipid-lipid and lipid-protein interactions, as well as by the interaction of

membrane components with the extracellular matrix [45] and the cytoskeleton [46]. Membrane fluidity is mostly influenced by temperature and lipid composition. At higher temperatures (e.g. 37°C), the PM is fluid and appears as a liquid crystal where molecules are relatively free to move. Below a defined transition temperature, determined by membrane lipid composition, it shifts into a more static and packed crystalline gel. In this context, cholesterol alters fatty acid compactness. Hence, it accounts for an intermediate phase, which is ordered with regard to the acyl chain conformational structure and disordered in the lateral positions of the molecules. It has been defined as liquid-ordered phase, to distinguish it from the liquid-disordered (fluid) phase [5, 47, 48].

The complex and compact structure of PM accounts for its barrier function. Indeed, it prevents the spontaneous and indiscriminate passage of substances. Only certain molecules are allowed to cross the bilayer, being specifically selected on the basis of their favourable interactions with membrane components. Hence, the PM is defined as a semipermeable barrier. Selective molecular transport across the membrane can be passive or active [49]. Diffusion is at the basis of passive transport and consists in the spontaneous movement of substances along their concentration gradient. Hydrophobic molecules or small ions directly pass through the phospholipid bilayer (simple diffusion). Polar or bigger substances are recognised by PM protein transporters, which form transmembrane channels to favour molecular passage (facilitated diffusion). Active transport, on the other hand, implies energy consumption to move substances against their concentration gradient. This is accomplished by energy-driven protein "pumps", which couple molecular transport with the hydrolysis of highly energetic phosphate bonds of adenosine triphosphate (ATP) [50, 51, 52]. Furthermore, cells are able to take up substances from the surrounding environment through less specific and multi-step mechanisms, such as endocytosis [53, 54]. It begins with the formation of a budding structure from the PM, which progressively invaginates until a membrane vesicle detaches inside the cell. This implies the internalisation of extracellular fluids and molecules as well as of membrane proteins. Endocytosis is supported and regulated by several proteins interacting with the membrane, such as clathrin, which coats the vesicle surface (clathrin-mediated endocytosis). However, other pathways exist which are independent of the clathrin coat (clathrin-independent endocytosis), e.g. caveolar endocytosis [55].

2.1.2 Membrane energy and biomechanics: Helfrich's model

As a physical system, a certain value of free energy is associated with the membrane, resulting from its intrinsic properties and from its interactions with the surrounding environment. When forces exerted on the phospholipid bilayer are balanced, the system is at its equilibrium state, with the minimum value of free energy. Cell physiological processes or (external) mechanical stimuli perturb this state and affect membrane energy.

In 1973, Helfrich proposed a model to describe membrane free energy and its alterations, along with the related biomechanics [56]. According to this model, curvature is the only strain affecting membrane shape and free energy. Contributions from other kinds of strain related to phospholipid orientations and interactions, such as stretching (due to tangential stress) and tilt (due to torque densities exerted on lipid molecules), are considered transient or too small, respectively, hence negligible. Helfrich's model links the bilayer free energy to its shape, thus to its biomechanics, through the membrane curvature. Three different contribution are considered. The mean curvature of the membrane, H, is the actual curvature, determined by the configuration of the phospholipid molecules and the resultant of the forces exerted on the bilayer. The spontaneous curvature, C_0, is the mean curvature that minimises the free energy and results from the different chemical composition of the two leaflets [56]. Finally, the Gaussian curvature, K, is inherent to membrane bilayer, and, according to the Gauss-Bonnet theorem, it is a topological invariant. Hence, its value is constant as long as membrane topology does not change and it only accounts for drastic shape changes (e.g. from a sphere to a torus) which can occur during some cell processes, such as endocytosis [57, 58].
In particular, named R_1 and R_2 the principal radii of curvature of the membrane, mean and Gaussian curvatures are defined as:

$$H = \frac{1}{2}\left(\frac{1}{R_1} + \frac{1}{R_2}\right) \tag{2.1}$$

$$K = R_1 \cdot R_2 \tag{2.2}$$

Membrane curvature is linked to its free energy by the following relation [56]:

$$E = \sum_{i=1,2} \int \frac{1}{2} \left[\kappa \left(H - C_0 \right)^2 + \kappa_G K \right] dS_i + \sigma_i \left(\int dS - S_0 \right) + p_i \left(\int dV - V_0 \right) \tag{2.3}$$

In this equation, i denotes each phospholipid leaflet, which can differ between each other in terms of free energy, by virtue of membrane asymmetry. σ is the surface tension, p the turgor pressure, S_0 and V_0 stand for the membrane surface area and volume, respectively, under zero-stress conditions. dS and dV represent the area and the volume, respectively, of infinitesimal elements of the membrane; κ and κ_G are two curvature-elastic moduli with the dimensions of energy. κ_G is the saddle-splay modulus associated with the Gaussian curvature, accounting for the energy cost of saddle-like deformation. κ is the membrane bending rigidity modulus, which describes the cost, in terms of energy, of deviations from the spontaneous curvature, thus representing membrane rigidity [56].

κ is an important parameter for the description of bilayer biomechanical and chemical characteristic. Its value depends on membrane features and thermodynamic state, as well as on the surrounding environment [56, 59]. For instance, κ can be affected by membrane lipid composition, i.e. the nature of polar heads or the length and level of unsaturation of the acyl chains [60, 61, 62]. The presence of specific lipids, e.g. cholesterol [63, 64], or proteins [65] can also influence its value. Moreover, the characteristics of the surrounding environment, such as temperature variations [61, 63] and buffer composition [66, 67], have been reported to influence the value of this parameter.

2.1.3 Artificial membrane models for biomechanical investigations

Several experimental models have been created to reproduce and investigate PM characteristics in more controlled and simpler structures. Initially, symmetric membranes, i.e. with the leaflets having the same composition, were mostly synthesised exploiting lipid spontaneous self-assembling. Successively, research focused on the realisation of more realistic asymmetric bilayers [68, 69, 70].

A first classification can be made distinguishing between planar and vesic-

ular lipid bilayer systems. Among planar membrane models, supported lipid bilayers (SLBs) results from the deposition of a lipid bilayer onto an inorganic support, in direct contact with it [71, 72] or separated by an ultrathin polymer cushion [73]. Maintaining the thermodynamics and the structural properties of a free bilayer [74, 75, 76], SLBs have been used for surface functionalisation, for protein reconstitution within the bilayer, as well as for investigations on molecular diffusion and interactions [73, 74, 77, 78, 79]. Pore-spanning lipid bilayers are another model system, most often used for biomechanical investigations. They consist in a lipid bilayer spread over a highly porous support to obtain portions of free membrane suspended on nano-sized pores (nano-black lipid membranes - BLMs). Their main advantage is that they allow easier measurements of membrane bending and stretching [80, 81, 82].

Vesicular model systems, on the other hand, represent an extremely versatile tool to reproduce membrane characteristics. They find important appli-

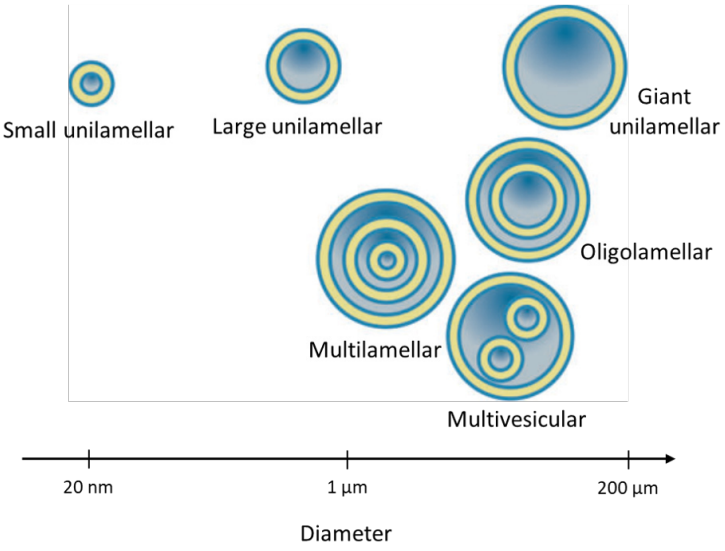

Figure 2.2: **Classification of vesicular membrane model systems.** Vesicular membrane models can be classified according to their lamellarity and size. Based on the first criterion, unilamellar, oligolamellar and multilamellar vesicles are distinguished. Unilamellar vesicles can be classified as small ($20 - 100\,\mathrm{nm}$), large ($100\,\mathrm{nm} - 1\,\mu\mathrm{m}$) or giant ($10 - 100\,\mu\mathrm{m}$), depending on their size. Multivesicular systems are formed by several non-concentric vesicles encapsulated within a single bilayer vesicle. Adapted from [84].

cations in several fields, including biomechanics and biomedicine. As shown in Fig. 2.2, they can be classified on the basis of two different criteria, namely lamellarity and size [83, 84]. Lamellarity refers to the number of concentric bilayers (*lamellae*) composing the vesicles, and accounts for the distinction among unilamellar, oligolamellar (OLVs, $2-5$ bilayers) and multilamellar (MLVs, >5 bilayers) vesicles. According to their size, unilamellar vesicles are further classified into small unilamellar vesicles (SUVs, $20-100\,\mathrm{nm}$), large unilamellar vesicles (LUVs, $0.1-1\,\mu\mathrm{m}$) and giant unilamellar vesicles (GUVs, $10-100\,\mu\mathrm{m}$) [83, 21]. MLVs, SUVs and LUVs can be also referred to as liposomes (from Greek *lipos* = fat, lipid; *soma* = body), while other authors (e.g. [85]) consider the word liposome as a synonym of spherical lipid vesicle. On the other hand, the nomenclature of "Giant Vesicles" was used for the first time at the end of the 1970s [86].

For their smaller size, liposomes (MLVs, SUVs, LUVs) have been widely employed in pharmaceutical and clinical fields, for example as drug carriers [87]. On the contrary, GUVs are more suited for the reproduction of membrane characteristics for several purposes, including biomechanical investigations [22]. However, in recent years, potential for innovative employment of GUVs for drug delivery applications came to light, as it will be discussed in § 2.3.

GUVs as artificial models of cell membranes

GUVs are widely employed in research for their advantageous features. With a bilayer thickness of approximately $4-5\,\mathrm{nm}$ and diameter ranging from 10 to $100\,\mu\mathrm{m}$, they match the cell-size scale and represent a valid tool to resemble physiological membranes [21, 88]. Once formed, they are stable for a period of time ranging from a few days [85] up to three months [89]. Moreover, they can be easily handled and observed through optical microscopy, also for real-time monitoring. Indeed, label-free techniques, such as phase-contrast and differential interference contrast (DIC) optical microscopy, can be used to enhance image contrast to optimise membrane visualisation [90, 91]. GUVs can be also investigated with fluorescence microscopy approaches [92, 93], including wide-field [94] and confocal [95] microscopy, as well as fluorescence correlation spectroscopy [96], laser scanning [97], Förster resonance energy transfer (FRET) [95, 98] and fluorescence recovery after photobleaching (FRAP) [99]. Either fluorescent lipids can be directly incorporated in the bilayer or fluorescent probes, e.g. DiIC_{20} or LAURDAN, can be associated to the formed

GUVs membrane [96, 100, 101].

Another element of GUVs versatility is related to their variable composition, which can be modified by including different kinds of lipids (either natural or synthetic), also in different proportions, in the production process. This allows to adjust membrane biophysical and biomechanical features and to investigate the contribution of different lipids to the PM characteristics [88]. For example, cholesterol has been reported to differentially interact with fatty acid chains of phospholipids (e.g. unsaturated glycero-phospholipids and sphingomyelin), leading to distinct packing and conformational changes, which resulted in modified lipid diffusion coefficients, also depending on cholesterol amount [102].

Such a flexibility can be further increased with the inclusion of proteins, which can be either loaded within the GUVs aqueous internal compartment or associated with the GUVs bilayer [103]. In the first case, the reconstitution of functional cytoskeletal proteins has been successfully accomplished [104, 105, 106]. Likewise, both peripheral and transmembrane bilayer-associated proteins have been successfully reconstituted into GUVs, recapitulating their biological activity upon interaction with the lipid membrane [107, 108], even distinguishing areas with different curvatures [109].

Given their versatility, GUVs have been exploited as biomimetic tools, to study compartmentalisation and cellular crowding [110, 111], to be used as microreactors [112, 113], up to the possibility to recreate an artificial cell [114, 115, 116]. However, GUVs main applications pertain the investigation on membrane features and interactions, as well as on their biomechanical and rheological properties [22, 117]. As far as membrane biomechanics is concerned, GUVs have been employed to characterise membrane curvature and elastic properties, with particular focus on the modulus κ [22, 118]. For this purpose, a simple and commonly used method is based on micropipette aspiration [119, 120], exploiting a gas capillary to exert a suction pressure on the membrane. This generates mechanical tension and subsequent area variations, that are mathematically linked to κ.

Another widespread technique to assess membrane rigidity is the thermal fluctuation analysis [121, 122, 123]. It is a simple and non-demanding approach consisting in acquiring a series of snapshots of the vesicle over time to observe the lipid bilayer fluctuations, implying low membrane tension. The analysis focuses on the extraction of the vesicle contours and in their Fourier decomposition, to calculate the mean square values of shape deviations. Being such membrane deformations dependent on the temperature

and on the mechanical properties of the lipid bilayer, κ can be extracted from this procedure [22, 124].

2.2 The vascular endothelium

Among the biological barriers of human organism, the vascular endothelium is the tissue lining the lumen of all blood vessels of the vascular tree, in direct contact with the blood stream. It is composed of a thin and uniform layer of specialised epithelial cells, the endothelial cells (ECs), supported by a basal lamina. In the vascular system, the endothelium plays a fundamental role in the homeostasis of blood vessels, being involved in vasodilation and vasoconstriction, coagulation, inflammation, and immune response. Its barrier function is particularly evident in capillary vessels, where the endothelium acts as a selective, semipermeable barrier, allowing the bidirectional passage of specific substances (nutrients, gas, signalling molecules, even cells) while hindering it to potentially harmful or toxic molecules, e.g. drugs [2, 125, 126].

Such a fundamental function is deeply linked to its structure and organisation. Indeed, ECs are connected and compacted by interendothelial junction complexes, which tighten the cells in an impermeable monolayer [127]. Interendothelial junctions can be classified according to their functional characteristics:

- **Adherens junctions (AJs).** AJs are ubiquitous in the vascular tree, where they are the prevalent kind of junction, and are constituted by several proteins, including adhesion proteins of the cadherin family [128]. Among these, the major AJs component is the vascular endothelial (VE)-cadherin, specific of the endothelial tissue and regulating its integrity and permeability [3, 4, 129].

- **Tight junctions (TJs).** TJs, predominant in small arterioles, mostly account for vascular impermeability, as they are composed of protein families (claudins [130], occludins [131], junctional adhesion molecules, JAMs [132]) that "seal" adjacent cells together, preventing molecular passage. As such, they are preferentially localised in specific body districts where they are fundamental to the establishment of a functional barrier, like in the case of blood-brain, gut-blood or blood-testis barriers. Analogously to AJs, TJs are also involved in several endothelial

signalling pathways, including mechanotransduction and regulation of cell growth [133, 134].

- **Gap junctions (GJs).** GJs are a kind of interendothelial junction mediating communication between adjacent cells [135]. Indeed, they consist in channels, made up of connexin proteins [136], that directly connect cell cytoplasms, allowing the passage of small molecules, including Ca^{2+} and other ions, as well as water molecules [127].

Adherens junctions are principally involved in endothelial permeability, accounting for tissue architectural integrity and making the endothelium a size-selective and semipermeable barrier, where molecular passage occurs through two well-characterised routes, the paracellular and transcellular (transcytotic) pathways [137]. Paracellular transport consists in substances diffusion across the endothelium upon AJs loosening and consequent opening of gaps between adjacent cell, due to VE-cadherin rearrangements. In this case, despite the lack of molecular specificity, the passage is limited to molecules with radii up to 3 nm [138, 139]. On the other hand, transcellular route involves the transport of material within a cell through energy-dependent vesicular trafficking. This process allows the passage of bigger molecules, e.g. albumin and albumin-bound ligands [140, 141], insulin, low density lipoproteins, and other hormones [142, 143, 144]. Being triggered upon specific ligand-receptors molecular recognition, this mechanism is more selective compared to the paracellular pathway [139, 145].

VE-Cadherin. VE-cadherin, the main protein regulating endothelial architecture and permeability, is preferentially localised within the intercellular junctional complexes [3]. It is a transmembrane protein, which establishes, on the extracellular side, Ca^{2+}-mediated homophilic contacts with other molecules on adjacent cells. On the other hand, its cytosolic portion is associated with scaffolding and signalling proteins, thus linking AJs to the cell actin cytoskeleton [146]. This configuration makes VE-cadherin and AJs highly dynamic structures, crucially involved in signal transduction pathways, especially those related to mechanotransduction and the response to the shear stress exerted by blood flow [147, 148]. Indeed, VE-cadherin can either sense mechanical stimuli from the surrounding environment and transfer them to the cell cytoskeleton, or it can be affected by intracellular signals, consequently altering AJs organisation [149, 150, 151]. Furthermore,

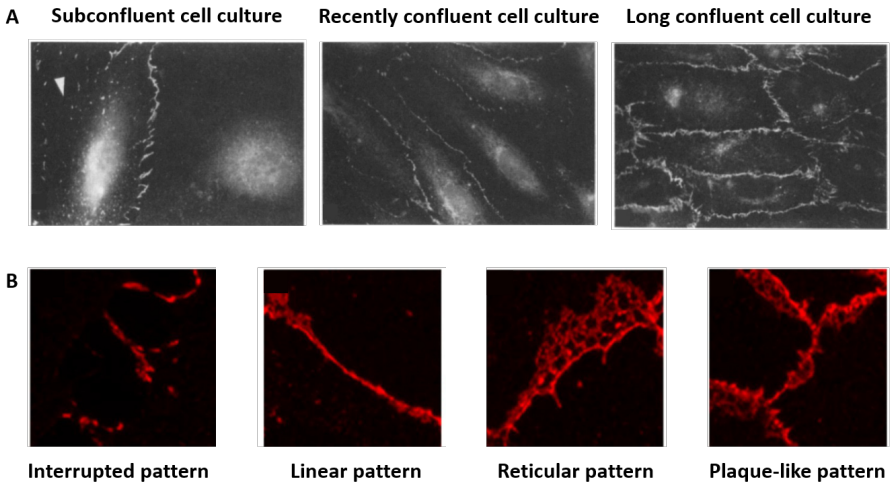

Figure 2.3: **VE-Cadherin patterns in relation with cell confluence A.** Human umbilical vein endothelial cells (HUVECs) cultures at different stages of confluence. **B.** Molecular patterns observed in HUVECs cultures stained for VE-cadherin (red). Details are explained in the main text. Modified from [128] (A) and [152] (B).

cell functional state and density, as well as tissue maturation state, affect VE-cadherin organisation as well, resulting in four morphological patterns, namely linear, interrupted, reticular or plaque-like structures, associated with the cell cytoskeleton [128, 152]. They are reported in Fig. 2.3 in relation to cell confluence (i.e. the surface percentage of the culture system covered by cells) in a 2D culture model. In subconfluent cultures (i.e. insufficient amount of cells to form a compact and uniform monolayer), VE-cadherin is only detected at the cell periphery where cells have already formed intercellular contacts, hence, it appears interrupted. When cells reach full confluence, contacts between them are established along their entire periphery and VE-cadherin appears as a fine line along cell perimeters. As culture confluence progresses, cells pack together and their area decreases and VE-cadherin, not varying in quantity, thickens, acquiring a more complex, reticular pattern [128, 152]. Moreover, another kind of pattern was observed during the dynamic process of cell maturation, involving changes in cell morphology and organisation. Membrane portions of adjacent cells were shown to overlap, guided by the remodelling of the actin cytoskeleton, forming transient structures called junction-associated intermittent lamellipodia (JAIL), whose

size and number is inversely proportional to cell density. VE-cadherin was reported to gather at these sites and cluster in a plaque-like pattern, which successively bring to the formation of cell junctions, during JAIL retraction [153].

Furthermore, it has been also demonstrated that the endothelium is significantly affected by the mechanical stimulation exerted by shear stress. *In vitro* studies, both in 2D cultures and in more complex (also 3D) experimental systems, have shown that physiological levels of shear stress favour ECs elongation and alignment in the direction of the flow. Flow-related mechanical cues also affect interendothelial junctions stability and VE-cadherin patterns. Indeed, short-term exposure to shear stress induces VE-cadherin linear pattern, while long-term exposure brings to protein aggregation at intercellular contact points. This is associated with the strengthening of cell junctions, hence favouring the overall barrier integrity. These rearrangements have been also linked to the reorganisation of the actin cytoskeleton into evenly distributed stress fibres, occurring in response to fluid flow [154, 155].

An example of specialised endothelium forming a fundamental biological barrier in human organism is the blood-brain barrier (BBB). It ensures appropriate nutrient (glucose) and oxygen supply for neuronal physiological activities, while protecting the brain from noxious elements circulating in the bloodstream (e.g. macrophages, antibodies, and toxins) [125]. For this purpose, TJs are preferentially expressed in brain microvessels and are the main structure accounting for vascular impermeability [156, 157, 158]. Sealing adjacent cells together, TJs prevent the paracellular transport to occur, thus leaving the transcellular pathway as the only route for molecular passage across the BBB. Since ECs receptors recognise a limited amount of molecules, this makes the BBB a highly selective barrier and protect the central nervous system from possible harm [159]. These features are also sustained by the presence of astrocytes, a brain-specific non-neuronal cell population carrying out several functions within the central nervous system. Among them, astrocytes establish physical interactions with the endothelium and biochemically support it, inducing TJs formation during brain development [160].

2.3 Overcoming biological barriers: drug delivery strategies

As discussed in this chapter, biological barriers are fundamental elements for the regulation of exchanges between living organisms and the surrounding environment. On the other hand, although their permeability can vary depending on their physical location, they represent one of the major obstacles to the effectiveness of therapeutic strategies, due to their impermeability to most drugs.

In order to overcome these limitations and favour drug transport to the target site, targeted drug delivery systems (DDS) were developed to localise the pharmacological activity. So far, the majority of approved DDS formulations are based on the use of nanocarriers, preferentially liposomes and lipid-based drug carriers [8]. In particular, soon after artificial vesicles manipulation started, it was demonstrated that liposomes are able to affect molecules distribution and prolong their retention within living organisms [161, 162, 163], with important implications for anticancer therapies [164]. Hence, drug carriers technology has been subject of constant research and development to optimise its efficiency. For instance, modulation of liposome composition to increase bilayer rigidity, e.g. by the incorporation of cholesterol [165] or sphingomyelin [166], has been proven to reduce drug leakage [167]. Also the use of polymers to produce carriers, called polymersomes, allowed control over membrane characteristics and thus led to improved carrier performance [168]. Moreover, carrier surface modification implies some advantages. Indeed, it increases their specificity, e.g. by attaching antibodies to the bilayer (immunoliposomes) [169], or ligands for receptors that are preferentially expressed within the target. For instance, liposomes have been functionalised with folic acid to direct them selectively against cancer cells, overexpressing the folate receptor [170]. Surface modifications also allow to stabilise liposomes within the body, slowing down their clearance and increasing their circulation time, as in the case of coating with biocompatible inert hydrophilic polymers, such as polyethylene glycol (PEG) [171, 172].

Furthermore, beyond being a well-suited model for mimicking phospholipid bilayer features, GUVs have been recently employed for drug delivery [173] (despite this promising aspect that is here acknowledged, throughout this work GUVs will be intended as a model for reproducing the features of phospholipid bilayers). Indeed, they allow the encapsulation of much larger

aqueous volumes, even an order of magnitude greater than values reported for other systems [174], and of bigger molecules. Therefore, recent studies have proposed GUVs as suitable tools for drug delivery strategies [175]. Moreover, these vesicular systems have been demonstrated to be an optimal precursor of smaller liposomes. For instance, an extrusion technique was employed to fragment GUVs and MLVs for drug carrier production, demonstrating that GUVs-derived liposomes were mainly unilamellar and more uniform in size. In addition, drug loading resulted maximised, by virtue of GUVs greater encapsulated volume [176].

Other DDS were developed to favour the accumulation of drugs or drug-carrier complexes at the target site. For instance, tissue characteristics were exploited or manipulated to induce drug release from the carriers. Examples of these strategies include passive drug accumulation through leaking vessels (as in the case of cancer) [177, 178], physical (pH- [179] or temperature-based [180, 181]) or magnetic targeting [182].

Membrane-disruption techniques are another convenient approach. They can be categorised as permeabilisation or direct penetration techniques, depending whether drug passage occurs through the disruption of membrane integrity or through a specific solid vehicle penetrating the membrane and introducing its cargo, respectively [12]. Strategies to alter membrane integrity include both biochemical and physical approaches, such as the use of detergents [183, 184] or membrane-active peptides [185, 186], as well as direct injection [187], ballistic particles [188] or electric fields [189, 190]. GUVs potential for these enhanced drug delivery strategies was demonstrated in this case as well. Indeed, by virtue of their cell-size scale, they were reported as effective means for the introduction of micrometre-sized objects into mammalian cells, through electrofusion [191, 192].

Another important mechanical approach to increase membrane permeability is based on the employment of acoustic waves, i.e. ultrasound (US), as it will be discussed in the next chapter.

Chapter 3

Cavitation-mediated enhancement of drug delivery efficiency

As discussed in the previous chapter, the presence of biological barriers impairs the efficacy of drug delivery. Nevertheless, intravascular administration is one of the most favourable routes for drug distribution to otherwise inaccessible target sites. Among the strategies to increase barrier permeability, the employment of ultrasound (US) has been reported effective in inducing membrane permeabilisation (sonoporation) maintaining cell viability [193, 194]. Moreover, the combination of US with gas microbubbles (MBs), usually used as ultrasound contrast agents (UCAs) in imaging, further strengthens this effect [195]. The physical phenomenon of cavitation underlies these events and has been proposed as a safe and effective strategy for enhanced drug delivery. This chapter will focus on the fundamentals of cavitation and the relative physics, as well as on USMB-triggered biological effects and USMB potential for enhanced drug delivery strategies.

3.1 Ultrasound employment in clinics

Since US technology is cheap, safe and non-invasive, it found wide application as a theranostic modality in pre-clinical research as well as in the clinical field, i.e. for diagnostics, anatomical and molecular imaging, and for therapeutic purposes. Ultrasound with frequency ranging from 1 MHz to 20 MHz are usually employed in clinics [196].

The main difference between diagnostic and therapeutic US applications

lies in the amount of energy carried by the acoustic wave, through plane, focused or unfocused US. Plane waves have usually lower energy. On the other hand, focused US are generated by spherically-curved transducers, which direct mechanical waves to a restricted portion of tissue volume, the focal point, where all the energy is concentrated. Hence, this kind of US is also known as high intensity focused ultrasound (HIFU) [197, 198].

Diagnostic US is not meant to cause any biological reaction. Hence, it has low-energy and is usually provided in short pulses. Plane waves are most often employed; however, focused US can be used as well, reducing beam width to increase image resolution, yet still avoiding biologically active levels of acoustic pressure and intensity [199, 200].

On the contrary, US therapeutic applications need to produce substantial biological effects through energy transfer to tissues. Low-energy non-focused US are typically employed for physical therapy (e.g. repair of fractures as well as relief of inflammation, muscle spasms, and pain [201, 202, 203]), for the insonation of large areas, and for sonophoresis, i.e. transdermal enhanced drug delivery [204, 205]. HIFU technology accounts for greater energy deposition; therefore, it is widely employed for direct ablation of lesions and tumours [197, 206].

US-triggered biological effects can be divided into thermal and mechanical (non-thermal) effects.

Thermal effects, i.e. temperature increase above physiological values, results from US energy absorption by the biological matter, with the consequent attenuation of US propagation. The amount of absorbed energy is strongly dependent on the features of the tissue (expressed by the tissue absorption coefficient), on US frequency and intensity [207, 208]. US-induced hyperthermia can be mild ($\mathrm{T} = 37 - 43°\mathrm{C}$) or high ($\mathrm{T} > 43°\mathrm{C}$). Mild hyperthermia, not implying irreversible tissue damage, is employed to favour drug accumulation at the target site [209]. High hyperthermia causes irreversible protein denaturation [210] and is mostly exploited to eradicate malignant cells [206, 211].

The thermal index (TI) is a clinically employed indicator of US-induced thermal effects. It describes temperature increases (in degree Celsius) in the biological sample and is defined as [199]

$$TI = \frac{W}{W_{deg}}\,, \tag{3.1}$$

where W is the acoustic power used at a certain depth of the target tissue

and W_{deg} is the power needed to rise the temperature of that tissue by 1°C in the same conditions [212], implying the reaching of a thermal steady-state, where US-tissue interactions can be considered stationary [213]. This parameter is used as a quantitative reference for US-induced temperature increase in biological structures. In order to standardise medical procedures and avoid harmful consequences on human organism, the Food and Drug Administration (FDA) defined a value of TI < 1 as generally safe and set a maximum safety value at TI $= 6$, which would bring tissue temperature up to 43°C [207].

The main US-induced mechanical effect is cavitation (acoustic cavitation, since it is provoked by US acoustic pressure), which will be described in the next section.

3.2 The physics of cavitation

Cavitation consists in the sudden nucleation of small air cavities within a liquid, occurring when the liquid pressure, p_L, falls below the saturated vapour pressure, p_V. It is linked to the liquid tensile strength, $\Delta \mathrm{P_C}$, defined as the value of pressure difference (tension), $\Delta \mathrm{P} = p_V - p_L$, at which liquid rupture due to bubble formation occurs [13].

Traditionally, cavitation is classified as homogeneous and heterogeneous. In the former case, vapour bubbles form in the liquid bulk. In the latter, bubble formation takes places in correspondence with solid walls or impurities suspended in the liquid.

Remarkably, the tensile strength of (ultra-)pure water, i.e. the negative pressure that the liquid can withstand without nucleating bubbles, is extremely large, on the order of -120 MPa. Such extreme values were obtained in controlled experiments with water microinclusion in quartz [214]. This extraordinarily large tensile strength implies that cavitation in water most often occurs via the heterogeneous mechanism. Indeed, any inhomogeneity (different chemical species, dissolved particles, interfaces, impurities, contaminating agents, or pre-existing air microbubles) decreases the tensile strength and favours the formation of cavitation nuclei at higher pressure [13]. In clinical applications, the heterogeneity is most often due to the non-uniformity of tissues with different composition and density.

Once the bubble is present in the liquid, the simplest model describing its dynamics [215] considers a simple bubble endowed with constant surface

tension within a bulk liquid. The model consists of the Rayleigh-Plesset equation,

$$\frac{p_G(t) - p_L^\infty(t)}{\rho_L} = R\ddot{R} + \frac{3}{2}\dot{R}^2 + \frac{4\mu_L}{\rho_L}\frac{\dot{R}}{R} + \frac{2\sigma_0}{\rho_L R}, \tag{3.2}$$

which describes the time evolution of the bubble radius $R(t)$. Here $p_G(t)$ is the pressure of the gas inside the bubble, ρ_L and μ_L are the liquid (constant) density and dynamic viscosity, respectively, and σ_0 is the (constant) liquid/gas surface tension. The bubble evolution is driven by the pressure in the liquid which, in the case of US excitation, is an oscillatory function of time $p_L^\infty(t) = p_e + p_{ac}(t)$, with p_e the equilibrium pressure in the liquid and p_{ac} the time dependent acoustic pressure. Due to the fast oscillations, the gas pressure inside the bubble changes according to the adiabatic law $p_G = p_G^0(V_B^0/V_B)^\gamma$ with γ the polytropic exponent and p_G^0 the gas pressure in the equilibrium bubble of radius R_0. The latter is related by the Young-Laplace law to the equilibrium pressure in the liquid, $p_G^0 = p_e + 2\sigma/R_0$.

The Rayleigh-Plesset equation (3.2) comes from the Navier-Stokes equation describing the purely radial motion of the fluid driven by the bubble oscillations,

$$\rho_L\left(\frac{\partial u_r}{\partial t} + u_r\frac{\partial u_r}{\partial r}\right) = -\frac{\partial p}{\partial r} \tag{3.3}$$

where, by mass conservation,

$$u_r = \dot{R}\frac{R^2}{r^2} = -\frac{\partial}{\partial r}\left(\frac{\dot{R}R^2}{r}\right) \tag{3.4}$$

and the viscous term vanishes altogether. Integration of Eqn. (3.3) with respect to r between $r = R$ and $r = \infty$ yields

$$\rho_L\left(R\ddot{R} + \frac{3}{2}\dot{R}^2\right) = p_L(R,t) - p_L(\infty)\,, \tag{3.5}$$

where $p_L(R,t)$ is the liquid pressure at the bubble surface. Using the force balance across the bubble interface,

$$p_G(t) = -t_n + 2\frac{\sigma_0}{R} \tag{3.6}$$

with $t_n = -p_L(R,t) + 2\mu_L\partial u_r(R,t)/\partial r$ being the normal stress in the liquid at the bubble surface, in Eqn. (3.5) leads to the Rayleigh-Plesset equation (3.2).

In absence of acoustic forcing, a bubble slightly displaced from its equilibrium radius, R_0, undergoes a system of damped oscillations which obey the linearised form of Eqn. (3.2),

$$\frac{d^2r}{dt^2} = -\omega_0^2 r - \alpha\frac{dr}{dt}\,, \tag{3.7}$$

where $r = R - R_0$ is the radial displacement,

$$\omega_0 = 2\pi f_0 = \frac{1}{R_0}\sqrt{\frac{3\gamma}{\rho_L}\Big(p_G^0 - \frac{2\sigma_0}{3\gamma R_0}\Big)} \tag{3.8}$$

the resonance angular frequency and $\alpha = 4\mu_L/(\rho_L R_0^2)$ the damping coefficient. The solution is

$$r(t) = r_0 e^{-\alpha/2t}\cos(\omega t) + \frac{\dot{r}_0 + r_0\alpha/2}{\omega}e^{-\alpha/2t}\sin(\omega t) \tag{3.9}$$

where $\omega = \omega_0\sqrt{1-\alpha^2/4\omega_0^2}$, while r_0 and $\dot{r}_0$ are the initial displacement and displacement velocity, respectively. The stationary response to an acoustic pressure of the form $p_{ac} = a\cos(\omega_{ac}t)$ is easily evaluated as

$$r(t) = -\frac{a}{(\omega_0^2-\omega_{ac}^2)^2 + \alpha^2\omega_{ac}^2}\left[\left(\omega_0^2-\omega_{ac}^2\right)\cos(\omega_{ac}t) + \alpha\omega_{ac}\sin(\omega_{ac}t)\right]\,. \tag{3.10}$$

As follows from the above solution, upon US excitation, the amplitude of bubble oscillation varies according to US amplitude and to the excitation frequency. The maximum bubble response is obtained for US excited at the bubble resonance frequency, $\omega_{ac} = \omega_0$. This linear response regime is called stable cavitation and occurs at low acoustic pressures (US intensity in the range of $0.3 - 3\,\mathrm{W\,cm^{-2}}$), Fig. 3.1A [208, 13]. When US intensity becomes larger (greater than $3\,\mathrm{W\,cm^{-2}}$), the linearised analysis does not apply any more and inertial cavitation occurs (Fig. 3.1B), which requires the solution of the full Rayleigh-Plesset equation. The destabilised bubbles oscillations enter a non-linear regime, where bubbles shrink and re-expand, until they may eventually reach a critical radius [217] at which a violent collapse may take place [13]. Bubble collapse associated with inertial cavitation leads to the formation of shock waves. Shock waves can be either spherical or asymmetric, depending whether bubbles are isolated or in the vicinity of walls (e.g. biological tissues) [218, 219] in which case strong liquid jet impinging the walls may form.

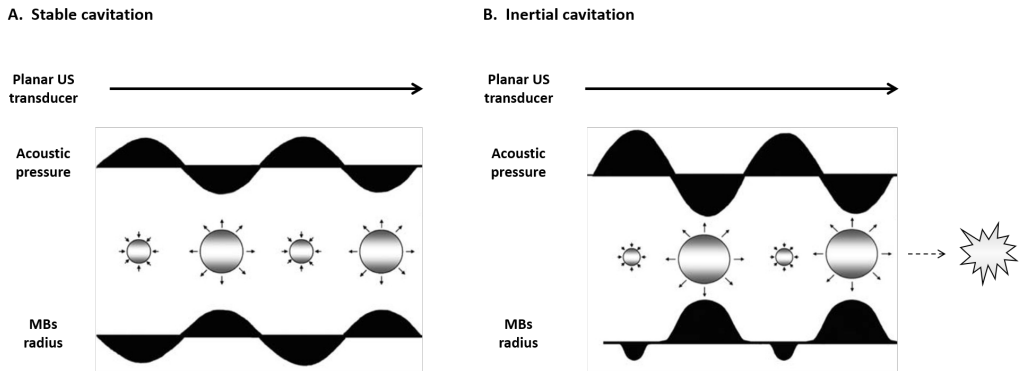

Figure 3.1: **Stable and inertial cavitation.** Linear (A) and non-linear (B) bubble responses to low and high oscillating acoustic pressure, resulting in stable and inertial cavitation, respectively. In the non-linear regime, the duration and extent of the expansion half cycle is greater than the compression half cycle, eventually resulting in bubble break-up. Modified from [216].

Of interest for the microfluidic platform presented in this PhD project is the evaluation of bubble behaviour upon exposure to US near rigid walls (i.e. the endothelial monolayer lining the PDMS microchannel). A modified form of the Rayleigh-Plesset equation (3.2) was proposed by Doinikov *et. al* [220], taking into account bubble vicinity to a solid wall with finite thickness. In the regime of stable cavitation, the linearised solution of this equation applies, and the bubble damped oscillations can be described as follows:

$$\ddot{r} + \alpha_w \dot{r} + \omega_w^2 r = -\frac{P_{ac}(t)}{\rho_1 R_0 \zeta}\,, \tag{3.11}$$

where $r = R - R_0$ is the radial displacement, $P_{ac}(t)$ is the driving acoustic pressure and ζ is a parameter accounting for the presence of the solid wall. α_w and ω_w are, respectively, the damping coefficient and the resonance frequency of the bubble and account for its proximity to a wall. They describe bubble response to the driving acoustic pressure and depend on the distance from the wall (see [220] for details). Hence, bubble behaviour in terms of oscillation amplitude, r_m, will be different. In particular, r_m variation depends on the excitation frequency with respect to the bubble natural resonance frequency in an unbounded fluid, ω_0. If the acoustic field frequency is greater than the bubble resonance frequency ($\omega_{ac} \geq \omega_0$), r_m decreases as the bubble approaches the wall. On the contrary, if the bubble is driven above its resonance frequency ($\omega_{ac} < \omega_0$), r_m increases [220].

Stable cavitation affects the surrounding fluid through acoustic microstreaming and Bjerknes forces. Acoustic microstreaming consists in a steady mean flow around the bubble, due to the vorticity created by the oscillations of its boundary layer [221].

Bjerknes forces are translational forces induced on the bubbles by the pressure field. They result in bubble displacement along the pressure gradient (primary Bjerknes forces) [222] or in variations in the distance between two adjacent oscillating bubbles, with consequent mutual attraction or repulsion (secondary Bjerknes forces) [223]. Of relevance for the experiments reported in this thesis are the primary Bjerknes forces, which are due to the acoustic pressure on the bubble boundary $S_B(t)$. The instantaneous pressure force is

$$\mathbf{F}_p(t) = -\int_{S_B(t)} p_L(R,t)\hat{\mathbf{r}}dS = -\int_{V_B(t)} \nabla p_L(\mathbf{x},t)dV \simeq -V_B(t)\nabla p_L(\mathbf{x}_B,t)\,, \tag{3.12}$$

where $\hat{\mathbf{r}}$ is the radial unit vector, and the last step follows by assuming that the bubble is much smaller than the spatial scale of the pressure field, given by the US wave length. After averaging over a period, the average force is $\overline{\mathbf{F}}_p = -\overline{V_B(t)\nabla p_L(\mathbf{x}_B,t)} \simeq -4\pi R_0^2\overline{r(t)\nabla p_L(\mathbf{x}_B,t)}$. A pressure wave of the form $p_{ac} = a_0\cos[\omega_{ac}(t-\hat{\mathbf{e}}\cdot\mathbf{x}/c)]$ travelling in the direction of the unit vector $\hat{\mathbf{e}}$ at the speed of sound c would then generate the average force

$$\overline{\mathbf{F}_p} = -\hat{\mathbf{e}}4\pi R_0^2\frac{\omega_{ac}}{cT_{ac}}\int_0^{T_{ac}} r(t)a_0\sin\left[\omega_{ac}\left(t-\frac{\hat{\mathbf{e}}\cdot\mathbf{x}_B}{c}\right)\right]dt\,, \tag{3.13}$$

where $\mathbf{x}_B$ is the position of the bubble centre. Analogously, a standing wave of the form $p_{ac} = a_0\cos(\omega_{ac}t)\cos(\omega_{ac}\hat{\mathbf{e}}\cdot\mathbf{x}/c)$ would give rise to the force component

$$\begin{aligned}\hat{\mathbf{e}}\cdot\overline{\mathbf{F}_p} = 4\pi R_0^2 a_0^2\frac{\omega_{ac}}{c}\sin(\omega_{ac}\hat{\mathbf{e}}\cdot\mathbf{x}_B/c)\cos(\omega_{ac}\hat{\mathbf{e}}\cdot\mathbf{x}_B/c)\\ \frac{\omega_0^2-\omega_{ac}^2}{\left(\omega_0^2-\omega_{ac}^2\right)^2+\alpha^2\omega_{ac}^2}\cdot\frac{1}{T_{ac}}\int_0^{T_{ac}}\cos\left(\omega_{ac}t\right)^2dt = \\ \pi R_0^2 a_0^2\frac{\omega_{ac}}{c}\frac{\omega_0^2-\omega_{ac}^2}{\left(\omega_0^2-\omega_{ac}^2\right)^2+\alpha^2\omega_{ac}^2}\sin\left(2\frac{\omega_{ac}}{c}\hat{\mathbf{e}}\cdot\mathbf{x}_B\right)\,.\end{aligned} \tag{3.14}$$

The average force is quadratic in the pressure amplitude (i.e. proportional to the US intensity), and directly proportional to the area of the bubble interface

(i.e. quadratic in the bubble radius). It is directed toward the nodes of the standing wave if $\omega_{ac} < \omega_0$ and towards the anti-nodes if $\omega_{ac} > \omega_0$. The bubble equation of motion

$$m_T \dot{\mathbf{v}}_B = -\xi \mathbf{v}_B + \mathbf{F}_p(t)\,, \tag{3.15}$$

where m_T is the total mass associated with the bubble (bubble mass plus added mass), $\mathbf{v}_B = \dot{\mathbf{x}}_B$ the bubble velocity, and $\xi = \beta\pi\mu_L R$ the Stokes drag coefficient, with $\beta = 6, 4$ for no-slip and free-slip boundary condition at the bubble surface, respectively, provides the average velocity,

$$\overline{\mathbf{v}_B} \simeq \frac{\overline{\mathbf{F}}_p}{\overline{\xi}} = \frac{R_0 a_0^2}{\beta\mu_L}\frac{\omega_{ac}}{c}\frac{\omega_0^2 - \omega_{ac}^2}{\left(\omega_0^2 - \omega_{ac}^2\right)^2 + \alpha^2\omega_{ac}^2}\sin\left(2\frac{\omega_{ac}}{c}\hat{\mathbf{e}}\cdot\mathbf{x}_B\right)\,, \tag{3.16}$$

where the bubble mass is assumed negligible. This shows that, in a standing pressure wave, the bubbles will accumulate at nodes if for $\omega_{ac} < \omega_0$, while for $\omega_{ac} > \omega_0$ they will be attracted to the anti-nodes.

Despite cavitation has been prevalently characterised in fluids, it also occurs in solids or in liquid phases included within solids, such as in soft materials like biological tissues, which most often present a visco-elastic behaviour [224].

Biological structures are subject to the mechanical stress exerted by the acoustic pressure and the oscillating bubbles. When it comes to US clinical applications, cavitation occurrence needs to be carefully evaluated in order to avoid damages to the involved tissues. Therefore, analogously to the TI described in § 3.1, the mechanical index (MI) was defined as an indicator of US-triggered cavitation. This parameter is given by the ratio of US peak negative pressure, PNP, to the square root of the centre frequency of the field, F_c, both normalised, respectively, to pressure and frequency reference values, as follows [225]:

$$MI = \frac{PNP}{\sqrt{F_c}}\,. \tag{3.17}$$

As for the TI, a higher MI is associated with a progressive increase in the risks for patients. According to the FDA clinical standards, values of MI < 1 are considered safe, while the upper safety limit is set at MI $= 1.9$, above which US-induced cavitation would take place, causing tissue damage [226]. Moreover, in clinical applications US can be combined with the concomitant administration of exogenous particles, as in the case of UCAs. This causes

a decrease in the cavitation threshold, i.e. the value of pressure triggering cavitation phenomena. As a consequence, the standard safety limits for the MI needs to be stricter. The upper safety limit has been thus set at MI = 0.7 by the British Medical Ultrasound Society [225, 198].

3.3 Microbubbles as ultrasound contrast agents

The effects of heterogeneous cavitation on biological tissues upon exposure to US can be strengthened in presence of microbubbles (MBs), mainly used in clinics as UCAs in imaging or for therapeutic applications. They sense and respond to the acoustic field through oscillation cycles, which, in turn, can further trigger cavitation (USMB-mediated cavitation).

3.3.1 Microbubbles: composition and properties

Clinically employed MBs are micrometre-sized bubbles (diameter range: $1-10\,\mu$m) consisting in a gaseous core enclosed in a stabilising external shell [227]. The gaseous core can be composed of air [228], nitrogen [229] or heavy inert gases with low solubility in water, such as perfluorocarbon (e.g. perfluorobutane, C_4F_{10}) [230], octafluoropropane (C_3F_8) [231], or sulphur hexafluoride (SF_6) [232]. The external shell is made of phospholipids [233], polymers [234], galactose [235] or albumin [236]. Their composition strongly influences their mechanical features and interaction with US.

The employment of MBs in clinics stems from their capability to enhance contrast in diagnostic imaging by ultrasound. Indeed, in 1968, small echogenic gas pockets, formed upon saline injection and US exposure, were found to significantly increase image brightness above the background of blood or tissue, producing diagnostic information about blood-filled regions otherwise appearing empty [237]. Since then, MBs of different kinds were developed and approved as UCAs; some examples are reported in Table 3.1.

MBs diameter matches erythrocytes size, so they are administered through intravenous injection and circulate through the body, interacting with US in the districts of interest [238]. In order to fulfil this function, they need to persist in the bloodstream and reach peripheral circulation without being prematurely discarded from the organism [216]. Hence, MBs need to be optimised in terms of composition and surface tension, so as to ensure their stability within the bloodstream.

Table 3.1: **Clinically approved MBs.** Examples of some MBs approved for clinical application as UCAs. Adapted from [199].

Name	Stabilising shell	Gaseous core	Company
Echovist	Galactose	Air	Schering AG
Albunex	Albumin	Air	Mallinckrodt
Levovist	Galactose	Air	Schering AG
SonoVue	Lipids	Sulphur hexafluoride	Bracco Diagnostics
Definity	Lipids	Octafluoropropane	ImaRx Pharm.
Imagent US	Surfactants	Perflexane	Alliance Pharm.

The gas contained inside MBs is typically a mixture of high-molecular-weight gas, G, and air content, A, with respective concentrations C_G and C_A (numbers of moles per unit volume). In the range of temperature and density inside MBs, both gases behave according to the ideal gas law. Hence, MBs internal pressure, p_i, is

$$p_i \;=\; (C_A + C_G)\,\mathcal{R}\,\mathrm{T}\,, \tag{3.18}$$

where $\mathcal{R}$ is the gas constant (expressed in $\mathrm{J\,mol^{-1}}$) and T the absolute temperature. When injected into the bloodstream, MBs are subject to an external pressure p_e determined by the sum of the atmospheric pressure, p_{atm} (101 kPa), and the so-called systemic blood pressure, p_b. Combining Eqns. (3.18) with the Youg-Laplace law, one finds

$$(C_G + C_A)\,\mathcal{R}\,\mathrm{T} \;=\; \frac{2\sigma}{R} + p_b + p_{atm}. \tag{3.19}$$

Given the small MBs diameter, the pressure difference across the interface is quite substantial and may lead the gas to diffuse across the interface and dissolve in the external aqueous environment. MBs persistence time (T_p) in the bloodstream thus depends on the gas diffusion, according to the following expression [216]:

$$T_p \;=\; \frac{\rho_G\,R^2}{2\,D\,C_s}, \tag{3.20}$$

where ρ_G is the gas density, D the gas diffusion coefficient, and C_s is the saturation coefficient of gas exchanges between the gaseous and aqueous phases, which is higher for more soluble gases. Equation (3.20) is obtained from the gas equation of state, from which $\rho_G = \frac{p_G}{R_G T}$, where R_G is the gas specific constant and $p_G = p_e + \frac{2\sigma}{R}$. Hence, T_p is also implicitly dependent on the gas pressure and on the surface tension σ of the water/gas interface. Given the solubility of nitrogen, the large surface tension of the water/air interface and the small MBs radius size, a simple air bubble would dissolve in a very short time. Hence, in order to increase MBs lifespan, the gas G contained in the bubble is selected to have a large molecular weight and a low solubility in water (i.e. in the bloodstream) [216].

The nature of the coating has a big influence on the MBs perfomances. The external shell composition controls their coalescence and, by reducing the surface tension, decreases the pressure difference across the interface for given bubble size. Moreover, it affects the echogenicity by influencing the natural oscillation frequency. Indeed, at constant external pressure, p_e, Eqn. (3.8) with $p_G^0 = p_e + 2\sigma_0/R_0$, as follows from the Young-Laplace law for the equilibrium bubble, leads to

$$\omega_0 = \frac{1}{R_0}\sqrt{\frac{3}{\rho_L}\left(\gamma p_e + \frac{3\gamma - 1}{3}\frac{2\sigma_0}{R_0}\right)} \tag{3.21}$$

which, since $\gamma > 1$ entails $d\omega_0/d\sigma_0 > 0$, implies that natural frequency increases with the surface tension.

Considering its crucial role, shell solubility in water needs to be as low as possible to prolong the shell lifespan, keeping MBs stable for a longer time. In this light, phospholipids are preferred for their surfactant nature (reducing σ) and lower solubility. Last generations of functionalised MBs are made of an albumin shell, which is even more compatible with the vascular microenvironment, being albumin an important component of the blood plasma [216, 239].

3.3.2 UCAs response to US

MBs shell coating modifies their response to US, making the basic analysis based on the Rayleigh-Plesset equation insufficient. Analysing the dynamics (see Table 3.1) through an ultrafast camera, Marmottant *et al.* [240] suggested that US-induced MBs oscillations produce strong surface area varia-

tions, generating molecular disequilibria at the interface. This implies that MBs physical parameters, i.e. surface tension and elastic modulus, cannot be considered as constant.Taking inspiration from low-frequency observations, the effective MBs surface tension could be described through three different ranges, depending on the MBs radius,

$$\sigma(R) = \begin{cases} 0 & R \leq R_{buckling} = \sqrt{A_{buckling}/\pi} \\ \chi\left(\dfrac{R^2}{R_{buckling}^2} - 1\right) & R_{buckling} \leq R \leq R_{break-up} \\ \sigma_{water} & \text{after break} - \text{up} \end{cases}, \quad (3.22)$$

where $\chi = 1/A_0 d\sigma/dA_{|_{A_0}}$ with $A_0 = 4\pi R_0^2$ being the area of the equilibrium bubble interface. During compression, bubble area decreases until it falls below a threshold (buckling area, $A_{buckling}$ - dependent on the number of interfacial lipid molecules and on their head-group area [241]) at which σ vanishes. Above $A_{buckling}$, bubble shell responds elastically, with a constant elastic compression modulus, χ, and an effective surface tension $\sigma(R)$ which is a quadratic function of the radius. During expansion, this elasticity is maintained up to a critical radius $R_{break-up}$, corresponding to the break-up tension $\sigma_{break-up}$, at which the bubble shell ruptures. After rupture, MBs behave as shell-free gaseous bubbles with the surface tension of water, σ_{water}. The modified evolution equation for the MB radius than takes the form of an extended Rayleigh-Plesset equation [240]:

$$\rho_L\Big(R\ddot{R} + \frac{3}{2}R^2\Big) = \Big[p_e + \frac{2\sigma(R_0)}{R_0}\Big]\Big(\frac{R}{R_0}\Big)^{-3\gamma}\Big(1 - \frac{3\gamma}{c}\dot{R}\Big) - p_e - p_{ac}(t) - \frac{2\sigma(R)}{R} - \frac{4\mu\dot{R}}{R} - \frac{4\kappa_s\dot{R}}{R^2}\,. \quad (3.23)$$

Beside the dependency of the surface tension on the bubble radius, Eqn. (3.22), two additional effects are included in the above equation. Firstly, the dissipation due to the surface dilatational viscosity of the shell, κ_s, is added. Secondly, by accounting for the compressibility of the liquid, the energy loss due to radiation of acoustic waves is also considered in the term inversely proportional to the sound speed c.

Linearising Eqn. (3.23), the angular resonance frequency of the augmented Rayleight-Plesset equation (3.23) follows as

$$\omega_0 = \frac{1}{R_0}\sqrt{\frac{\gamma}{\rho_L}\left(\gamma p_e + \frac{3\gamma - 1}{3}\frac{2\sigma_{eff}^0}{R_0}\right)}, \quad (3.24)$$

where, taking Eqn. (3.22) into account,

$$\sigma^0_{eff} = \sigma(R_0) + \frac{3\chi}{3\gamma - 1}\frac{2R_0}{R^2_{buckling}}\,, \tag{3.25}$$

with $\sigma(R_0) = \chi\left(R_0^2/R^2_{buckling} - 1\right)$, is the effective shell surface tension associated with Eqn. (3.22) for small oscillation around the equilibrium radius R_0 ($R_{buckling} < R_0 < R_{break-up}$) and, as obvious, the additional dissipative effects associated with wave radiation and shell dilatational viscosity only affect the damping rate α.

3.4 Cavitation-mediated biological effects

3.4.1 Cavitation bioeffects on the plasma membrane

USMB-induced cavitation alters cell membrane integrity, through sonoporation, which consists in the formation of small pores, as it was observed for the first time in 1999 by electron microscopy [242, 16]. At low US intensity, stable cavitation exerts a mechanical stress on the phospholipid bilayer and tears lipids apart [243]. This brings to the formation of pores with size ranging from few to hundreds of nanometres [244, 245]. These phenomena are intensified at higher acoustic pressures, resulting in the formation of a greater number of pores with bigger size (in the order of hundreds of nanometre up to micrometre), also due to the contribution of shock waves and jet streaming provoked by MBs collapse, further puncturing the membrane [245, 246, 247]. Furthermore, considerable membrane invaginations have been observed in addition to these events, and it is nowadays widely accepted that cavitation can also trigger cell endocytic pathways [248].

Furthermore, it has been demonstrated that USMB-induced membrane pores are transient and reversible, as they eventually reseal, albeit with different time scales [15]. Reversion of stable cavitation bioeffects is quicker, with a time range in the order of milliseconds to seconds after turning US off [249]. On the other hand, pores generated by inertial cavitation usually reseal within seconds after US exposure [244]. Pore opening and the reversion of cavitation bioeffects is shown in Fig. 3.2A.

Cavitation-mediated mechanical effects on cell membranes have been also described with a physical model proposed by Kimmel's group, integrating

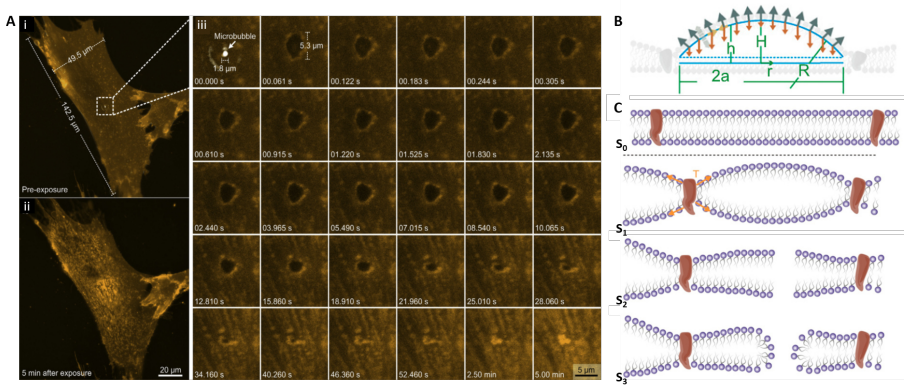

Figure 3.2: **Bioeffects of USMB-mediated cavitation on the cell membrane. A.** Confocal fluorescence time-lapse of pore opening and recovering on a fibroblast upon USMB-mediated cavitation. (i) Whole cell image prior to insonation (a single microbubble is showed through overlaid gray-scale contrast); (ii) Whole cell image after exposure to US; (iii) Time-lapse images (16.39 fps) acquired on a $15 \times 15\,\mu m^2$ frame centred on the region of interaction between the microbubble and the PM. **B.** Schematic sketch of the bilayer sonophore during the separation phase of its leaflets due to negative acoustic pressure. **C.** Different steps of the bilayer sonophore response to oscillating acoustic pressure. Initially, the membrane is unperturbed (reference stage, S_0). US activation triggers the oscillation of membrane leaflets, which increases the mechanical tension exerted on the phospholipids and on the mechanosensitive proteins (brown) inserted within the membrane (S_1). This eventually brings to the rupture of the phospholipid bilayer (S_2) and to pore formation (S_3). Images adapted from [15] (A) and [250] (B and C).

molecular forces, bubble dynamics and gas diffusion in and around the phospholipid bilayer [250]. According to this model, the phospholipid bilayer is a "sonophore", able to transform acoustic waves into intracellular deformations (in the order of nanometres or micrometres). The US-generated oscillating acoustic pressure is the driving force applied at the hydrophilic sides of the bilayer. Positive pressure peaks compress the lipid bilayer, whereas negative pressure pulls its leaflets apart, overcoming intermolecular attraction, viscous forces, the tension arising in a curved leaflet, and the inertial forces of the surrounding water. This dynamics can be modelled as the movement of one leaflet with respect to the other, considered fixed, as sketched in Fig. 3.2B. Such a cyclic oscillatory movement involves the fast approach of the moving leaflet towards the other at positive pressures, favouring the diffusion

of air molecules (dissolved in the surrounding water) within the membrane, so that they dissolve into its hydrophobic phase. Therefore, bilayer internal air pressure varies too, oscillating according to the acoustic field. These motion accounts for compression shock waves, large areal strain and high leaflet tension, determining membrane rupture and pore opening, as shown in Fig. 3.2C. In this context, oscillating MBs in the US field act as local amplifiers of the pressure peaks, intensifying the described phenomena [250].

3.4.2 Cavitation bioeffects on endothelial permeability

USMB-mediated cavitation effects within the cardiocirculatory system involve both blood vessel structure and the endothelial barrier. It has been shown that MBs oscillation exerts a mechanical effect on the neighbouring blood vessels wall, inducing invaginations and distensions within a millisecond time scale. Moreover, proximity to the endothelial wall can affect MBs behaviour; for instance, MBs motion is limited by microvessels size, resulting in an increased oscillation lifetime [251, 252].

With regard to the endothelial barrier, beyond sonoporation, exposure to US in presence of MBs leads to endothelial sonopermeabilisation, consisting in the opening of pores between adjacent ECs. Both direct MBs oscillation and the mechanical action exerted by microstreaming (stable cavitation) and liquid jets (inertial cavitation) account for this phenomenon, as shown in Fig. 3.3 [18, 252, 253].

It has been demonstrated on 2D *in vitro* cell cultures that endothelial exposure to USMB has both intracellular and intercellular effects, without impairing cell viability. At the single-cell level, USMB-mediated cavitation impacts ROS (Reactive Oxygen Species) homeostasis and results in the rise of the intracellular amount of Ca^{2+}, which enters the cell through the membrane pores [17]. In endothelial cells, increased levels of intracellular Ca^{2+} have been associated with cell hyperpolarisation rather than depolarisation [254]. This phenomenon is localised in areas of the membrane in contact with MBs. The underlying mechanism has been shown to involve the Ca^{2+}-dependent potassium (BK_{Ca}) channels, the main large-conductance outwardly rectifying K^+ channels [255]. They are activated by Ca^{2+} ions entering the cell through membrane pores and determine a K^+ efflux that overcompensates Ca^{2+} influx and locally hyperpolarises the membrane [256]. In general, cell sonoporation affects ion movement across the PM and has been associated with the consequent variation of the transmembrane current (TMC) [257].

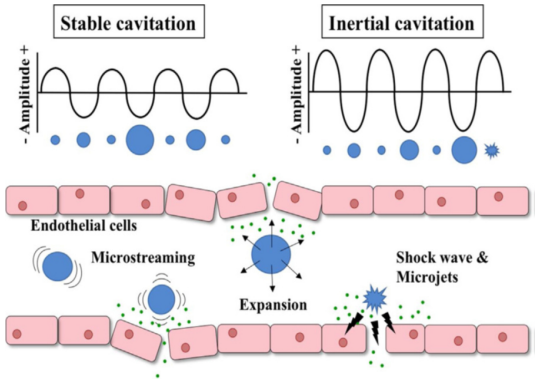

Figure 3.3: **USMB-mediated mechanisms leading to endothelial permeabilisation.** Mechanisms underlying endothelial permeabilisation upon stable and inertial cavitation. The integrity of the endothelial barrier is altered by the direct action of MBs oscillation. The mechanical stress exerted by microstreaming as well as by shock waves and liquid jets triggered by the stable and inertial cavitation regimes, respectively, further induce the opening of interendothelial gaps. Image from [18].

This implies the involvement of Na^+, K^+ and Cl^-, which are the main contributors to establish TMC levels [258]; however, the exact extent of their passage across the pores formed upon exposure to USMB cannot be exactly estimated due to their non-selectivity [257]. In general, USMB-mediated cavitation phenomena determine an increase in cell permeability to small molecules. For instance, the uptake of propidium iodide (PI) has been reported to occur in ECs while membrane pores are opened and to stop after they reseal [259]. Cell exposure to US in presence of MBs has also been associated with increased permeability to dextran or other probes [260], hormones [261], proteins [262], and plasmids [263].

Moreover, the mechanical stress exerted by cavitation-related phenomena triggers cytoskeletal rearrangements and a remarkable increase in F-actin stress fibres, as shown in Fig. 3.4A. This also affects the endothelium tissue as a whole, altering interendothelial junction complexes. In particular, VE-cadherin molecules loose their contacts, resulting in intercellular gaps opening and tissue permeabilisation, as in Fig. 3.4B. However, this phenomenon was demonstrated to revert completely within 30 minutes from insonation, with the restoration of intercellular contacts, thus highlighting the safety of USMB-mediated cavitation for clinical applications [17].

Kimmel's mechanical model describes these events considering the membrane not as a free surface, but constrained by other cellular components. In this context, US-induced periodic displacements of the bilayer leaflets exert

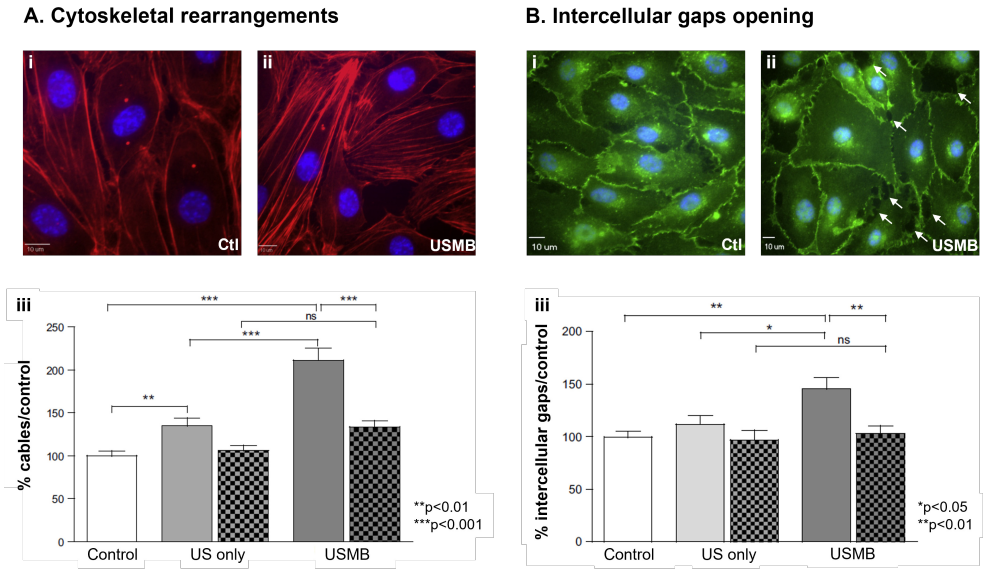

Figure 3.4: **Bioeffects of cavitation on the endothelium.** Dark-field images of 2D HUVECs cultures stained for F-actin (red) or β-catenin (green). Nuclei are stained with DAPI (blue). **A.** USMB-mediated cavitation induces cytoskeletal rearrangements and increases F-actin stress fibres in ECs. Comparison between HUVECs (i) in control conditions (untreated cells) and (ii) upon exposure to US and MBs. (iii) Bars showing F-actin stress fibres (mean number) per μm cell width. US alone determines a slight increase in F-actin stress fibres (light grey bar) compared to control. US exposure in presence of MBs significantly strengthens this effect (dark grey bar). In both cases, F-actin stress fibres number reverted to control condition 30 minutes after insonation (checked bars). **B.** Cavitation-induced opening of intercellular gaps in HUVECs stained for β-catenin. Comparison between HUVECs (i) in control conditions and (ii) upon exposure to US and MBs (gaps are pointed out with white arrows). (iii) Mean number of intercellular gaps per cell. US alone condition (light grey bar) was comparable to control, whereas US and MBs determined a significant increase in the number of intercellular gaps (dark grey bar). This phenomenon resulted completely reversed after 30 minutes, when the number of intercellular gaps returned to control levels (checked bars). Images adapted from [17].

mechanical forces (pushing and stretching) on the nearby subcellular structures, i.e. the cytoskeleton. This limits membrane motion and attenuates the maximal areal strain to which it is subject. Beyond having an effect on the lipid bilayer itself, the tension transferred to the cytoskeletal structure is propagated to intercellular junctions, impairing their integrity with the consequent formation of the intercellular gaps that further enhance tissue permeability [250].

3.4.3 USMB-mediated drug delivery

Cavitation-based drug delivery strategies consist in the systemic drug-MBs co-administration with the simultaneous application of US at the target site. This allows to localise cavitation bioeffects and maximise drug passage, as depicted in Fig. 3.5A [264].

Different strategies exist for the co-administration of drugs and MBs. For instance, they can be either injected as a single solution or administered as two separate pharmaceutical preparations [266]. In the second case, administration timing can be adjusted in order to reach drug plasma peak level before MBs injection [267]. This approach allows to administer different combinations of drugs and MBs.

Another strategy focuses on drugs and MBs conjugation to co-localise them at the target site, using MBs both as cavitation nuclei and drug carriers. This approach is particularly useful when pharmaceutical agents are toxic or unstable in the bloodstream, as they can be loaded into the MBs, as in Fig. 3.5B.i, and released only where cavitation is induced by US application [268, 269]. However, since MBs show low drug encapsulation capability, drugs can be also embedded within the bubble surface (Fig. 3.5B.ii) or attached to it (Fig. 3.5B.iii), e.g. through chemical conjugation or electrostatic binding (Fig. 3.5B.iv) [270, 271]. Alternatively, they can be conjugated with other carriers (e.g. nanoparticles or liposomes) with controlled-release mechanisms and co-administered with MBs [272, 273].

Furthermore, cavitation-mediated drug delivery can be further strengthened by designing MBs capable to target the therapeutic site. In this approach, MBs surface is functionalised with specific ligands for molecules that are preferentially expressed by cells at the target site, favouring MBs accumulation (Fig. 3.5B) [274, 265].

Cavitation-mediated drug delivery has been proven efficient for plasmid and gene delivery applications, allowing to overcome the limitations due to

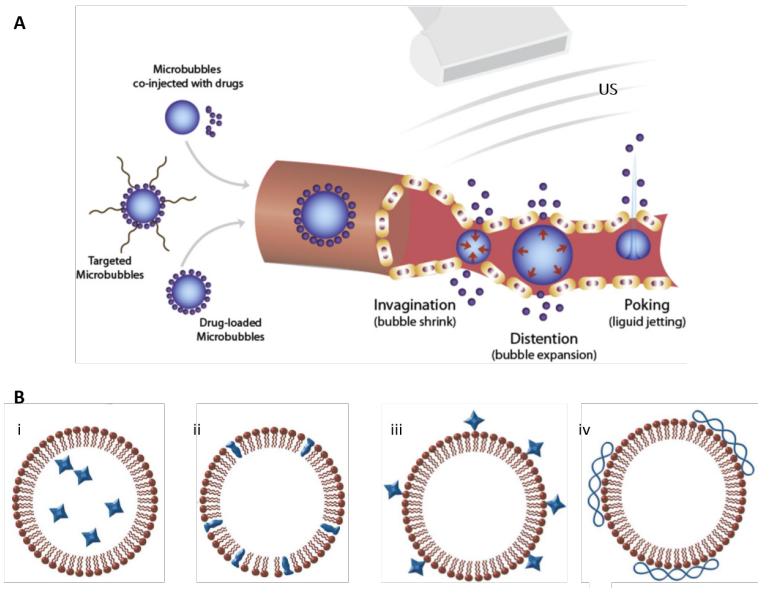

Figure 3.5: **Cavitation-mediated drug delivery. (A.)** Drugs can be physically combined with MBs or co-injected with them. US exposure is localised to the site of interest, where MBs oscillate upon the acoustic pressure. USMB-mediated bioeffects result in vessel wall deformations and in the permeabilisation of the endothelial barrier. **(B.)** Examples of different strategies for combining MBs and drugs. (i) Drugs can be encapsulated into MBs gaseous core; (ii) The pharmaceutical agent can be embedded within the bubble shell; (iii) Drugs can be attached to the bubble surface; (iv) The therapeutic agent can be bound non-covalently to the bubble surface. Adapted from [264] (A) and [265] (B).

the unstable nature of genetic material [266, 275, 276]. Moreover, it has already been successfully employed for cardiovascular drug delivery [277] to treat several conditions, such as atherosclerosis [278], diabetic cardiomyopathy [279] and even myocardial infarction [280]. It has also found wide application in cancer therapy [281].

Chapter 4

Microfluidics and biomedical applications

Given the complexity of biological structures, traditional *in vitro* cell cultures are not always suited to faithfully reproduce their features, especially from a mechanical viewpoint. This has driven biomedical research towards an interdisciplinary approach, involving knowledge, methods and technologies from other scientific fields. In particular, progress in microfluidics has significantly contributed to the development of highly versatile systems, able to recapitulate tissue and organ complexity in terms of biological and structural organisation. These microfluidic platforms are valid tools for the reproduction of biological barrier models, employed for several biomedical and clinical applications, as it will be discussed throughout this chapter.

4.1 Microfluidic development and features for biomedical research

Microfluidics is a branch of fluid mechanics. It is the science and engineering of manipulating small amounts of fluids (order of magnitude from 10^{-6} to 10^{-18} litres) within micrometre-sized devices, consisting in networks of microchannels of tens to hundreds of micrometres. Its origin dates back in the last decades of the XX century, when a boost towards miniaturisation accounted for significant progresses in electronics [23]. Successful fabrication methods (i.e. photolithography [282]) and the employment of suitable materials led to the development of Micro Electro-Mechanical Systems (MEMS)

and Micro Total Analysis Systems (μTAS), i.e. miniaturised devices where multi-step processes can be carried out in an integrated and automated way, with enhanced analytical performances [283]. The possibility to perform sampling, sample transport and separation, chemical reactions, as well as detection and analysis within a single chip has initially favoured the employment of these devices for chemical analyses, with the development of miniaturised systems for air and liquid chromatography [283, 284, 285]. The combination of μTAS with microfluidic technologies and tools to control fluid dynamics (e.g. pumps, sensors and microvalves) led to the Lab-on-Chip (LoC) technology. It consists in the miniaturised version of macroscale multi-step processes, integrated within single devices where events occur in controlled conditions and in an automated fashion. Moreover, miniaturisation supports a series of new functions that cannot be performed on greater scales [286, 287].

Initially, devices were mostly made of glass or silicon and their fabrication consisted in expensive, complex and multi-step processes requiring highly-specialised expertise, i.e. photolithography. Two elements strongly contributed to the employment of these systems on a greater scale. Firstly, in the middle of the 1990s, progress in microfabrication technology led to the development of soft lithography [288], an easier and low-cost alternative to photolitography. It allowed non-technician personnel to carry out microfabrication processes and significantly lowered the economical impact of this technology, making it accessible for a wider range of applications, including biomedical research. Secondly, advances in polymer science and engineering brought to the introduction of poly(dimethylsiloxane) (PDMS) [289, 290], an economic, easy to handle and non-toxic elastomer, totally compatible with molecules (e.g. proteins or DNA [291, 292]), cells and tissues [293, 294, 295].

Advancement in microfabrication: soft lithography and PDMS

As discussed, traditional lithography was initially employed in microelectronics and in the fabrication of semiconductor devices [296]. It consists in the transfer of a complex pattern (geometry) from a photomask to a chemical photoresist coated on a silicon or glass substrate (wafer), through exposure to light. The photoresist is a photosensitive material, which either degrades (positive photoresist) or polymerises (negative photoresist) upon exposure to light. The photomask is thus needed to selectively expose some parts of the photoresist to light in order to obtain, after dissolution of unpolymerised photoresist, the patterning of the geometry of interest. This process allows

to obtain the master mould, or stamp, which can be used to produce multiple devices.

With a conceptually similar approach, soft lithography aims at generating these patterned structures through rapid prototyping and in a high-throughput way [297]. Its key feature lies in printing, moulding and embossing with elastomeric (i.e. mechanically soft) materials to reproduce the geometry of the master mould. This implies important advantages, including a drastic reduction of time and costs of production, the increase in technique versatility and flexibility, as well as its accessibility to a wider range of users. Moreover, soft materials can be functionalised to improve their compatibility with biological molecules. Soft lithography also allows a higher patterning resolution (down to $\sim$ 30 nm) than contact printing photolithography (limited to 100 nm by optical diffraction), and more complex micropatterns, including curved and 3D structures [298, 299]. Recently, however, some other photolithographic approaches have significantly reduced the resolution limit. For example, projection printing photolithography has allowed to push resolution below the limit of 100 nm [300, 301], while photolithography based on surface plasmon polaritons can ensure a half-pitch resolution as low as 14.6 nm, with the concrete possibility to reach the 10-nm limit [302, 303].

Most microfluidic devices for biological applications are made of PDMS, a silicon rubber composed of an inorganic siloxane backbone, with organic methyl groups attached to silicon. Being characterised by very low glass transition temperatures, PDMS elastomers are fluid at room temperature (RT) and become solid by cross-linking, which is induced by the addition of a curing agent and makes this material suitable for casting and for the realisation of different micropatterns. Moreover, PDMS is well-suited for cell culture purposes. Indeed, it is a moderately stiff elastomer (Young's modulus = 1 MPa), chemically inert and biocompatible [298]. It is also impermeable to water, yet permeable to gases, thus ensuring a sufficient O_2 and CO_2 supply to cells. Being optically transparent to $\sim$ 300 nm, it is fitted to be combined with microscopy techniques. Finally, despite being inherently highly hydrophobic (advancing contact angle of water, $\theta_a^{H_2O} \sim 110°$), it can undergo hydrophilic treatments to change its surface chemistry in terms of polarity and interfacial free energy [297, 304].

Among the soft lithographic techniques, replica moulding (REM) is widely used [305, 306] and basically composed of three steps. Initially, a master mould is generated; this step still relies on the employment of photolithography. Then, an elastomeric prepolymer, typically PDMS, is poured onto

the mould, cured and peeled off, so that its surface results patterned with the relief nanostructures of the original master. Finally, this pattern is re-replicated using other soft materials, including PDMS itself. This process allows the rapid and faithful reproduction of multiple copies (> 50) of the geometry of interest [298], with very high resolution [307] and the possibility to replicate non-planar surfaces [308].

These advancements paved the way to LoC employment in biology and biomedical research, providing valuable supports for cell and tissue engineering, pharmacology and drug delivery, clinical diagnostics and proteomics [309]. This was also made possible by some advantages offered by microfluidic systems. First of all, device geometry can be easily customised through soft lithography, providing high versatility for the reproduction of different microenvironment. The possibility to regulate fluid injection and its timing further increases the control over the experimental conditions, including chemical and physical microenvironment (i.e. biochemical gradients and mechanical cues) [310], as well as cell density and their 2D or 3D spatial organisation [311, 312]. Moreover, fluid flow can be modelled and finely controlled in terms of velocity patterns and shear stress [313, 314].

In addition to its biocompatibility, PDMS is also optically transparent, low-autofluorescent and stable, making microfluidic platforms extremely well-suited for direct optical visualisation [290]. Indeed, several microscopy methods, including confocal fluorescent microscopy, real-time imaging, and time-lapse recording can be performed, guaranteeing the possibility to follow in real time biological processes inside the devices [24]. Beyond PDMS, other materials can be used to fabricate microfluidic devices, including polymethylmethacrylate (PMMA), polycarbonate (PC), polyimide (PI), polystyrene (PS) and the family of cyclic olefin polymers [315, 316, 317, 318].

Furthermore, the micrometric size allows the use of small amount of usually expensive fluids and reagents, such as culture medium, molecules, drugs, thus contributing to microfluidics cost-effectiveness [24]. Finally, parallelisation and automation are two other advantages of these systems. Indeed, the possibility to have multiple independent compartments on a single platform allows to carry out parallel assays, even in a high throughput and automated way, significantly improving the standardisation of the experiments and, hence, their reproducibility [319, 320].

In this context, a new category of "bioinspired" and cell-based devices was developed, allowing to produce biological barriers complex models for *in*

vitro studies, including the endothelial barrier. Moreover, the employment of droplet microfluidics [321], consisting in the manipulation of immiscible fluids within a device with specific geometrical patterns, allowed the production of nano- and micro-particles with tunable characteristics in terms of composition, shape, and size. For this reason, it has been recently applied for the formation of vesicular systems, including GUVs and drug delivery carriers [322].

4.2 Cell-based microfluidic platforms

Within microfluidic platforms, the adjustable combination of micropillars, microchannels and microchambers provides different geometries and levels of structural complexity, with high biological relevance. Indeed, both 2D and 3D cell culture models can be obtained, mimicking the physiological organisation of tissues and organs. Either homotypic or heterotypic cell monolayers, also grown in separated compartments, or cell cultures organised upon the three dimensions can be realised, possibly with the aid of porous membranes, scaffolds or matrices as well [24, 312, 323]. Such a structural complexity also involves cell microenvironment, crucial for cell differentiation and physiology. These devices allow to spatially and temporally control culture conditions in terms of chemical [324, 325], physical and mechanical stimuli [326, 327], as well as temperature [328] and gas control [329], nutrient supply and waste removal [330, 331]. In this respect, they offer greater advantages compared to 2D traditional culture systems, such as flask or Transwell, which, lacking the fine tuning of these aspects, do not ensure a faithful reproduction of the biological conditions [24, 332]. These features, integrated with microscopy techniques, can provide important information about culture conditions as well as about cell behaviour and responses, even at the single-cell level and with a high temporal resolution (< 1 s) [24, 330]. For instance, phenomena like cell growth and death [333, 334], differentiation [335], and cell migration [324] have been investigated in microfluidic devices.

Exploiting such versatility, several cell culture and tissue models have been implemented within these platforms, with increasing levels of complexity. For instance, key features of the tumour microenvironment (TME) were reproduced in microfluidic devices [336, 337]. These TME-on-chip models allowed not only to characterise its role in cancer progression, but also to test the efficacy of innovative therapeutic strategies, such as immunotherapy

[338].

The progressive increase in biological similarity has eventually led to the so-called Organs-on-Chip (OoC) technology, i.e. microfluidic platforms where physiological functions of tissues and organs can be recapitulated as well as their 3D structural organisation and microenvironment. Reproducing organ morpho-functional units within micrometre-sized devices, this technology offers valuable experimental models to mimic both physiological and pathological conditions [309, 339].

Microfluidic platforms also represent valuable alternatives to animal models, which lack in similarity to human metabolism and are often limited in their employment also due to management and ethical issues [340].

4.2.1 Vasculature-on-chip models and drug delivery

In this scenario, microfluidics allowed the realisation of several *in vitro* models of endothelial barrier and microvasculature, reproducing either single channels or more complex networks. They consist in PDMS microfluidic platforms or other substrates (e.g. biologically derived hydrogel), combined with different kinds of approaches, including the pre-defined patterning of geometries (also using subtractive scaffolding) and self-assembly from ECs sprouting [25].

The first attempts to implement the vascular endothelium in microfluidic platforms focused on capillary bed models where ECs were cultured alone. For example, in Shin *et al.* [341] soft lithography was used to realise a PDMS channel network, where an endothelial cell line was cultured up to 14 days to form a capillary bed, as depicted in Fig. 4.1A. The system was perfused with culture medium and a compact monolayer of ECs lined the walls of the microchannels, expressing typical endothelial markers [341].

Inclusion of hydrogel matrices and pro-angiogenic gradients

Successive work aimed at reproducing more physiological conditions. Hydrogel matrices were included within microfluidic devices, and pro-angiogenic factors gradients were established to favour endothelial maturation. For instance, the PDMS microfluidic platform developed in Vickerman *et al.* [342], reported in Fig. 4.1B(i), displayed a central "gel cage", where ECs/collagen mixtures could be loaded. Two flanking microchannels provide spatial and temporal control over fluid flow, guaranteeing the supply of nutrients as well

as the establishment of biochemical and pressure gradients. Real-time microscopy allowed to assess ECs migration and hydrogel invasion, with the subsequent maturation of complex and interconnected multi-cellular capillary-like structures in the 3D matrix, as in Fig. 4.1B(ii). They were demonstrated to be perfusable, through the injection of fluorescent microbeads, Fig. 4.1B(iii) [342]. Analogous results were obtained using another microflu-

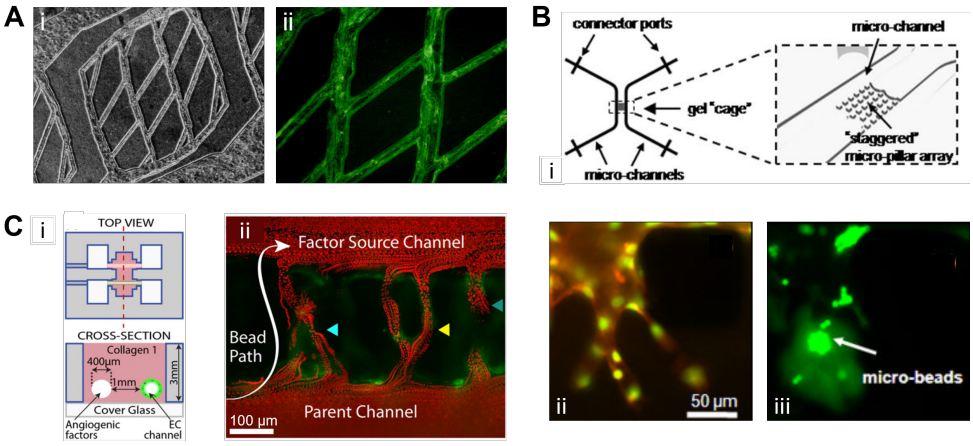

Figure 4.1: **Vasculature-on-chip models with ECs single cultures. A.** (i) Microfluidic channel network where human microvascular endothelial cells (HMEC-1) were seeded and formed a confluent monolayer within 7 days. (ii) HMEC-1 were stained for CD31 (green), a typical endothelial marker and key molecule for the formation of a cell monolayer, confirming that cells uniformly lined the capillary network. Adapted from [341]. **B.** (i) Sketch of the geometry of a microfluidic device where a central "gel cage" was loaded with soft hydrogels for the 3D culture of human adult dermal microvascular endothelial cells (HMVEC-ad). Two flanking microchannels provide culture medium supply. (ii) Microvascular sprout with HMVEC-ad stained for actin cytoskeleton (orange) and nuclei (green). (iii) Injected green fluorescent microbeads were shown to enter within the sprouted microvessels, confirming the formation of a perfusable lumen. Adapted from [342]. **C.** (i) Geometry of a PDMS microfluidic device where two parallel cylindrical channels are encased within a 3D collagen matrix and linked to fluid reservoirs. One microchannel is loaded with ECs and perfused with growth medium, while angiogenic-factors-enriched medium is flowed in the other microchannel. (ii) Merged image of a time-lapse acquisition of red fluorescent microspheres injected into the large channel. They were tracked over time, confirming the formation of new perfusable vessels. Adapted from [343].

idic platform [343], with two parallel microchannels embedded in a collagen matrix, as sketched in Fig. 4.1C(i). In one channel, ECs were cultured under flow conditions; in the other channel pro-angiogenic factors were injected and a gradient was established. Newly formed vessels were observed to sprout from the parent channel invading the matrix, recapitulating neoangionetic events, as in Fig. 4.1C(ii). This set-up also allowed to test different combinations of pro-angiogenic factors, investigating their role in inducing the formation of new vessels.

Mimicry of the physiological microenvironment: co-culture models

Co-culture models were implemented to better mimic an *in-vivo*-like microenvironment. They included fibroblast cells, naturally secreting angiogenic sprouting-inducing factors, within the devices. In these platforms, either vessel formation can be directed through the chip geometry or cells can be let organise autonomously into a vascular network. For instance, in the first case, the device developed in [344] was composed of two main parallel channels interconnected by eight bridge channels of customisable size, as showed in Fig. 4.2A.i and Fig. 4.2A.ii. By seeding ECs and fibroblasts in the matrix-filled main channels (Fig. 4.2A.iii), ECs, upon fibrolast-derived pro-angiogenic stimuli, were shown to migrate into the bridge channels from both sides and form tubular structures, as in Fig. 4.2A.iv. Eventually, with the two extremities fusing in the middle of the channels, perfusable blood vessels were obtained.

In the work by Moya *et al.* [327] the second approach was adopted. The microfluidic platform reported in Fig. 4.2B.i comprised two outer microchannels, connected to either sides of a chain of 12 millimetre-sized diamond-shaped microchamber, through a single communication pore. The microchannels were linked to large medium reservoirs for the establishment of hydrostatic pressure difference, controlling both convective and interstitial flow direction and magnitude. The two channels simulated venular and arteriolar circulations, while a mixture of endothelial and fibroblast cells embedded in a fibrinogen matrix was seeded into the microchambers. Upon the fine control of both mechanical (interstitial flow and pressure gradients) and chemical stimuli (pro-angiogenic factors, hypoxia, nutrient deprivation), an interconnected network of capillaries was obtained in each chamber within $14 - 21$ days, as showed in Fig. 4.2B.ii and Fig. 4.2B.iii. They were demonstrated to be perfusable and physiological shear stress was applied in the system.

In the described works, the integration of these platforms with microscopy approaches (phase contrast, epifluorescence and confocal microscopy, as well as time-lapse imaging) allowed to follow cell migration and angiogenic sprouting, as well as to investigate microvessels features. The injection of fluorescent microbeads (Fig. 4.2B.iv) or dextran confirmed the possibility to perfuse the formed microvessels, proving their stability and barrier function.

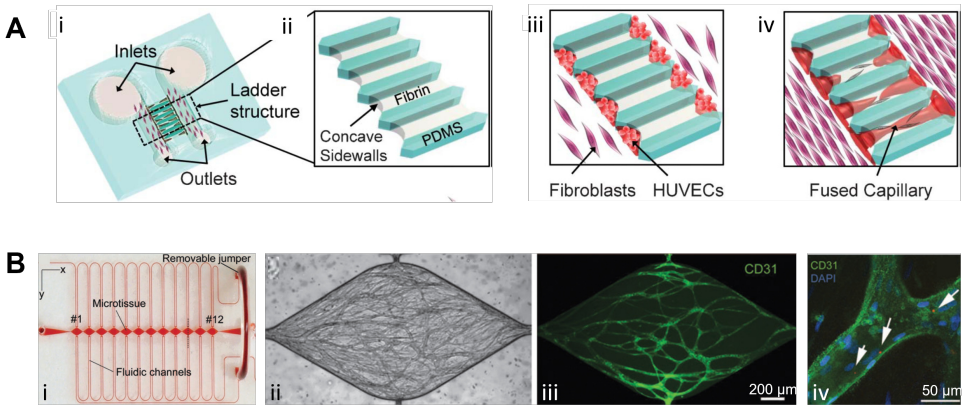

Figure 4.2: **Vasculature-on-chip models entailing ECs-fibroblasts co-coltures. A.** Design of a microfluidic platform (i) comprising two parallel microchannel interconnected by a ladder structure, composed of eight parallel bridge channels (ii), filled with fibrin gel. (iii) HUVECs were loaded at the extremities of each ladder channel, while fibroblasts were seeded into the two parallel microchannels. (iv) Upon the pro-angiogenic stimuli produced by fibroblasts, HUVECs grow and migrate to fuse in the centre of each ladder channel, bringing to the formation of a self-organised capillary network. Adapted from [344] **B.** (i) Geometry of the high-throughput PDMS microfluidic device consisting in twelve diamond-shaped tissue microchambers, daisy-chained and interconnected by pores on each side along the long axis. Each chamber is connected to two fluidic channels. Human endothelial colony forming cell-derived ECs (ECFC-ECs) and normal lung human fibroblast (NHLFs) were suspended in a fibrinogen solution and loaded within the microchambers. An interconnected network of perfusable capillaries was obtained within each chamber and was visualised through bright-field (ii) and fluorescent (iii) microscopy. (iv) Red fluorescent microbeads (white arrows) were injected within the microvessels and visualised through confocal microscopy, confirming the formation of a perfusable vascular network. Adapted from [327].

Investigations on endothelial barrier functionality

These platforms have been also employed to investigate endothelial response to flow-induced shear stress. For instance, Kim *et al.* [155] developed a microfluidic chip consisting in five parallel channels partitioned by microposts. Matrix-embedded ECs were seeded in the central channel, whereas fibroblasts were introduced in the two most external ones, as displayed in Fig. 4.3A.i.

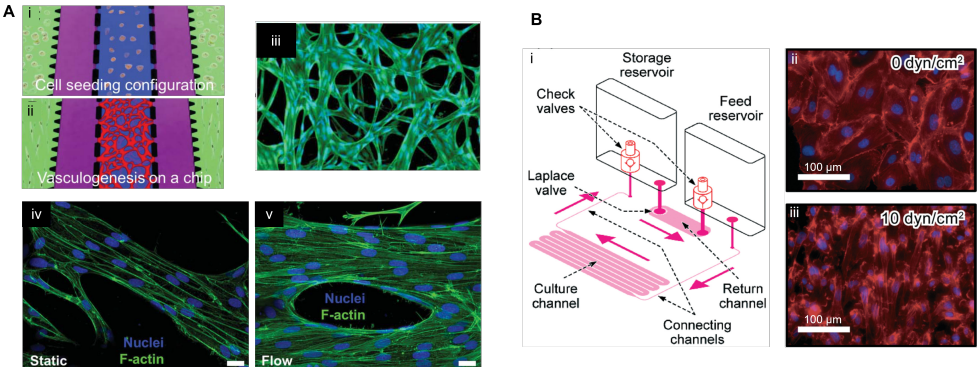

Figure 4.3: **Vasculature-on-chip platforms to investigate endothelial response to shear stress. A.** Microfluidic device composed of five parallel channels partitioned by microposts. (i) Cell seeding configuration, with ECs and fibroblasts loaded in the central and stromal (lateral) channels, respectively. (ii) Vasculogenesis occurring in the device, leading to ECs organisation in a perfusable vascular network. (iii) Fluorescent image of the vasculature grown in the device. Cells are stained with CellTracker (green), nuclei are stained with DAPI (blue). (iv) and (v). F-actin (green) configuration in vascular networks grown under static (iv) and flow (v) conditions. Physiological levels of shear stress induce the organisation of F-actin stress fibres aligned in the direction of the flow. Cell nuclei are stained in blue. Adapted from [155]. **B.** Microfluidic platform entailing multiple medium-circulation units where the flow is driven by pneumatic pressure difference obtained by the presence of two reservoirs. Three different microchambers allow to expose HUVECs cultures to flowing medium. (i) Layout of a single circulation unit of the device, comprising culture channels, where cells are grown, a return channel, and connecting channels (flow direction is indicated by the pink arrows). The storage and feed reservoirs generate a pressure-driven flow within the device. (ii) and (iii). Fluorescent images of HUVECs stained for F-actin (red) and nuclei (blue), cultured under static condition (ii) and under flow (iii), exerting physiological shear stress levels ($10\,\mathrm{dyn\,cm^{-2}}$). Adapted from [345].

The two compartments were separated by two intermediate fluidic channels, where culture medium was flowed. Upon the maturation of a microvascular network (Fig. 4.3A.ii and Fig. 4.3A.iii), evaluation of its low permeability confirmed the formation of an intact barrier. It was then perfused to exert physiological levels of shear stress ($0.31 - 7.22\,\mathrm{dyn\,cm^{-2}}$, depending on vessel size) on the microvessel walls. It was demonstrated that F-actin cytoskeleton reorganised into evenly distributed stress fibres aligned along the flow direction, as reported in Fig. 4.3A.v, compared to microvasculature grown in static conditions (Fig. 4.3A.iv). A significant increase in the synthesis of nitric oxide (NO), associated with several endothelial functions, was also reported [155]. Similar results were obtained through another microfluidic platforms developed in Satoh *et al.* [345], consisting in an array of three parallel independent cell culture units, where pressure-driven flow exerted physiological shear stress (2 or 10 $\mathrm{dyn\,cm^{-2}}$) on a monolayer of ECs covering the bottom of the microchannels. The device layout is shown in Fig. 4.3B.i. ECs under shear stress (Fig. 4.3B.iii) showed a spindle-like morphology and elongated along the direction of the flow compared to static cultures (Fig. 4.3B.ii). Moreover, increased production of endothelial-associated molecules, such as NO, was observed [345].

These results were also consistent with previous studies on 2D ECs monolayer exposed to laminar flow in non-microfluidic systems [154].

Increasing biological complexity: the blood-brain-barrier-on-chip

The reproduction of physiological-like vascular models paved the way for drug delivery studies within these systems, also involving more complex biological barriers, such as the blood-brain barrier (BBB). In particular, efforts were directed to enhance its permeability and favour drug passage. It had already been demonstrated that endothelial barrier permeability is shear stress-dependent in a 2D endothelial monolayer [346], and these results were confirmed for a 2D BBB model cultured in a flow chamber allowing the application of physiologically relevant shear stress [347]. In this context, a commercially available microfluidic device was employed to develop a relevant BBB-on-chip model [348, 349]. The microfluidic platform comprises two different compartments, namely the vascular channels (two independent microchannels) and the tissue compartment (a central chamber surrounded by the channels), interconnected by an interface of evenly spaced pores, as shown in Fig. 4.4A. By co-culturing neonatal rat capillary endothelial cells

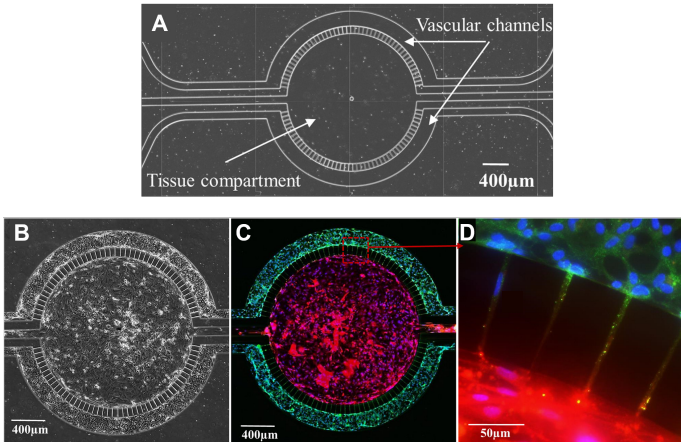

Figure 4.4: **The BBB-on-chip.** The microfluidic platform for the reproduction of the BBB. **A.** Geometry of the microfluidic device, with a central tissue compartment and two independent vascular channels interconnected by a series of pores. **B** and **C.** Brightfield (**B**) and fluorescent (**C**) images of the BBB model, with astrocytes (red) and HUVECs (green) grown in the tissue compartment and in the vascular channels, respectively. Cell nuclei are stained in blue. **D.** Detail of the interactions between astrocytes and HUVECs through the device pores, allowing the establishment of the physical and biochemical contacts for the formation of a physiological-like model of BBB. Adapted from [348].

and astrocytes, respectively in the vascular channel and in the tissue compartment (Fig. 4.4B and C), both biochemical and direct physical endfeet-like interactions took place between the two cell populations (Fig. 4.4D), resembling BBB physiological conditions. Moreover, endothelial cells lining the microchannel walls can be subject to physiological flow rates through the perfusable channels, allowing the formation of a vascular lumen. This BBB model was employed for permeability studies [348] as well as for the characterisation of signalling pathways involved in sepsis-induced neuroinflammation and the screening of therapeutics [350]. This system allows to mimic *in vivo* vascular features, thanks to the three-dimensional channels, with a similar size to microvessels, and to the possibility to perfuse them. Indeed, optimising shear stress to match physiological values ($1 - 12$ dyn cm^{-2} [351]) has been demonstrated to improve endothelial barrier maturation and functions.

Considerations on our blood vessel-on-chip system

The blood vessel-on-chip presented in this thesis shares some of its physiological features with other models discussed in this section. Its geometry, discussed in detail in § 5.1.1, is composed of two vascular channels (VCs) surrounding a central tissue compartment (TC). The different compartments are interconnected by a series of pores. The device was also employed for the realisation of a BBB-on-chip experimental model [348], as described in the previous paragraph and represented in Fig. 4.4.

The adopted approach to obtain the endothelial barrier is similar to the one presented by Yeon *et al.* [344], since cell organisation in a microvessel is "guided" by pre-existent channels. Indeed, according to our experimental protocol, presented in § 5.2, ECs are loaded into the VCs and let adhere. A possible drawback of this approach is the impossibility to evaluate endothelial remodelling behaviour, which was instead investigated in other works, where spontaneous angiogenesis or vasculogenesis were followed on-chip [155, 327, 342, 343]. On the other hand, guiding cell organisation provides the advantage of having a reproducible model, with the same standardised geometry and size in all the experiments performed. This aspect is more desirable for our goal, consisting, as stated in Chapter 1, in the quantification of endothelial permeability and evaluation of junction dynamics, through an image analysis code, self-customised for the specific geometry of our system. Moreover, compared to the other presented experimental systems, the presence of pre-existent microchannels provides another important advantage. The vascular network formed in the previously discussed works is perfusable only upon its complete maturation. On the contrary, in our system endothelial maturation within the PDMS microchannel occurs under flow conditions, with cells undergoing levels of shear stress ($10\,\mathrm{dyn\,cm^{-2}}$) matching the physiological ones, as explained in § 5.2. This allows to provide cells with physiological mechanical stimuli from the early stages of their maturation, obtaining a microfluidic systems reproducing some mechanical parameters of *in vivo* microvessels. In this context, having standardised geometrical features is also a key element for the complete control over the system microfluidic parameters, including the precise evaluation of shear stress levels to which ECs are exposed. Moreover, in accord with the experimental evidence reported in the previous paragraphs, endothelial exposure to physiological shear stress promotes cell organisation in a mature and integer barrier, favouring cell adhesion to PDMS walls [352] and their alignment

along the flow direction [155, 345].

In addition, such a control over microfluidic parameters is fundamental in this project, since, after a first quantitative evaluation of the endothelial permeability, genetically engineered cells were used in place of wild-type cells to investigate endothelial junction dynamics. Using this device, it was possible to maintain the same microfluidic conditions while changing the employed cells.

Our microfluidic system entails a single type of cell population, i.e. ECs, which can represent another drawback compared to other models where stromal cells are included to support endothelial growth and functionality [155, 327, 344] or to obtain organ-specific barriers [348]. Stromal cells indeed provide physiological biochemical stimuli to promote endothelial maturation and functionality. Actually, the microfluidic platform employed in this project does provide the possibility to include more cell populations, thus increasing structural and biological complexity of the system. Despite that being a future objective of our experimental project, at the present stage we decided to focus only on the endothelial monolayer behaviour and response

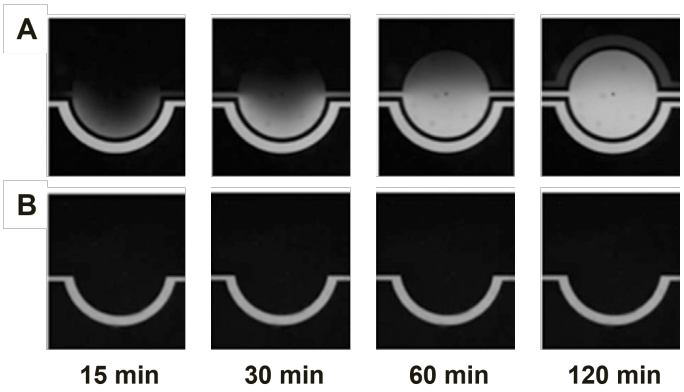

Figure 4.5: **Assessment of endothelial barrier permeability in our microfluidic system.** The endothelial barrier obtained in the presented microfluidic platform was tested in terms of functionality and integrity. Texas Red-conjugated Dextran (40 kDa) was injected into the VCs and fluorescence time-lapse recording was performed over 2 hours, in two different conditions: cell-free device (**A**) and in presence of a mature endothelial monolayer (**B**). The presence of the endothelial barrier prevented the fluorescent dye from diffusing into the TC, confirming its integrity. Adapted from [18].

to exposure to US in presence or absence of MBs, minimising any other external factor that could affect or contribute to that response. Nevertheless, future development of this system will involve the increase of the biological complexity in order to evaluate possible variations in the endothelial response to the exposure to USMB, due to the presence of a stromal cell population.

Furthermore, endothelial barrier functionality in our system had already been tested in terms of permeability to solutes under physiological flow conditions. To this aim, Texas Red-conjugated Dextran (40 kDa) was injected into one of the VCs and real-time fluorescence microscopy acquisition was performed over 2 hours in two different conditions: cell-free device and after barrier maturation under physiological shear stress. As it can be seen from Fig. 4.5A, Texas Red Dextran freely diffused into the TCs from the device microchannel in absence of cells. On the contrary, upon endothelial maturation, dye diffusion was prevented and fluorescence was confined within the VC, as in Fig. 4.5B, confirming the presence of an integer and functional endothelial barrier [18].

4.3 Microfluidics for the production of GUVs as plasma membrane models

As already discussed in Chapter 2, several experimental models have been developed to recapitulate the features of cell membrane. Among them, giant unilamellar vesicles (GUVs) [88, 353] are vesicular systems composed of a closed single phospholipid bilayer. Their match with the size of eukaryotic cells and the ease of their handling and visualisation through different microscopy approaches make them preferential model systems [88, 354]. In this light, some of their features can be optimised in order to enhance their biomimicry of natural membranes [355]:

- **Composition.** Membrane composition is a crucial factor for GUVs production, as phospholipids can differentially affect vesicle properties [356], such as structure, stability, biomechanics, fluidity and permeability [357, 358, 359, 360]. Hence, membrane composition needs to be adjusted according to the experimental needs. Moreover, other non-phospholipid surfactants or synthetic lipids with specific functionalities can be used, further expanding the possible combinations to tune membrane characteristics [361, 362, 363, 364].

- **Stability.** It can be classified as chemical, physical and biological stability and is related to vesicle durability over time [84]. Usually ranging from few minutes to even a few months, it depends on several factors, including vesicle size and composition [357], but also bulk properties such as temperature, pH, osmolarity, and salinity [356, 365]. Unstable GUVs undergo processes like lysis, coalescence, aggregation or budding [366].

- **Mean size and size distribution.** GUVs average size lies within the range of $10 - 100\,\mu$m [88, 354], which is also advantageous for their handling and manipulation. For a lot of biomedical applications, control over GUVs size distribution is fundamental. It can be influenced by lipid composition (e.g. the length of surfactant chains or the area of the phospholipid headgroup) and by some bilayer characteristics, such as spontaneous curvature and the elastic moduli described in Helfrich's model [353, 356, 367]. Usually, monodispersed GUVs (i.e. population of vesicles of the same size, or with small deviation) are preferred for their uniformity, which guarantees stability and the consistency of population properties [84, 368].

- **Encapsulation efficiency.** Molecules of different nature, drugs included, can be enclosed within phospholipid vesicles [369]. The substance to load into the vesicular system is named *core* or *sensitive material*, while the enclosing material is said *the encapsulant*; the final system is called *the encapsulate*. The encapsulation efficiency (EE), which can also be expressed as percentage, is defined as the ratio between the concentration of the core material entrapped within the encapsulate (C_{in}) over the total concentration of that substance (C_{tot}) initially added to the encapsulation system [370, 371]:

$$EE = \frac{C_{in}}{C_{tot}} \cdot 100.$$

  EE is strongly affected by vesicle composition and stability as well as by the chosen method for GUVs production [369, 372, 373, 374].

These characteristics can be affected by GUVs production method. Traditionally, batch methods have been employed, starting from natural swelling, introduced in the late Sixties of the XX century [353, 375] and successively

integrated with some strategies to increase the efficiency of the process (e.g addition of sucrose [376] or charged lipids [377]) [378], up to the use of electric pulses with the introduction of the electroformation technique by Angelova and Dimitrov in 1986 [379]. In general, batch methods rely on two different approaches, i.e. phase inversion and organic solvent-free [380].

However, batch methods cannot always guarantee ideal GUVs features, especially in terms of size distribution, and thus require post-processing steps to even their size out, such as extrusion or sonication. In this context, microfluidics allows more precise handling of the experimental conditions during both production and manipulation steps, as well as the possibility to monitor formation events in real time. It offers a series of advantages, including size monodispersity and the production of long-lasting vesicles [366, 381]. It also guarantees a fine control over salinity, osmolarity, temperature, pH, as well as fluid mechanical forces and vesicle lamellarity [355]. Moreover, in microfluidic systems vesicles can be easily produced in a high-throughput way and the post-production processes can be integrated on the same device [380].

Microfluidic methods for GUVs production can be divided into scaled-down macroscale techniques and approaches specifically designed for the microscale [380]. Examples of techniques derived from the macroscale include microfluidic-based electroformation [382], lipid film hydration in microchannels [383, 384], and extrusion (advantageous to control vesicle lamellarity) [385]. On the other hand, hydrodynamic flow focusing (HFF) is a widely employed microfluidic approach to produce phospholipid vesicles, exploiting diffusive mass transfer at the interfaces between immiscible liquids and allowing to control vesicle size by tuning the volumetric flow rate ratio of the different solutions [386, 387]. Other microfluidic methods for vesicles production include pulse jetting [388, 389] and droplet-microfluidic-based emulsion templates. The latter consists in vesicle formation based on either single or double emulsion drops, respectively water-in-oil (W/O) [390, 391, 392] and water-in-oil-in-water (W/O/W) [26, 381, 393, 394]. In particular, this last approach allows the formation of monodispersed GUVs with high efficiency and production rate [26]. It is based on the employment of W/O/W double emulsification, obtained through specific geometries combining HFF with droplet-based microfluidics. They usually consist in two consecutive flow focusing junctions, as depicted in Fig. 4.6A. At the first junction, a first aqueous solution is intersected by a lipid-containing oil phase and sheared into W/O emulsion droplets enclosed by a lipid layer with hydrophobic chains stabilised by the oily environment. At the second junction, W/O droplets in-

tersect with an external aqueous solution; lipid molecules thus reorganise into a bilayer, with the polar heads facing outwards on both sides [26, 89, 395]. Vesicles formation is finalised with solvent removal from the hydrophobic layer of W/O/W emulsion droplets. This can be accomplished with the addition of organic solvents to external aqueous environment, which solubilise and extract oil residues, leaving a single phospholipid bilayer around the water droplet. Different solvents or mixtures can be used, such as toluene and chloroform [26], toluene and tetrahydrofurane [396], and ethanol [89, 390].

In this project, solution composition was inspired to the work of Teh *et al.* [89]. The use of Pluronic F-68 (a di-block copolymer with surfactant properties) in the internal aqueous solution allows to protect the membrane from hydrodynamic damages and to prevent coalescence of the double emulsion droplets, thus improving GUVs stability. The oil phase was made of oleic acid, whereas the external aqueous solution contained glycerol, Pluronic F-68 and ethanol. Glycerol, water-soluble and biocompatible, increases the viscosity of the external phase facilitating the shearing of the oil solution; it also

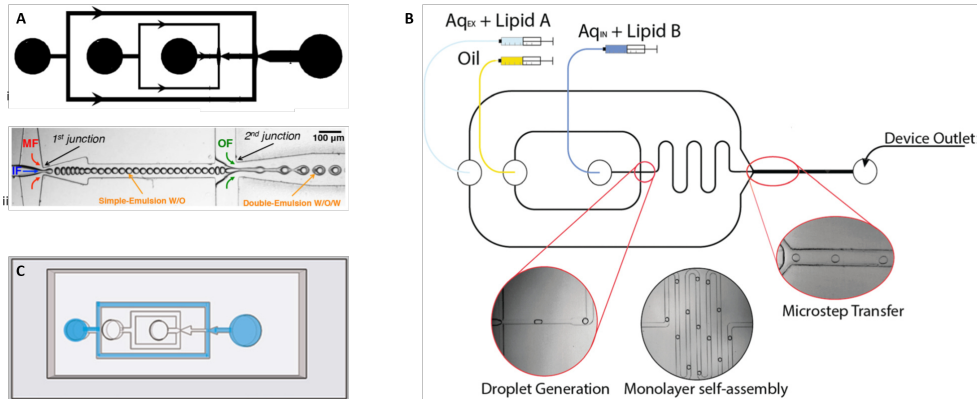

Figure 4.6: **GUVs formation through double emulsion template.** Examples of device geometries to promote the formation of a W/O/W double emulsion for GUVs production, through two consecutive flow focusing junctions. **A.** Sketch of a microfluidic device geometry (i), where the two consecutive junctions (ii) allow direct formation of the W/O/W double emulsion. Adapted from [395] **B.** The basic geometry can be optimised with additional features, such as a channel meander helping the spontaneous phospholipid organisation in a monolayer around the aqueous droplets in W/O emulsion. Adapted from [397] **C.** The selective hydrophilic treatment with PVA stabilises GUVs formation through favourable interactions between the channel walls and the lipid polar heads. Image adapted from [89].

contributes to the stability of the phospholipid bilayer. Ethanol is used for oil residues extraction from the bilayer, as oleic acid is soluble in this alcohol [89].

The described geometry can be optimised with other structures, such as a channel meander (coil) placed between the two junctions, as in Fig. 4.6B, aimed at favouring the spontaneous organisation of a phospholipid monolayer around each aqueous droplet [27].

Moreover, since the vesicular external surface is polar, its interactions with the hydrophobic PDMS walls are energetically unfavourable. GUVs stability during the formation process has been demonstrated to be improved by selective hydrophilic pre-treatments of PDMS channel walls, such as the treatment based on polyvynil alcohol (PVA) [398] employed in Teh *et al.* for GUVs production through droplet-based microfluidics [89] (Fig. 4.6C). PVA is a mechanically strong, biocompatible, and non-toxic polymer showing hydrophilic properties [399]. By coating the surface of external microchannel wall, PVA forms an hydrophilic layer that promotes and stabilises the formation of W/O/W droplets.

The vesicles obtained through this microfluidic approach are usually stable for long periods of time, up to three months [89, 395].

The GUVs produced through microfluidic approaches have been exploited to carry out a wide range of studies regarding membrane features [88], including their biomechanics [27, 397], their permeability [389] and their role as biological barriers for compartmentalisation and encapsulation [89, 390, 400].

Microfluidic-based, drug-delivery-related studies have been recently carried out employing GUVs as membrane models. For instance, a microfluidic device has been used to immobilise GUVs and study lipid membrane response to shear forces exerted by fluid flow, which can be relevant not only to mechanotransduction studies, but also to simulate haemodynamic conditions during drug transport [401]. Studies on membrane permeability and drug release have also been performed [402]. In this context, thanks to the fine control that microfluidics provides, vesicle composition and diameter can be adjusted and smaller drug carriers can be produced and functionalised to optimise drug loading and release [402, 403, 404, 405]. Moreover, GUVs themselves have been recently considered as drug carriers, as briefly discussed in § 2.3. Microfluidics has been thus exploited for the high-throughput production of functionalised GUVs for drug delivery purposes [406].

Besides, microfluidics contributes to drug delivery research in other ways.

For example, HFF can be also used for the fabrication of lipid-stabilised MBs, which can be used as UCAs [407]. In particular, since MBs act as acoustic amplifiers in cavitation phenomena, these systems can be combined with US for the development of enhanced drug delivery strategies [407, 408]. In this respect, microfluidics can offer a valid contribution to test and improve the efficiency of these drug delivery and therapeutic approaches.

Chapter 5

Experimental set-up and Results

Moving from the theoretical background provided in Chapters 2, 3 and 4, the following chapter is intended to present the experimental aspects of this PhD project, including the employed materials and methods, as well as the obtained results. In the first part of the dissertation, the detailed description of the device microfabrication procedure, through soft lithography, is provided. The second section is dedicated to the blood vessel-on-chip microfluidic system. Initially, the experimental set-up is described in detail, entailing the cell seeding protocol for loading endothelial cells into the microfluidic platform, the acoustic and optical set-ups for the USMB-mediated cavitation experiments, as well as the analysis of endothelial barrier permeabilisation. The relative results are then presented and discussed. Analogously, the last part of the chapter is devoted to the production of GUVs through microfluidics. The setting up of the experimental protocol is reported, providing details about the production of the W/O/W double emulsion template, the microfluidic parameters (e.g. solutions flow rate) and about the microscopy investigations carried out on the formed GUVs. Hence, the results related to vesicle formation are reported and discussed.

5.1 Microfabrication of the microfluidic devices

5.1.1 The geometry of the devices

The geometries of the devices employed in this project were designed by computer-aided design (CAD) and successively used for the production of a

master mould through photolithography. Then, soft lithography by replica moulding (REM) was used for the self-microfabrication of the microfluidic platforms. Both devices were made of PDMS.

The blood vessel-on-chip device

The commercially available microfluidic platform is produced by SynVivo (AL, USA) and used throughout this project. A home-made replica of this device, shown Fig. 5.1A, was microfabricated to be bonded onto a 0.17 mm-thick microscope glass coverslip (alternatively to the standard 1 mm-thick microscope glass), in order to optimise the resolution for confocal fluorescence microscopy.

The device geometry, sketched in Fig. 5.1B, comprises a circular microchamber (1575 μm $\times$ 100 μm, diameter $\times$ height), named the tissue compartment (TC), surrounded by two independent microchannels (200 μm $\times$ 100 μm, width $\times$ height), representing the vascular channels (VC), where vascular endothelial cells (VECs) can be seeded and cultured. Each VC can be accessed through an independent inlet, while two inlets provide control over the TC. The TC and the VCs are interconnected by a series of radially distributed pores (3 μm $\times$ 3 μm $\times$ 100 μm, width $\times$ height $\times$ length), spaced every 50 μm.

The SynVivo geometry was chosen for its well-characterised microfluidic properties (e.g. even flow distribution and controlled values of shear stress),

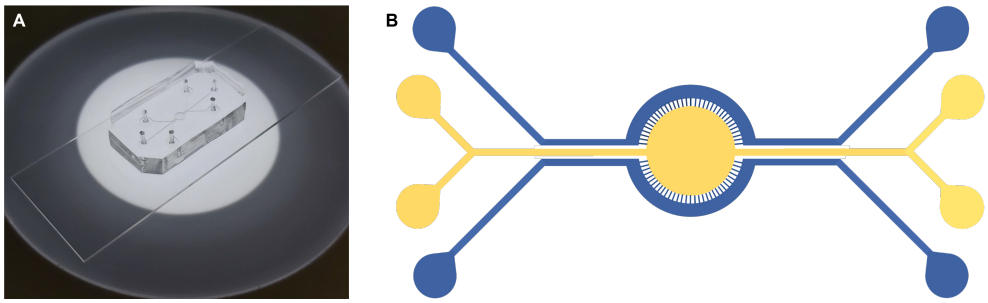

Figure 5.1: **The blood vessel-on-chip device. (A.)** The PDMS microfluidic platform self-microfabricated through soft lithography. Adapted from [29]. (**B.**) Sketch of the device geometry. The central tissue compartment (yellow) is surrounded by the two vascular channels (blue) and connected to them through a porous membrane.

the ease of handling and for its versatility, which gives the possibility to increase the structural and biological complexity through 2D or 3D co-cultures within the different compartments. Moreover, the presence of two VCs either allows to obtain two endothelial vessels within the same device (using cells coming from the same batch and undergoing the same growth conditions) or to establish biochemical gradients, by flowing enriched medium into one of the two microchannels.

Double exposure lithography was performed in order to obtain the two different heights (100 μm and 3 μm) within the microstructure, as it will be explained throughout this section.

The device for GUVs production

The geometry of the microfluidic device employed for GUVs production is inspired by the work of Karamdad *et al.* [27] and is shown in Fig. 5.2. The device consists in three independent inlets (I_1, I_2 and I_3), one for each solution to form the double W/O/W emulsion. Two symmetric branches originate from both I_2 and I_3 to successively join at the intersection with

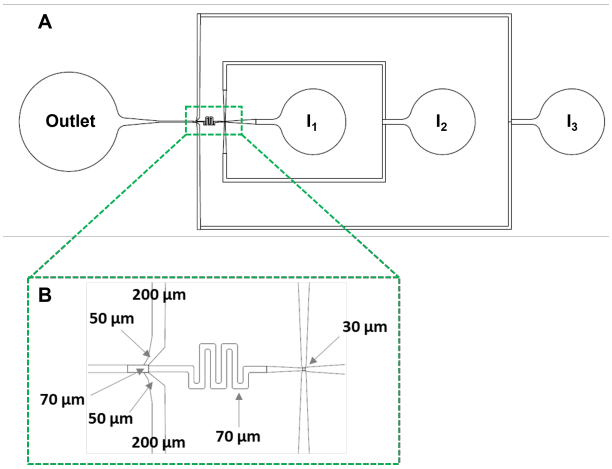

Figure 5.2: **The microfluidic platform for GUVs production. A.** CAD design of the device geometry, inspired by [27]. It is composed of three inlets (I_1, I_2 and I_3) for the injection of each solution and by two consecutive flow-focusing junctions, separated by a coil, for the formation of a W/O/W double emulsion. The produced GUVs are collected at the device outlet. **B.** Focus on the core of the geometry, where the solutions intersect to form the double emulsion.

the flow coming from the more internal inlet. In this way, two consecutive flow-focusing junctions are formed. A channel meander is interposed between them. From the second flow-focusing junction, the formed GUVs flow towards the device outlet for their final collection. The channel originating from I_1 is 300 μm wide $\times$ 100 μm high. It intersects the two symmetric microchannels originating from I_2 (200 μm $\times$ 100 μm, width $\times$ height) at the first flow-focusing junction, sized 30 μm. The successive channel meander has a dimension of 70 μm $\times$ 100 μm, width $\times$ height. The second flow-focusing junction is 70 μm wide. It is formed by the intersection between the channels coming from the meander and from I_3, from which two branches (200 μm $\times$ 100 μm, width $\times$ height) originate. Before the second junction, the two external channels width reduces down to 50 μm. The size of the microchannel flowing towards the outlet is 90 μm $\times$ 100 μm, width $\times$ height.

Compared to the device presented in Karamdad *et al.* [27], 90° angles were inserted at the channel bends. Hence, microchannels size was increased and the flow rates were optimised in order to prevent alterations of the fluid flow or air bubble formation, as well as to ensure laminar regime within the device. This allows the proper interaction between the different solutions at the flow-focusing junctions and the formation of the W/O/W double emulsion. Although computational fluid dynamics (CFD) and numerical simulations can be used to simulate and optimise the double emulsion formation process [409, 410], this goes beyond the scope of this thesis project, based on experimental work.

After microfabrication, the device was bonded onto a 1 mm-thick microscope glass.

5.1.2 Materials and Methods

Photolithography: Fabrication of the master mould

The master mould for soft lithography is obtained by photolithography. In this project, SU-8 epoxy resin (MicroChem, Newton, MA) was used to pattern the desired geometry onto the silicon wafer. In particular, SU-8 with two different viscosities was used: SU-8(3050) for 100-μm-high structures and SU-8(3005) for 3-μm-high patterns.

SU-8 is a negative photoresist, i.e, it polymerises upon exposure to UV light (at the wavelength $\lambda = 365$ nm). Hence, microstructures in relief are obtained with the aid of a photomask, shielding the photoresist from UV

light, patterned with the reverse of the geometry of interest. It thus allows UV light to pass through only where the SU-8 needs to cross-link. Therefore, the initial step of the microfabrication process involved the design of the geometries of interest. This was accomplished by CAD, the geometries were then printed onto a high-resolution photomask.

The main phases that can be identified in the photolithographic process, described in detail in this section, are the spin coating phase, the pre-exposure bake (soft bake), the exposure phase, the post-exposure bake (PEB), the development step and the final hard-bake. When double exposure lithography is performed, as in the case of the blood vessel-on-chip device, all the steps are initially performed for the 3-μm-high porous structure, until the development phase. Then, before carrying out the final hard-bake step, they are repeated to micropattern the 100-μm-high geometry. Finally, the hard-bake step is performed to obtain the master mould.

Pre-treatment of the substrate. The silicon wafer must be thoroughly cleaned from any physical (e.g. dust) or chemical contaminants before coating with SU-8. Indeed, any impurity could hinder photoresist exposure to UV light, compromise the uniformity of the photoresist coating on the surface, or provoke unwanted effects by reacting with other chemicals used during the process. The silicon wafer was thus immersed in Piranha solution (H_2O_2:H_2SO_4, 1:3) for 20 minutes. With its high oxidative power, this solution removes all metallic and organic contaminants. Then, the wafer was rinsed with distilled water and completely dried under a stream of air, to prevent water residues from affecting the adhesion of the photoresist.

Spin coating and soft bake. A spin coater (WS-650, Laurell Technologies, PA, USA) was used to deposit SU-8 onto the silicon wafer. Spin coating technique exploits centrifugal force to obtain a uniform film of desired thickness, which is influenced by the rotation speed, the acceleration and the SU-8 photoresist viscosity. The process is carried out in a pure nitrogen atmosphere. For the micropatterning of the 3-μm-high structure, SU-8(3005) was accelerated to 500 rpm in 10 seconds, and then accelerated by 100 rpm s^{-1} up to 4000 rpm, spinning at this velocity for 30 seconds. The spin coating process was carried out at 25°C. In order to obtain the thickness of 100 μm, SU-8(3050) was accelerated to 500 rpm in 10 seconds and then accelerated by 100 rpm s^{-1} up to 1000 rpm, for 30 seconds, at 20°C.

After spin coating, the photoresist can still contain up to 15% solvent, as well as possible built-in stress, which might affect the quality of the coating and the density of defects successively transferred to the device. To overcome this issue, the coated wafer was soft-baked (pre-exposure bake) at 65°C for 2 minutes and then at 95°C for 30 minutes.

Exposure to UV light and post-exposure treatment. Through the use of the high-resolution photomask, SU-8 was selectively exposed to UV light to activate its cross-linking and obtain the microstructures patterned in relief on the silicon wafer. A UV-KUB3 exposure box (Kloe, FR) was used, producing a power of approximately $200\,\mathrm{mJ\,cm^{-2}}$.

For the microfabrication of the blood vessel-on-chip device, double exposure photolithography was performed aligning two complementary photomasks, in contact mode. The first exposure was performed for the SU-8(3005) (3-μm-high porous structure) at 50% power for 15 seconds. After the development and the PEB steps (see below), a second 100-μm-thick SU-8(3050) layer is deposited onto the wafer to pattern the complementary structure of the device. The alignment process is performed manually with the aid of alignment references present in the two photomasks, visualised with an optical microscope. Then, the second exposure is carried out at 60% power for 22 seconds.

For the production of the GUVs generator device, exposure was performed at 60% power for the 100-μm-thick SU-8(3050) layer, for 22 seconds.

After UV exposure, PEB is performed, at 65°C for 1 minute and then at 95°C, for 7 minutes in the case of SU-8(3005), or for 10 minutes for SU-8(3050). Similarly to the previous soft-bake, such a gradual temperature increase minimises the mechanical stress inside the photoresist.

Chemical development. In this step, performed after each UV exposure and PEB, a specific solvent (developer) is used to selectively rinse the unlinked, fluid photoresist, with no effects on the hardened parts. Propylene glycol monomethyl ether acetate (PGMEA) (MicroChem, Newton, MA) was used as SU-8 developer. After exposure, the SU-8-coated wafer was immersed in PGMEA for at least 3 minutes at RT. The unlinked photoresist was thus dissolved, while the patterned microstructures were revealed. This step could still leave some unwanted unlinked photoresist residues, and, by developer penetration, even weaken the adhesion of the cross-linked photoresist onto

the silicon wafer surface. Therefore, after washing the substrate with isopropyl alcohol and drying it with compressed air, an additional post-bake step was performed, with a similar temperature ramp-up as before: 65°C for 2 minutes and then 95°C for 4 minutes.

Hard bake. As last step, hard bake was performed at 150°C for 1 hour, with the aim of removing all the residual stresses that could be still left within the exposed photoresist. This step improves the hardness of the patterned structures and increases the mould resistance during the successive REM.

Soft lithography by replica moulding and plasma treatment

After the hard bake, since our protocol does not involve a silanisation process before REM, the master mould is ready to be used for device microfabrication. A mixture of PDMS and its curing agent (10:1) (SYLGARD^{TM} 184 Silicone Elastomer Kit, Dow Europe GmbH, Germany) was prepared and degassed. The prepolymer was poured onto the master mould and thermally cured at 90°C for 30 minutes, to induce PDMS cross-linking. The hardened PDMS structure (with a complementary geometry to the master mould) was peeled off from the mould and punchered at the microchannel inlets and outlets, to ensure access to the micropatterned structures within the device.

Afterwards, PDMS was bonded to a microscope glass slide through plasma treatment, using plasma cleaner (PDC 002-CE, Harrick Plasma, USA) with a plasma power of 27 W at the pressure of 680 mTorr for 3 minutes. This treatment oxidises the surfaces exposed to plasma, allowing the successive formation of covalent (irreversible) bonds between them when put into direct contact and provided with thermal energy (60°C for approximately 30 minutes). In this specific case, Si-O-Si bonds were formed between the layers, since oxidation forms silanol groups (-SiOH) on PDMS surface, which interact with glass active groups. The newly formed bonds are strong enough to seal the microfluidic device, so that fluids can be confined and pumped at pressures as high as approximately 350 kPa [411].

5.2 Blood vessel-on-chip

The following section is devoted to the description of the blood vessel-on-chip platform and the relative experiments on endothelial permeabilisation. As

introduced in Chapter 1, aim of this part of the PhD project is the quantitative evaluation and the dynamic characterisation of endothelial permeabilisation upon exposure to US in presence or absence of MBs. After assessing the effects of USMB-mediated cavitation phenomena on the experimental model previously developed by our group [28, 29], interendothelial junction dynamics upon these events will be investigated through live imaging on an endothelium obtained using genetically modified ECs. Since USMB induce sonoporation, as explained in § 3.4, we can expect pores to form on the surface of the ECs as well. However, as already stated, aim of this investigation is the evaluation of endothelial permeabilisation through the opening of interendothelial gaps. For this purpose, VE-cadherin is stained either with immunofluorescence assays or by genetically engineering ECs and, despite acknowledging cell membrane sonoporation, attention is paid only to the events involving interendothelial junctions. In the following section, the realisation of the endothelial barrier models and the analysis of endothelial permeabilisation are described, with the relative results. Then, preliminary results regarding interendothelial junction dynamics are presented and discussed.

5.2.1 Experimental set-up

Cell culture

Human umbilical vein endothelial cells (HUVECs) were chosen as these primary cells are well-characterised and are considered an ideal experimental model for the formation of the endothelial barrier *in vitro*.

HUVECs pooled from different donors were purchased from Lonza (MD, USA) and stored in liquid nitrogen. Cells were cultured using Endothelial Basal Medium-2 (EBM-2) supplemented with the Endothelial Growth Medium (EGM-2) Bullet Kit from Lonza (MD, USA). Cells up to the 6^{th} passage were used, so as to guarantee the physiological expression of endothelial proteins.

HUVECs were cultured in 75 cm^2 treated flasks in a humified incubator at 37°C and 5% CO_2. Upon reaching $\sim$ 90% confluence, they were detached to be seeded into the microfluidic device. Cells were washed with Dulbecco's Phosphate Buffered Saline (PBS) without Ca^{2+} and Mg^{2+} (Sigma Aldrich, MO, USA) to remove all medium residues and then treated with Trypsin EDTA solution (Sigma Aldrich, MO, USA). After 50 seconds, trypsin activity was blocked by adding Trypsin Neutralizing Solution (TNS) (Sigma-

Aldrich, Missouri, USA), cells were collected and centrifuged at 1400 rpm for 7 minutes at RT. Then, they were resuspended in filtered EGM-2 at the average final concentration of 10^8 cells ml^{-1}, for the successive seeding. This concentration was experimentally proven to guarantee the optimal seeding confluence within the VCs. On average, three vascular channels can be obtained from a single flask with HUVECs at $\sim 85 - 90\%$ confluence.

Cell infection

In order to carry out live imaging microscopy and investigate junction dynamics, HUVECs were genetically modified to express constitutively fluorescent VE-cadherin. This was achieved through an infection protocol, carried out in collaboration with the group of Professor Bozzoni of the Department of Biology and Biotechnology of Sapienza University of Rome.

pLV-CDH5-mRuby3-IRES-puro plasmid (Plasmid #85144) [412], shown in Fig. 5.3, as well as the 2^{nd} generation packaging plasmids psPAX2 (#12260) and pCMV-VSV-G (#8454) were purchased by Addgene (MA, USA).

HEK293T cells were cultured in DMEM (10% FBS, 1% Glutamax, 1%

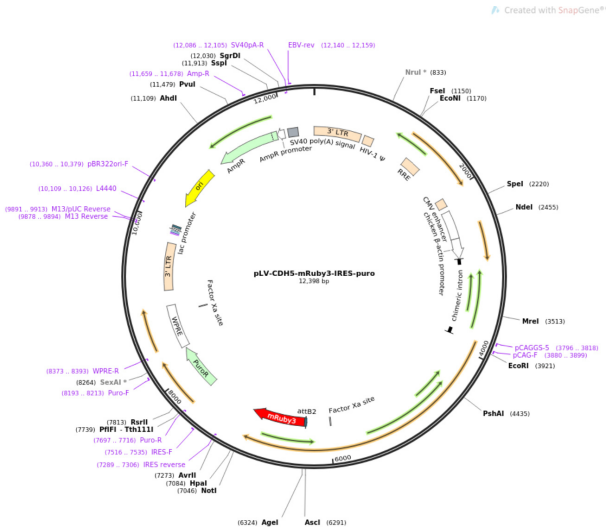

Figure 5.3: **pLV-CDH5-mRuby3-IRES-puro plasmid.** Map of the plasmid (Plasmid # 85144, Addgene) used for HUVECs infection, carrying the gene coding for VE-cadherin linked to the red fluorescent protein mRuby3. Taken from Addgene plasmid # 85144.

Pen/strep) and kept in logaritmic growth phase. 3 μg of pLV-CDH5-mRuby3-IRES-puro plasmid, psPAX2 and pCMV-VSV-G (4:3:1) were co-transfected into HEK293 cells on 150-mm dishes. Calcium phosphate transfection protocol was performed. Culture medium was replaced with low-serum medium (5% FBS) after 16 hours. The supernatant containing viral particles was harvested and filtered (0.22 μm filters). Using a viral concentration column (# UFC910024, Millipore, MA, USA), all the produced viral particles were used for the successive HUVECs infection.

HUVECs were cultured as previously described. Cells were infected in their own medium complemented with Polybrene (4 $\mu g\,ml^{-1}$). After 24 hours, the medium was changed and VE-cadherin fluorescent signal was visible in approximately 30% of cells in both infection conditions 4 days post-infection. Selective pressure exerted by Puromycin addition (0.5 $\mu g\,ml^{-1}$) allowed the identification of successfully-infected cells. Puromycin was only removed when uninfected control cells were all dead.

Cell seeding

Cell seeding protocol, outlined in Fig. 5.4, was adapted from [413] and [348]. The device was firstly degassed and rinsed with PBS with Ca^{2+} and Mg^{2+} (Fig. 5.4A). Before seeding, microchannels were functionalised to favour HUVECs adhesion to the PDMS walls, by perfusing fibronectin (200 $\mu g\,ml^{-1}$) (Sigma-Aldrich, MO, USA) for 2 hours at 37°C and 5% CO_2 (Fig. 5.4B) with the aid of a programmable multiple syringe pump (PhD ULTRA Syringe Pump, Harvard Apparatus, MA, USA). Afterwards, HUVECs were injected into the vascular channels (Fig. 5.4C) with the aid of a Tygon tube (Saint Gobain PPL Corp, PA, USA) and of the programmable multiple syringe pump. Initial cell confluence was optimised at $60\% - 70\%$, then they were let adhere to the channel walls at 37°C and 5% CO_2 for 4 hours in static conditions.

Then, the device inlets were connected to EGM-2 reservoirs through a Tygon tube and the whole system was placed inside the incubator, at 37°C and 5% CO_2 to protect cells from thermal shock. Outlet tygon tubes were connected to 1 ml plastic syringes (Fisher Scientific, PA, USA) secured on the multiple syringe pump located next to the incubator. This layout offers the possibility to generate a continuous flow inside the microchannels (Fig. 5.4D), pulling the medium from the reservoirs through the vascular channels. Flow perfusion was thus started and reached the rate of 0.5 $\mu l\,min^{-1}$ over the

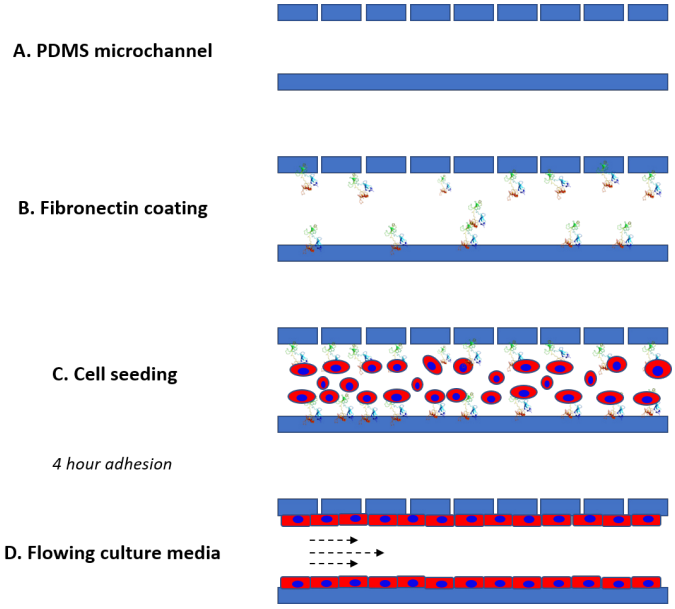

Figure 5.4: **Sketch of the seeding protocol for the realisation of the blood vessel-on-chip model.** Details about each step are provided in the main text.

first 24 hours, then, after refilling medium, flow rate was ramped up to $25\,\mu\mathrm{l\,min^{-1}}$, which exerted physiological levels of shear stress on ECs, i.e. $10\,\mathrm{dyn\,cm^{-2}}$.

Flow-induced shear stress

In order to allow the endothelium to grow under physiological-like conditions and to form mature and fully functional interendothelial junctions, growth medium was constantly flowed into the microfluidic platform. The flow rate was initially ramped up to $0.5\,\mu\mathrm{l\,min^{-1}}$ over the first 24 hours and then to $25\,\mu\mathrm{l\,min^{-1}}$ until full maturation. This ramp-up mode was chosen in order to allow cells to progressively adapt to the fluid flow increase over time.

The flow rate was chosen to exert physiological levels of shear stress on the endothelium. The average wall shear stress τ (expressed in $\mathrm{dyn\,cm^{-2}}$) for the device size was calculated using the following equation:

$$\tau = 6\,\frac{Q\mu}{w^2 h}\,, \tag{5.1}$$

where Q is the fluid flow rate expressed in $\mu\mathrm{l\,min^{-1}}$, μ the fluid dynamic

viscosity, expressed in $\mathrm{Pa} \cdot \mathrm{s}$, w and h the width and height, respectively, of the device microchannels, measured in m. At 37°C, the dynamic viscosity of the growth medium can be approximated to the dynamic viscosity of water, equal to $8 \times 10^{-4}\,\mathrm{Pa} \cdot \mathrm{s}$. Therefore, at the flow rate of $25\,\mu\mathrm{l\,min^{-1}}$ the shear stress exerted on the endothelium is approximately $10\,\mathrm{dyn\,cm^{-2}}$, which falls into the physiological range of $1 - 12\,\mathrm{dyn\,cm^{-2}}$ [351].

Immunofluorescence assay

All the steps of the immunofluorescence assay were carried out at RT conditions. ECs were initially fixed with paraformaldehyde (PFA) (Electron Microscopy Sciences, PA, US) for 15 minutes in static conditions and then rinsed with PBS with Ca^{2+} and Mg^{2+}. Afterwards, they were permeabilised through 5-minute incubation with 0.2% Triton X-100 (Sigma-Aldrich, MO, USA). VE-cadherin was stained by perfusing at $0.5\,\mu\mathrm{l\,min^{-1}}$ VE-cadherin mouse monoclonal antibody (Thermo Fisher Scientific, MA, USA), at the concentration of $5\,\mu\mathrm{g\,ml^{-1}}$ in 3% bovine serum albumin (BSA) (Sigma-Aldrich, MO, USA) for 1 hour. After rinsing, AlexaFluor647 conjugate-Goat anti-mouse IgG (H+L) secondary antibody (Thermo Fisher Scientific, MA, USA) ($2\,\mu\mathrm{g\,ml^{-1}}$) was perfused for 1 hour at $0.5\,\mu\mathrm{l\,min^{-1}}$ and antibody excess was washed with PBS afterwards. Actin filaments were stained by perfusing Phalloidin-Atto488 (Sigma-Aldrich), $30\,\mu\mathrm{l\,ml^{-1}}$ in 3% BSA, at $0.5\,\mu\mathrm{l\,min^{-1}}$ for 1 hour, rinsing afterwards. Nuclei were stained with DAPI (Thermo Fisher Scientific, MA, USA) for 5 minutes in static conditions and then rinsed with PBS.

Insonation chamber design

In order to carry out USMB-mediated cavitation experiments, an insonation chamber was designed to integrate the acoustic and the optical components of the experimental set-up. It was realised through CAD using the Rhinoceros software (Robert McNeel & Associates, WA, USA) and 3D printed. An inert plastic resin was chosen to provide structural strength and total impermeability. Indeed, it was filled up with deionised water during the experiments, for a dual purpose. Firstly, water was preferred over air as US propagation medium, as it matches the acoustic impedance at the interface with the PDMS device. Secondly, water was used to keep cells at their physiological temperature by pre-warming and maintaining it at 37°C. The in-

sonation chamber was tailor-made to match with the features of an inverted Olympus iX73 spinning disk confocal microscope, with the external size of $13 \times 11.5 \times 4.5$ cm^3 and the internal size of $11.5 \times 10 \times 3.5$ cm^3. It has a capacity of approximately $0.4\,l$.

The insonation chamber and relative technical drawings are shown in Fig. 5.5. As it can be observed, the bottom of the chamber is interrupted; it was sealed with 1-mm-thick plexiglass or with a 175-μm-thick glass coverslip,

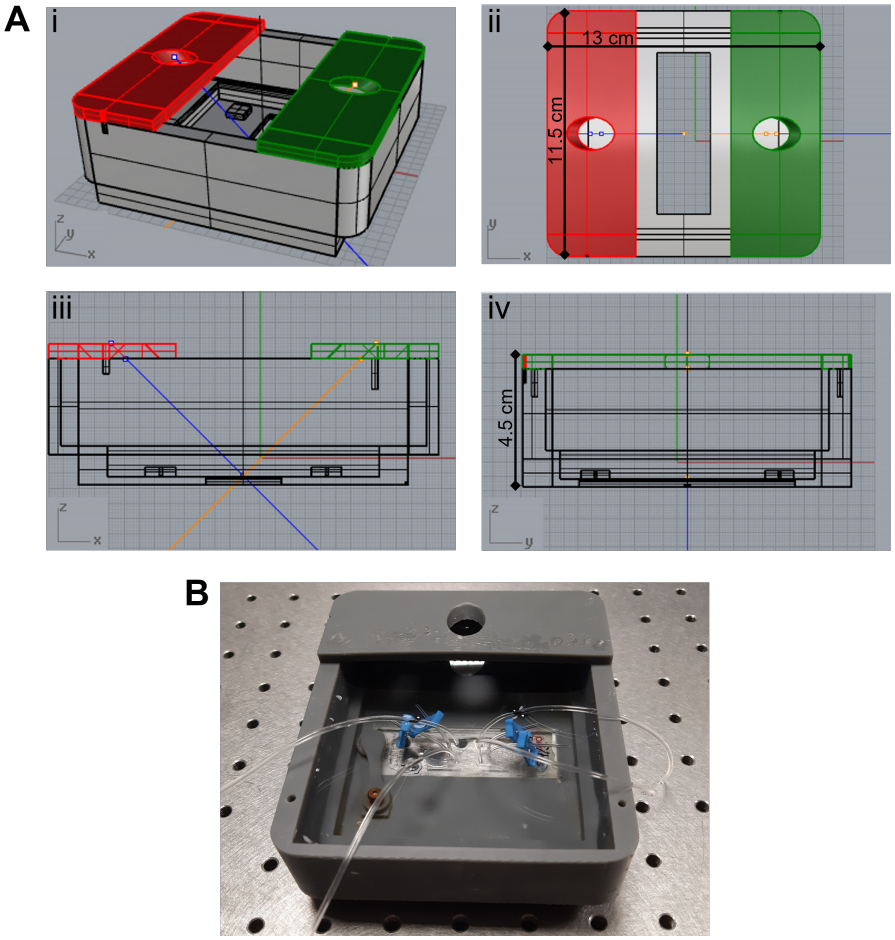

Figure 5.5: **Insonation chamber. A.** Technical drawing of the insonation chamber: (i) overview; (ii) top view; (iii) and (iv) lateral views. Internal dimensions: $11.5 \times 10 \times 3.5$ cm^3. Capacity: $\sim 0.4\,l$. **B.** Photo of the insonation chamber realised by 3D printing. Image from [29].

respectively for bright-field or confocal fluorescence microscopy. By placing the microfluidic device on top of the glass, direct visualisation of the vasculature is ensured, as the total thickness of the chamber and of the device glasses lies within the working distance of the used microscope objectives. On the bottom of the support, a pin was included to secure the device, in order to avoid its displacement in water and to make it adhere to the glass coverslip, preventing air infiltration.

The acoustic set-up was integrated by placing a support for the transducer on the top part of the chamber. It was designed with 45° inclination and at 35 mm distance from the microfluidic platform, to ensure US propagation in the far field to the vasculature and prevent uncontrolled pressure variations. Indeed, transducer calibration for 140 mV driving was previously performed with the aid of a needle hydrophone, identifying the distance of 25 mm from the transducer as the boundary between near and far fields.

The integration of the optical and acoustic set-ups is shown in Fig. 5.6.

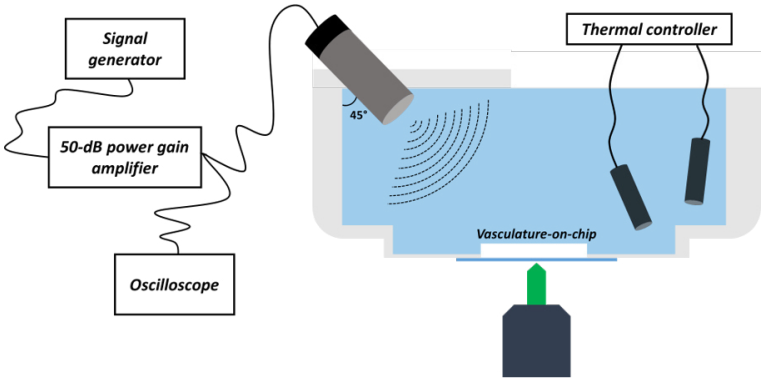

Figure 5.6: **Integration of the acoustic and optical set-ups for USMB-induced cavitation experiments.** The sketch shows the integration of the acoustic and optical components. The microfluidic platform is placed at the bottom of the chamber, ensuring optical access for microscope visualisation. The transducer is placed on top of the chamber at 45° inclination and US waves are generated by the US chain, composed of the signal generator, the 50-dB amplifier and the oscilloscope. US propagates through deionised water to the blood vessel model within the device. Water temperature was monitored and kept at 37°C with a thermal controller. Image from [29].

Acoustic set-up

As sketched in Fig. 5.6, the acoustic chain was organised as follows: a signal generator (Tektronix AFG3022c, OR, USA) emitted electrical signal in burst, which were amplified by a 50-dB power gain amplifier (ENI 240L) and sent to a planar, single element, 1-MHz-centre-frequency transducer (diameter: 12.7 mm), necessary to convert them in sine-wave US beams. This process was constantly monitored with an oscilloscope (Tektronix TBS1064, OR, USA), reading the amplifier output.

Cell were exposed to sine-wave US bursts at 1 MHz central frequency, 500 cycles repeated every 50 ms, 0.1% duty cycle (DC), corresponding to 500 μs pulse duration (PD), and 20 Hz pulse repetition frequency (PRF). US generated an acoustic pressure of 0.72 MPa (17 W cm^{-2} intensity), obtained driving the transducer at 140 mV. The system was insonicated for 30 s (corresponding to 600 pulses).

Optical set-up and imaging

Microscopy acquisition was carried out using an inverted Olympus iX73 equipped with X-light V1 spinning disk head (Crestoptics, Italy) and LDI laser illuminator (89 North, VT, USA), using MetaMorph software (Molecular Devices, CA, USA).

Fluorescent images of the wild-type HUVECs stained with immunofluorescence were acquired with the CoolSNAP MYO CCD camera (TeleDyne, Photometrics, AZ), while fluorescence real-time acquisition of genetically engineered HUVECs was performed with the Prime BSI Scientific CMOS (sCMOS) camera with 6.5 μm pixels (Photometrics, AZ, USA). Bright-field acquisition of MBs dynamics was carried out using an Evolve EMCCD camera (Photometrics, AZ, USA) at 1 ms exposure time.

In IF assays, the endothelium was stained for VE-cadherin, actin and DAPI, as in Fig. 5.7. Sampling was performed an with Olympus 20× air objective (NA = 0.45) to ensure a sufficient resolution for the interendothelial gaps analysis. The whole VC does not fit the field of view at this magnification. Therefore, several separated portions of the sample were captured and then stitched with Image J software by Fiji [414], in order to obtain a view of the entire endothelium. The acquisition in tiles guaranteed enough overlap to reconstruct the whole image. On the other hand, fluorescence live-imaging of the endothelium was performed during the whole experiment

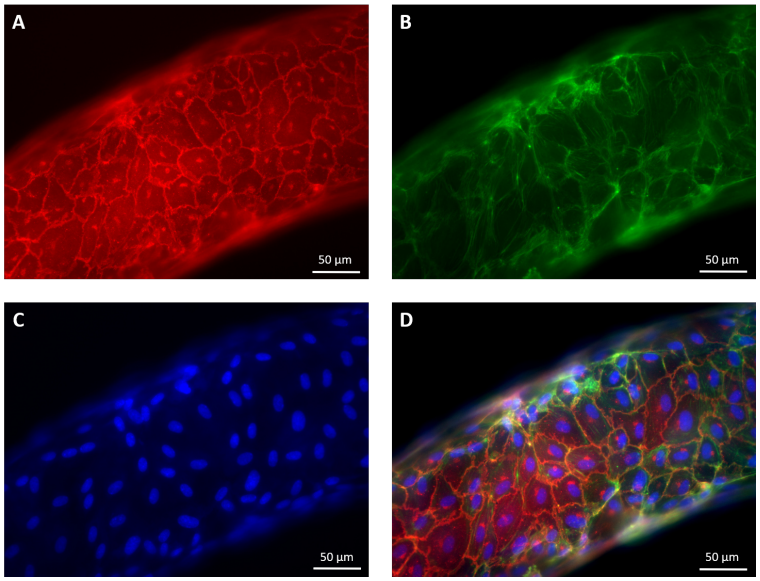

Figure 5.7: **Examples of fluorescence microscopy acquisition of the vascular channel.** The specimen was subdivided in tiles, each one acquired with different colour channels. **A.** VE-cadherin; **B.** Actin; **C.** Cell nuclei; **D.** Merging of the three channels for the same portion of the vascular channel. Image from [29].

on a single field of view of the VC. Time-lapse recording was carried out at 800 ms exposure time, with a time interval of 800 ms.

The three dimensional reconstruction of the channel (Fig. 5.9B and C) was obtained by acquiring 20× confocal Z-stack images of the endothelium (stained for VE-cadherin and cell nuclei) with the Prime BSI Scientific CMOS (sCMOS) camera and processing them through the Imaris software (Oxford Instruments, UK).

Microbubbles

SonoVue® (Bracco Research, Switzerland) were employed for the present investigation. They were chosen as their dynamics is well-known and their response to exposure to US is characterised in detail in Marmottant *et al.* [240].

SonoVue® suspension was reconstituted in 5 ml solution of 0.2% NaCl ($2 \times 10^8 - 5 \times 10^8$ MBs ml^{-1}, according to manufacturer's instructions). For USMB-mediated cavitation experiments, this preparation was diluted

to the concentration of $2 \times 10^7 - 5 \times 10^7\,\mathrm{ml}^{-1}$ in culture medium enriched with 2% HEPES buffer solution, in order to obtain 1 : 1 cell-to-bubble ratio [415, 416], in a 5-ml syringe. SonoVue® solution was then injected in the vascular channel at the flow rate of $1\,\mu\mathrm{l\,min}^{-1}$ with the aid of a syringe pump, prior to US insonation.

USMB-mediated cavitation experiments

USMB-mediated cavitation experiments were performed upon endothelial maturation, exposing the system to US in presence (USMB) or in the absence (US only) of MBs.

The experimental set-up is shown in Fig. 5.6. The microfluidic platform was placed and secured at the bottom of the insonation chamber, before filling it with previously warmed up deionised Milli-Q water. The system was then mounted onto the microscope stage. Throughout the overall duration of the experiment, water temperature was constantly monitored and maintained at 37°C with a PID (proportional integral derivative) thermal controller. The vascular channel was continuously perfused with culture medium enriched with 2.5% HEPES. Initially, the flow was maintained at the rate of $25\mu\mathrm{l\,min}^{-1}$, while cells were let adapt to the new conditions for 30 minutes (thermalisation step). During this phase, cell were monitored through time-lapse recording. Afterwards, SonoVue® suspension was injected into the microchannel and the flow rate was slowed down to 1 μl min^{-1}. This was done to match microvessel physiological conditions and to guarantee a sufficient MBs residence time over the vasculature, considering flow velocity in relation to the channel cross section in blood vessels compared to our microfluidic system. Capillary diameter typically lies in the range of $5 - 20\,\mu\mathrm{m}$, with physiological shear stress ranging from 1 to $12\,\mathrm{dyn\,cm}^{-2}$. In a 10-mm-diameter capillary, a shear stress of $10\,\mathrm{dyn\,cm}^{-2}$ corresponds to an average flow velocity $V_c = 1.25\,\mathrm{mm\,s}^{-1}$ [417]. Since our device microchannels have a cross section of $S = 100 \times 200\,\mu\mathrm{m}^2$, it can be calculated that the same physiological shear stress ($10\,\mathrm{dyn\,cm}^{-2}$) is obtained at the flow rate of $25\,\mu\mathrm{l\,min}^{-1}$. This value, however, corresponds to a flow velocity of $V_d = 20\,\mathrm{mm\,s}^{-1}$, more than ten-fold higher compared to actual microvessels ($V_c = 1.25\,\mathrm{mm\,s}^{-1}$). Therefore, keeping the MBs flowing at the same rate would have not reproduced the physiological conditions, leaving too short transit time for the MBs to produce the same effects on the endothelium. This contrast was resolved by slowing down the flow rate uniquely during the insonation period, in or-

der to reproduce capillaries conditions and to ensure a sufficient MBs transit time within the vascular channel.

When MBs reached a suitable concentration within the channel, insonation was started and stopped after 30 seconds. In the experiments with wild-type HUVECs, in order to evaluate gap opening upon exposure to US, the device was extracted from the chamber immediately after the end of the insonation and fixed with PFA under chemical hood. On the contrary, in order to evaluate the recovery phase, the microfluidic platform was placed back in the incubator after insonation and re-exposed to physiological levels of shear stress at the flow rate of $25\,\mu l\,min^{-1}$ for 45 minutes; afterwards, the endothelium was fixed with PFA and stained. In the experiments with genetically modified HUVECs, confocal fluorescence microscopy time-lapse recording was performed throughout the whole experiment to evaluate VE-cadherin dynamics. Immediately after the end of the insonation, the flow rate was re-set at $25\,\mu l\,min^{-1}$ without moving the system for 15 minutes, in order to follow the interendothelial gap dynamics and recovery.

Interendothelial gap analysis

Interendothelial gap analysis consisted in the measurement of gap number as well as of their total and mean areas in terms of pixels. For this purpose, a self-customised image analysis code was written, able to extract quantitative information from the acquired images.

The analysis protocol comprises two steps, carried out with Image J software by Fiji [414] and MATLAB Image Analysis Tool (Mathworks, MA, USA), respectively.

Initially, interendothelial gaps were visualised in the global image of the endothelium with Image J, as in Fig. 5.8A. The first part of the analysis relied on the manual identification of the gaps, as VE-cadherin pattern interruption at interendothelial junctions. Two-dimensional rectangular regions of interest (ROIs) were selected within the image of the endothelium, manually centring each of them on a single gap, as depicted in Fig. 5.8B. A TXT file was obtained as output of this selection process, listing each ROI with their coordinates, width and height. For each experimental condition, these files and the corresponding frames (TIF images) were then processed with the self-customised code. Using the information contained in the TXT file, the program crops the ROIs from the TIF image and equalises them for better contrast. Then, the resultant images are binarised through a thresholding

method, consisting in identifying all the ROI pixels above a given cut-off value as "signal", i.e. part of the gap. Connected "signal" pixels are then considered part of a single blob, which is identified as the interendothelial gap. Should the program detect more than one blob (i.e. distinct groups of connected pixels) within a single ROI, it calculates the centre of mass of each found blob. Then, it identifies the closest blob to the centre of mass of the image as the interendothelial gap, as shown in Fig. 5.8C. Hence, the code extracts quantitative information from the identified gaps, i.e. their number, the distribution of gaps number vs gap area, as well as the total and mean gap areas, returning the relative graphs, which allow to compare the different experimental conditions.

In the current image analysis approach, areas are measured and expressed in pixels. For USMB experiments with wild-type HUVECs (results reported in Fig. 5.11 and Fig. 5.12), acquired with Myo Camera at 20× magnifica-

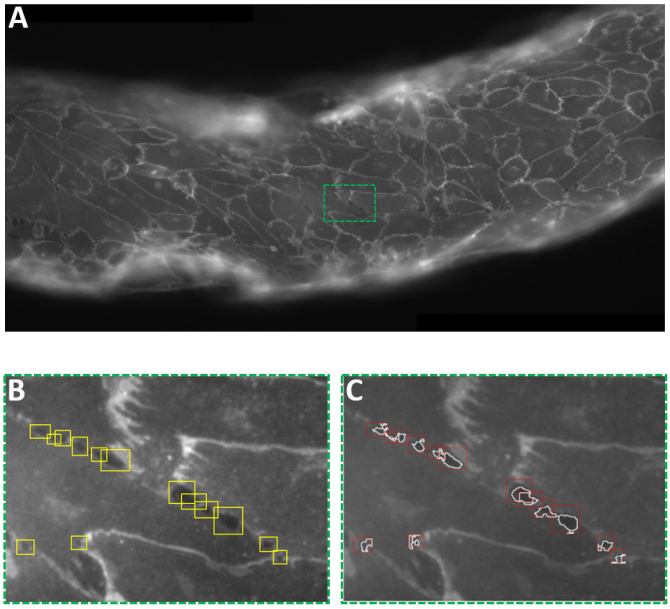

Figure 5.8: **Interendothelial gap analysis procedure. A.** Portion of the vascular channel acquired through fluorescence microscopy. **B.** Cropped image from (A), where the interendothelial gaps are identified and manually selected in Image J through rectangular ROIs. **C.** Same image as in (B), after code processing. In the TIF image, the code identifies the gap contained in each ROI and its boundaries. Image from [29].

tion, 1 pixel = $0.22 \times 0.22\,\mu m^2$. For interendothelial gap dynamics (Fig. 5.15), sampled with Prime BSI Scientific CMOS (sCMOS) camera at 20× magnification, 1 pixel = $0.325 \times 0.325\,\mu m^2$. There is no a minimum number of gaps required for the analysis, since statistical significance is evaluated by comparing the different experimental conditions with the control. Hence, all the identified gaps were included in the analysis.

For USMB experiments with wild-type HUVECs, the two conditions "US only" and "USMB" were compared with each other and with the control condition (i.e. untreated endothelium). In the USMB experiments with genetically modified HUVECs, the evaluation of VE-cadherin dynamics was also carried out over time. Five time points were thus chosen and analysed for US only and USMB conditions: at the beginning of the experiment ("control"), just before the starting of insonation ("pre-US"), at the beginning and at the end of US exposure ("US on" and "US off", respectively) and 5 minutes after the end of insonation ("Recovery").

5.2.2 Results and discussion

Characterisation of the microfluidic vascular model

A first blood vessel-on-chip model was obtained with wild-type HUVECs [28, 29]. Within the microfluidic device, cells were grown under physiological-like conditions, including continuous laminar flow exerting the same shear stress as bloodstream in microvasculature. Endothelial barrier characterisation was carried out, through the assessment of maturation features and the evaluation of interendothelial junction organisation with immunofluorescence assays. As depicted in Fig. 5.9A, after three days under physiological shear stress cells acquired a polygonal shape and clearly formed a compact monolayer, showing the cobblestone phenotype typical of a mature endothelium [418]. Cell elongation in the flow direction was also evident, indicating that cells could sense and respond to the mechanical stimuli exerted by the shear stress. Figure 5.9A shows the immunostaining of VE-cadherin (red) and F-actin (green), highlighting the formation of a cortical actin cytoskeletal network as well as VE-cadherin clusterisation at interendothelial junction complexes. In particular, VE-cadherin organisation in a linear pattern along the cell periphery is well visible. These characteristics indicated a confluent mature endothelium in resting state.

Moreover, Z-stack confocal fluorescent acquisition (with VE-cadherin and

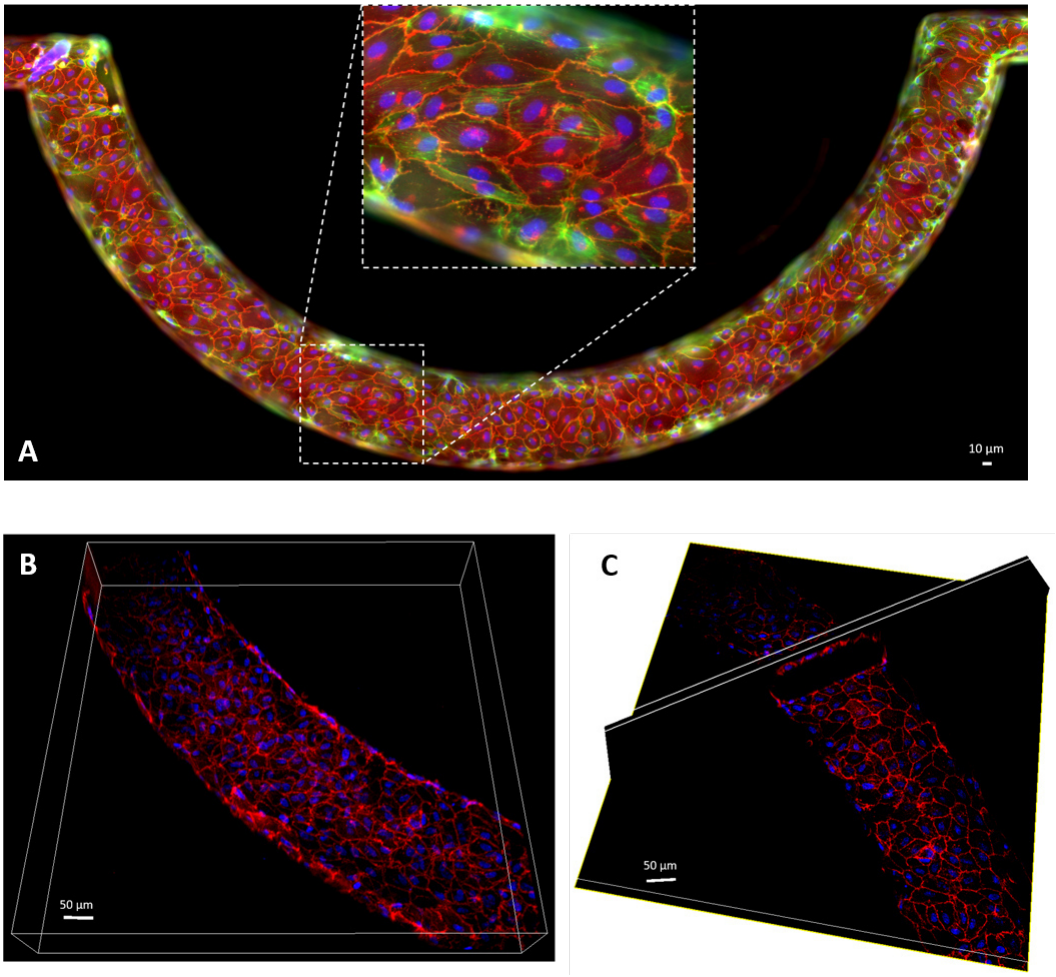

Figure 5.9: **The endothelium within the microfluidic platform, lining the walls of the vascular channel.** Cell maturation was evaluated through immunostaining of VE-cadherin (red) and actin (green). Cell nuclei are stained with DAPI (blue). **A.** Fluorescence images of the endothelial monolayer showing full-maturation characteristics. VE-cadherin is organised in a linear pattern at the cell periphery, where contacts between adjacent cells take place. Actin interacts with the interendothelial junctions, forming stress fibres and cortical filaments. Inset: highlight of the barrier maturation traits. **B** and **C.** Three-dimensional rendering of the vascular channel, obtained through Z-stack confocal acquisitions. **B.** Horizontal section of the endothelial monolayer lining the channel wall. **C.** Orthogonal view of a compound 3D figure, obtained by combining an horizontal section and a diagonal cross section of the endothelium. Images adapted from [29].

cell nuclei stained in red and blue, respectively) was used to evaluate HUVECs 3D organisation within the vascular channels. The obtained 3D rendering of the microchannel is reported in Fig. 5.9B and Fig. 5.9C. The pictures show that a single endothelial monolayer lines all the four walls of the vascular channel, enclosing a 3D vascular lumen, as in actual microvessels. Indeed, cells were grown and maintained at a flow rate of $25\,\mu l\,min^{-1}$, which was demonstrated to be optimal for the organisation of a functional endothelium. Lower flow rate were already proven inadequate to allow proper tissue maturation, while further increases provoked cell detachment from PDMS [28].

The realised system was employed for investigations on USMB-mediated endothelial permeabilisation.

Microbubbles injection and exposure to US

Upon endothelial maturation, the microfluidic platform was mounted onto the customised insonation chamber described in § 5.2.1. Once the device was secured at the bottom, in direct contact with the glass, the thermalisation step was carried out.

Afterwards, SonoVue® were injected in the vascular channel and the flow velocity was slowed down to $1\,\mu l\,min^{-1}$, to match the bloodstream velocity in capillaries and ensure a sufficient residence time of MBs within the channel (see § 5.2.1). After SonoVue® reached a sufficient concentration within the channel, the insonation was started, according to the insonation protocol.

As a first step, MBs behaviour was investigated, in order to assess their response to the acoustic field. Given the set-up of our system, we expected MBs excitation not to be altered, but to follow the theoretical models reported in Chapter 3. This is because the microfluidic device placed at the bottom of the insonation chamber was immersed in distilled water. Since PDMS acoustic impedance matches with water impedance, PDMS can be thus considered acoustically transparent and US waves are not scattered at the water/PDMS interface. Then, with good approximation, we expect the acoustic field within the microchannels to be comparable to the one in the aqueous free space outside the device.

SonoVue® distributed homogeneously to the top wall of the vascular channel (due to buoyancy), as in Fig. 5.10A. Time-lapse recording showed that US-induced radiation forces made MBs slow down and aggregate in spaced clusters, as depicted in Fig. 5.10B.

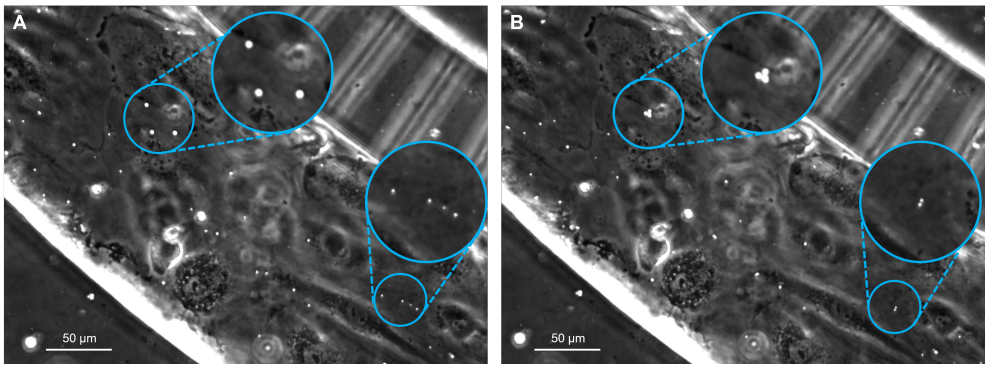

Figure 5.10: **Microbubbles response to US-induced acoustic pressure. A.** Microbubbles injected into the vascular channel before insonation. They appear as dispersed particles within the channel, distributed homogeneously. **B.** When exposed to the acoustic field, MBs aggregate in spaced clusters. *Insets* show enlargements of the encircled areas.

USMB-mediated bioeffects on interendothelial junctions

The insonation protocol is described in § 5.2.1. The endothelium was exposed to the acoustic pressure of 0.72 MPa. Since inertial cavitation threshold in these experimental conditions (fluid speed as low as 0.83 $\mathrm{mm\,s^{-1}}$) lies at 0.86 MPa [28, 419], stable cavitation occurred in the system. Two different conditions were investigated, i.e. US exposure with (USMB) and without (US only) MBs. In this regard, the microfluidic platform design is advantageous, as the presence of two VCs allows to investigate the two different experimental conditions at the same time and on the same device. This implies testing cells coming from the same seeding batch and that have undergone the same growth conditions. To this aim, during the experiment MBs are injected in one of the two VCs for the USMB condition while the other is exposed to US only.

US exposure lasted 30 seconds. At the end of insonation, when the interendothelial junction opening upon US exposure had to be evaluated, the sample was removed from the insonation chamber and placed under the chemical hood, where PFA was injected into the channels. Through this protocol, the endothelium was fixed within 4 minutes from the end of insonation. On the other hand, when the recovery of barrier integrity (i.e. gap closure) was investigated, the endothelium was further exposed to 25 $\mu\mathrm{l\,min^{-1}}$ flow at 37° for additional 45 minutes and then fixed. Afterwards, immunostaining of

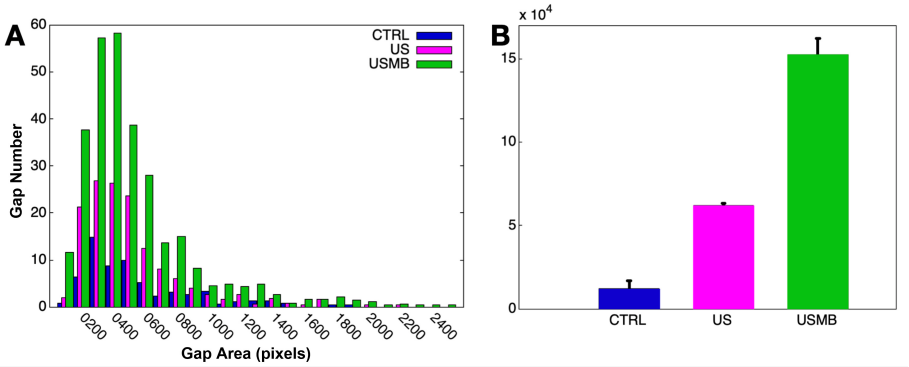

Figure 5.11: **Interendothelial junction opening.** The three conditions, i.e. US only, USMB and control, were compared. **A.** Gap number VS gap area. **B.** Total gap area opened. Areas are expressed in pixels; 1 pixel $= 0.22 \times 0.22\,\mu\text{m}^2$. Adapted from [29].

VE-cadherin was performed. The images acquired through fluorescence microscopy were stitched into a single picture of the entire vascular channel. Then, interendothelial gap analysis was carried out. As explained in § 5.2.1, an initial manual selection of the ROIs was performed through Image J. The TXT file containing the list of ROIs for each vascular channel and the correspondent TIF image were then analysed through the self-customised image analysis code, in order to quantify the opening of interendothelial gaps. Results are shown in Fig. 5.11, averaged for three samples for each condition. The histogram in Fig. 5.11A shows gap number distribution VS gap area, whereas total gap area opened for each condition is reported in Fig. 5.11B. Both USMB and US alone conditions are shown to determine a notable increase in the number of gaps and in the total opened area, compared to the control (no exposure). Notwithstanding, this effect is significantly intensified in presence of MBs. Indeed, bars in Fig. 5.11B show an increase in the total opened area by 130% and 360% for US alone and USMB conditions, respectively [28, 29].

After 45 minutes from the end of insonation the endothelium state was also assessed. Results are shown in Fig. 5.12, reporting the histogram of gap number VS gap area and the total gap area (average on three samples for each condition). Graphs highlight the total recovery of the endothelial integrity after additional exposure to physiological shear stress, with the number of gaps and their total area reverting to control conditions [28].

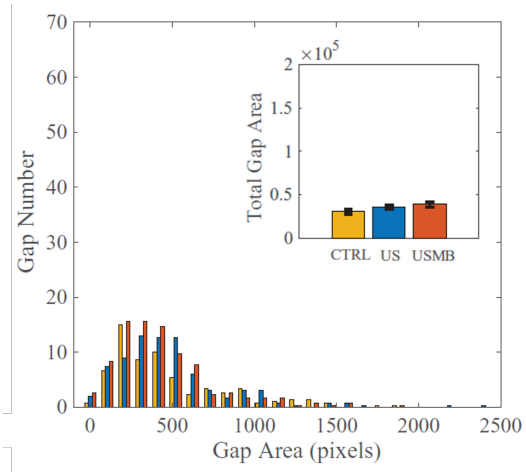

Figure 5.12: **Recovery of endothelial integrity.** Gap number VS gap area 45 minutes after insonation for US only, USMB and control condition. The inset shows the total gap area. Areas are expressed in pixels; 1 pixel = $0.22 \times 0.22\,\mu m^2$. Adapted from [28].

The total closure of the interendothelial gaps for both conditions (US only and USMB) is a significant indication of the reversibility of USMB-induced bioeffects on endothelial permeability. It also highlights the intense dynamics of interendothelial junctions, with VE-cadherin rearranging upon mechanical stimuli.

In these experiments the recovery has been evaluated 45 minutes after the insonation. However, indications exist that the gap closure can occur 30 minutes after the end of insonation [17]. It could be thus supposed that the reversion of the USMB-mediated bioeffects might start even earlier than that, on a time scale which is not totally clear yet. Therefore, the blood vessel-on-chip system was adapted for following interendothelial junctions in real time. This was accomplished by using genetically modified HUVECs expressing fluorescent VE-cadherin. In this way, the entire dynamics of interendothelial junctions can be monitored through fluorescent live imaging, following all the events of gap opening and closure as well as the relative timing.

Realisation of the blood vessel-on-chip system for live-imaging

The blood vessel-on-chip system suited for live imaging was implemented within the same device using genetically engineered HUVECs, manipulated

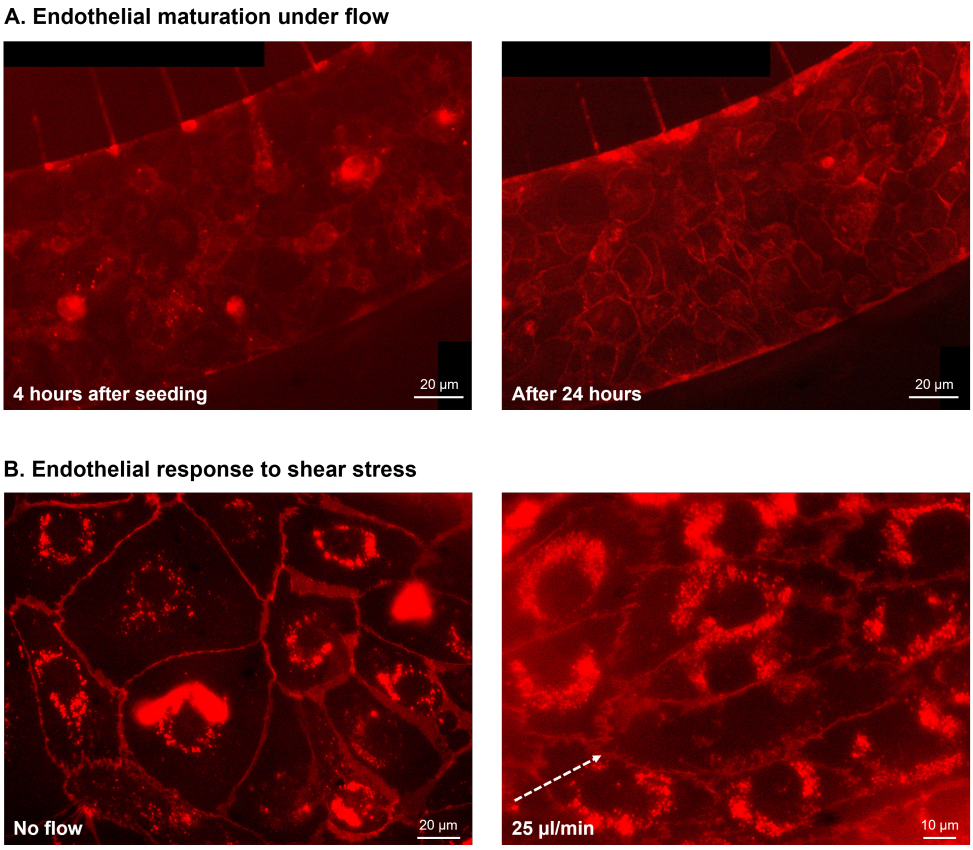

Figure 5.13: **The blood vessel-on-chip system for live-imaging.** Wide-field fluorescence live imaging of the endothelial barrier obtained with genetically modified HUVECs, expressing fluorescent mRuby-tagged VE-cadherin. **A.** Endothelial maturation under flow over the first 24 hours after seeding. *Left panel*: 4 hours after seeding. No clear VE-cadherin organisation is detectable. *Right panel*: Endothelium after 24 hours maturation under flow. VE-cadherin is organised and distributed along the cell periphery. **B.** Mature HUVECs monolayer, grown under different flow conditions. *Left panel*: HUVECs in a 2D static culture. Cells show polygonal shape without preferential directionality. *Right panel*: HUVECs grown in the vascular channel under flow at $25\,\mu l\,min^{-1}$, exerting physiological levels of shear stress ($10\,dyn\,cm^{-2}$). Cells display preferential alignment along the flow direction, indicated by the white dotted arrow.

as described in § 5.2.1. Briefly, a plasmid with a modified VE-cadherin genetic sequence was inserted into the HUVECs using a viral vector. The VE-cadherin produced through this gene is linked to mRuby, a kind of red fluorescent protein with excitation and emission peaks at the wavelengths of 558 nm and 605 nm, respectively. Hence, the VE-cadherin produced by these cells, its organisation and dynamics are clearly visible in real-time with fluorescence microscopy techniques.

Once the cells were successfully infected, they were seeded within the microfluidic device, in order to obtain a confluent monolayer under the same physiological-like conditions. Endothelial maturation was monitored over the first 24 hours after seeding through fluorescent time-lapse recording, reported in Fig. 5.13A. When fluid flow was started (4 hours after seeding, left panel), VE-cadherin signal was low and randomly distributed throughout cell cytoplasm. This poor organisation suggested that interendothelial junction complexes were not formed yet, in accordance with the early stages of the endothelial culture. After 24 hours (right panel), VE-cadherin signal appeared sharper and clearly distributed along the cell periphery. The protein also showed an organised pattern, indicating the ongoing junction rearrangement and formation process.

The shear stress influence on the endothelium was also evaluated, as showed in Fig. 5.13B. Two different conditions were compared, i.e. cells grown in a 2D static culture (no flow, left panel) and under physiological levels of flow-induced shear stress in the vascular channel (10 $\mathrm{dyn\,cm^{-2}}$, right panel). In both cases, VE-cadherin is well-organised at the cell borders and the linear pattern prevails, along with the presence of plaque-like structures. Cells within the static culture display a polygonal shape and a randomly-aligned morphology. On the other hand, when maturation occurs under physiological-like shear stress, cells acquire an elongated shape, aligning along the flow direction [155, 345].

The similarity between wild-type and genetically engineered HUVECs in terms of morphology, organisation and response to shear stress, was thus confirmed.

USMB-mediated bioeffects on endothelial barrier dynamics: preliminary results

Upon the validation of the live-imaging system, the same insonation experiments were carried out for the two conditions, i.e. US only and USMB.

The insonation chamber was modified so as to allow fluorescent microscopy to be performed. The bottom of the chamber was sealed with a glass coverslip in order to reduce the total light path (constituted of the 175 μm-thick glass coverslip and of the 1 mm-thick device glass) and match with the working distance of the 20× objective. Real-time junction dynamics was followed with confocal fluorescent time-lapse recording throughout the whole experiment. Acquisition was started before the insonation to register the behaviour and dynamics of untreated cells (control) and continued up to 15 minutes after US exposure, in order to investigate cavitation-related events over time. During the exposure to US, none of the most common optical aberrations was detected in the acquisition. Indeed, chromatic aberrations could not occur since only one wavelength was acquired, while spherical aberrations are not visible in 2D acquisition. Moreover, no other distortion was noticed.

Time-lapse recordings were then analysed for the evaluation of interendothelial gap opening, through the manual selection of the gap-containing

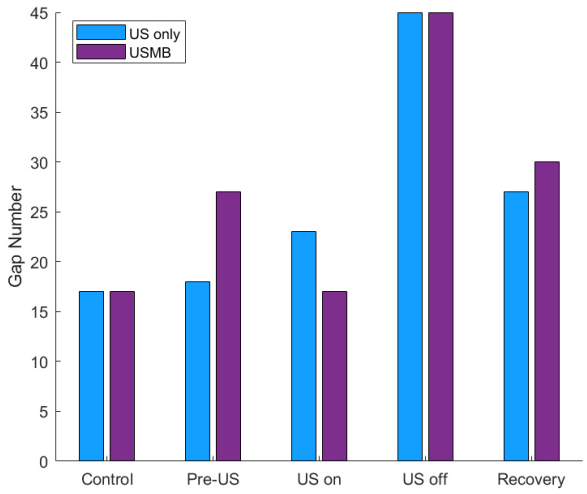

Figure 5.14: **Gap number over time**. The graph shows the number of gaps opened at each time point for US only (blue) and USMB (purple) conditions, with respect to the beginning of the experiment. *Control:* Beginning of the experiment; *Pre-US:* prior to US exposure; *US on:* start of insonation; *US off:* end of insonation; *Recovery:* 5 minutes after insonation. N=1 (preliminary data).

ROIs and the self-customised image analysis code. Since this investigation regards junction dynamics over time, five different instants were chosen for the analysis of the time-lapse frames: the beginning of the recording ("Control"), just prior to US exposure ("pre-US"), at the beginning of the insonation ("US on"), at the end of the insonation ("US off") and 5 minutes after the end of US ("Recovery").

Results are shown in Fig. 5.14 and Fig. 5.15. The number of gaps, Fig. 5.14, remains constant until insonation, consistently with the endothelium having reached a mature configuration. After exposure to US for 30 s, the number of gaps increased significantly for both conditions. During the recovery phase, their number tends to decrease, indicating their closure. A similar trend is followed by the total and mean areas of the opened gaps, reported in Fig. 5.15. Since US only and USMB conditions were evaluated in distinct vascular channels, data were normalised to the relative control, to account for the differences between the two samples. As it can be seen, exposure to US in presence of MBs determined a notable increase in the opened gap area compared to the US only condition. The successive reversion of the phenomenon was also detected, as shown in Fig. 5.15A.

These preliminary results indicate the suitability of the system for the investigation of the USMB-mediated effects on the endothelium and their dynamics. The detection of a recovery dynamics already 5 minutes after the end of insonation suggests that the time scale of these events might be

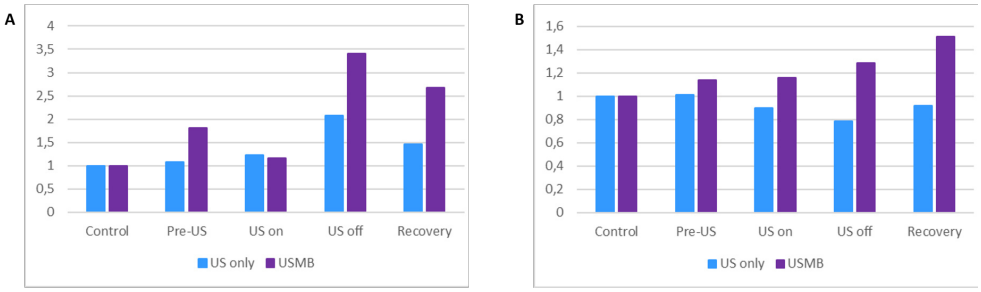

Figure 5.15: **Total and mean gap areas.** Histograms showing the normalised total (**A**) and mean (**B**) area of the opened gap over time, for US only (blue) and USMB (purple) conditions. *Control:* Beginning of the experiment; *Pre-US:* prior to US exposure; *US on:* start of insonation; *US off:* end of insonation; *Recovery:* 5 minutes after insonation. Areas are expressed in pixels; 1 pixel = $0.325 \times 0.325\,\mu m^2$. N=1 (preliminary data).

faster than previously stated, allowing the endothelial barrier to reacquire its integrity shortly after exposure to US. It is probable that continuous rearrangement of interendothelial junctions occurs in response to the mechanical stimuli triggered by the acoustic field.

5.3 GUVs production through microfluidics

This last section is focused on the second microfluidic platform presented in this project, for the production of GUVs as an experimental model of phospholipid bilayer. Aim of this PhD project is the device realisation, with the choice of a suitable geometry for the formation of a W/O/W double emulsion template and the establishment of the relative experimental protocol. After assessing GUVs formation, vesicles will be initially visualised through optical microscopy and measured. The final aim consists in optimising an optical set-up and protocol for the successive thermal fluctuation analysis, which will be performed to characterise some biomechanical features of the phospholipid bilayer.

5.3.1 Experimental set-up

Hydrophilic treatment of the device microchannel

Before GUVs generation, the external microchannels and the second junction of the device underwent a hydrophilic surface treatment, in order to stabilise the vesicles to form [89, 420]. This was done using polyvinyl alcohol (PVA) ($87.0 - 89.0\%$ hydrolyzed, M.W. approx. $31000 - 50000$) (Fisher Scientific, PA, USA). PVA solution was prepared dissolving PVA powder in filtered Milli-Q distilled water ($0.22\,\mu$m filters) at the concentration of $50\,\mathrm{mg\,ml^{-1}}$. It was gently stirred at 85°C for 30 minutes, in order to favour PVA dissolution.

To carry out the hydrophilic treatment, a drop of PVA solution was poured onto the outlet of the microfluidic device, while empty syringes were connected to I_1 and I_3 inlets (see Fig. 5.2). Negative pressure was generated with the syringe connected to I_3, withdrawing PVA into the outer channel. With the syringe connected to I_1, air was injected into the channel to prevent PVA from flowing towards the coil, confining it to the second junction. After wetting the PDMS walls with PVA, it was carefully removed through air injection and the device was baked at 120°C for 15 minutes, in order to fully dry it and increase the bonding strength of the coating.

Solution preparation

Vesicles were composed of 1-palmitoyl-2-Oleoyl-*sn*-glycero-3-phosphocholine (POPC) (Sigma-Aldrich, MO, USA). After weighing pospholipids in a glass vial, they were initially dissolved in 1 ml chloroform (Sigma-Aldrich, MO, USA), which was then dried under a stream of nitrogen while keeping the vial at $\sim 45°$ and constantly rotating it, in order to obtain a lipid film on its walls. With the aim to completely remove any chloroform residue, the lipid film was kept under vacuum overnight, afterwards, it could either be used immediately or stored at $-20°$C. Solutions to obtain the W/O/W emulsion were prepared as follows. The inner aqueous solution is composed of filtered Milli-Q water and Pluronic^{TM} F-68 (Gibco^{TM}, Thermo Fisher Scientific, MA, USA), in 1:1 proportion. 0.05% Texas Red fluorescent dye (labelled dextran, 40 kDa) (Invitrogen, Thermo Fisher Scientific, MA, USA) was added to allow the successive visualisation and identification of the formed GUVs. The oil phase was obtained by dissolving the lipid film in oleic acid (Sigma-Aldrich, MO, USA) at the concentration of $5\,\mathrm{mg\,ml^{-1}}$. The external aqueous phase is composed of POPC lipids dissolved at $3\,\mathrm{mg\,ml^{-1}}$ in a mixture of 2.85%v/v Pluronic F-68, 14%v/v glycerol (Sigma-Aldrich, MO, USA),14%v/v ethanol absolute anhydrous (CARLO ERBA Reagents S.r.l., Italy) and filtered Milli-Q water.

In order to facilitate lipid resuspension, the oil and the external aqueous phases were vortexed for 1 minute (at 25 Hz for the oil phase and 20 Hz for the external aqueous phase) and then underwent 1-hour sonication bath at RT. In particular, the external aqueous solution was sonicated before the addition of its different components, immediately after lipid dissolution into deionised water. The other reagents were added after the sonication bath. This choice is justified by the fact that the ultrasound-induced heating can cause molecular damages or allow collateral chemical reactions to happen without control.

GUVs production through microfluidics

The three solutions were loaded into plastic syringes and connected to the device inlets through Tygon tubes; each syringe was then mounted on a syringe pump. A short Tygon tube was connected to the device outlet for the collection of the formed GUVs into a 1.5-ml Eppendorf tube. The device was finally placed onto the stage of a Observer Z1 inverted microscope (Zeiss,

Germany).

Flows were started. The inner aqueous solution (I_1) was flowed first into the device, at the rate of $1.7\,\mu l\,min^{-1}$, followed by the oil phase (I_2) at $2.1\,\mu l\,min^{-1}$. Time was given for the two flows to stabilise within the device, until the oil phase started shearing the inner aqueous phase at the first junction, generating a W/O emulsion flowing into the device coil. At this point, the third solution (I_3) was flowed at $70\,\mu l\,min^{-1}$, shearing the single emulsion at the second junction. The W/O/W double emulsion was thus formed and collected. The process of W/O/W double emulsion formation leaves oil residues within the phospholipid phase, due to the favourable interactions between the hydrophobic molecules. Being oleic acid soluble in ethanol, the emulsion was then incubated in its outer solution. Indeed, ethanol favoured the extraction of oleic acid residues, leaving a well organised phospholipid bilayer and finalising GUVs formation, as described in [390] and [89].

In some experiments, glucose at different concentrations was added to the solution after GUVs formation, in order to monitor their variations. Glucose powder (Sigma-Aldrich) was dissolved in filtered ($0.22\,\mu m$ filters) deionised Milli-Q water, with the aid of magnetic stirring. Two solutions were prepared, one at the concentration of 500 mM, and the other at glucose solubility limit ($0.13\,g\,ml^{-1}$, according to manifacturer's product information). The solutions were added to formed GUVs directly into the Ibidi wells, immediately before microscope visualisation.

Optical set-up

GUVs formation was monitored in real time through a Observer Z1 inverted microscope (Zeiss), provided with the high speed camera FASTCAM Mini UX100 (1280×1024 px CMOS sensor) (Photron, CA, USA). Images and time-lapse recordings related to the formation process were acquired at $20\times$ magnification.

Sampling of the formed GUVs was performed using an inverted Olympus iX73 microscope, equipped with X-light V1 spinning disk head (Crestoptics) and LDI laser illuminator (89 North), through $10\times$, $20\times$ and $40\times$ air objectives and MetaMorph software (Molecular Devices).

For visualisation, GUVs were loaded onto a Ibidi μ-Slide 8 Wells Chamber (Ibidi, Martinsried, Germany) with a $180\,\mu m$-thick polymer bottom. Both fluorescent and phase contrast images were acquired with a Prime BSI Scientific CMOS (sCMOS) camera with $6.5\,\mu m$ pixels (Photometrics) and then

processed with Image J software. Time-lapse recordings were acquired in phase contrast with 20× and 40× air objectives.

Measurement of vesicle size and size distribution

An image processing and analysis protocol was defined in order to measure the size of the formed GUVs through MetaMorph software. For this purpose, images acquired at different magnification (either 10× or 20×) and in different experiments were used, as in the example of Fig. 5.16A.

A manual intensity threshold was initially applied to fluorescent images in order to isolate the Texas-Red-containing GUVs and erase the background. The thresholded images were then turned into a 8-bit binary mask, where "signal" pixels (corresponding to GUVs) were assigned a value of intensity

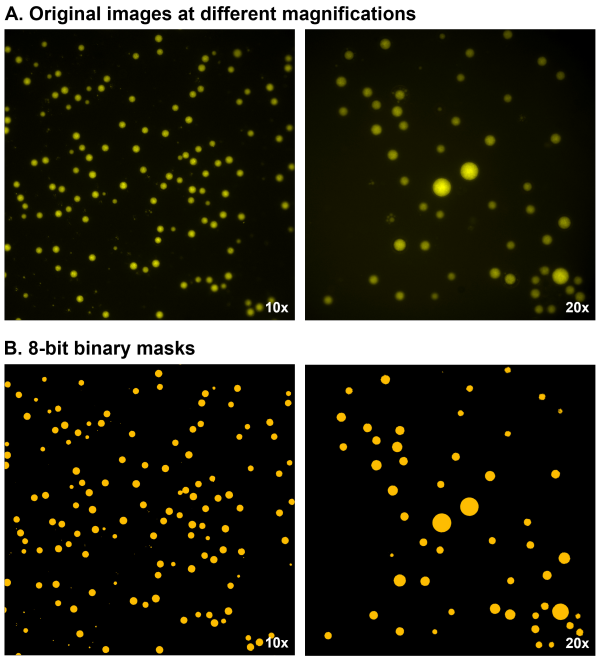

Figure 5.16: **Image processing and analysis protocol to measure GUVs size. A.** Either 10× (left panel) or 20× (right panel) images can be used to measure GUVs size through MetaMorph software. **B.** 8-bit binary masks obtained from the same images in (A) after thresholding and binarising. GUVs appear as orange particles (pixel intensity = 255) while the black background has pixel intensity value of 0.

of 255, while background pixels were equal to 0, as shown in Fig. 5.16B. Then, a filter on objects area was set, excluding from the measurement all the particles with area (in pixel) below 1000 or 2000 pixel for 10× and 20× magnification, respectively (1 pixel = $0.65 \times 0.65\,\mu m^2$ for 10× magnification and $0.325 \times 0.325\,\mu m^2$ for 20× magnification). This was done in order not to take into account possible debris in the analysis. Comparing the obtained mask with the original image, blurred GUVs were manually excluded from the measurement. Hence, the radius of the identified particles could be measured through the MetaMorph software, which, considering the pixel size for the used CCD camera and magnification, returns each length in nanometres. In particular, since not all GUVs appeared to have a perfectly round shape, their equivalent radius was used for the quantification of their size.

Then, the normal distribution of GUVs diameters was calculated through the MATLAB App Distribution Fitter. The Probability Density Function (PDF), the mean value and the standard deviation of GUVs diameters were obtained.

For the results reported in § 5.3.2, the diameters of 152 GUVs were measured.

5.3.2 Results and discussion

Microfabrication and hydrophilic treatment of the microfluidic device

The geometry of the microfluidic platform (Fig. 5.2) was designed through CAD and the device was self-fabricated by soft lithography.

Before the experiment, the device was subject to a hydrophilic treatment.

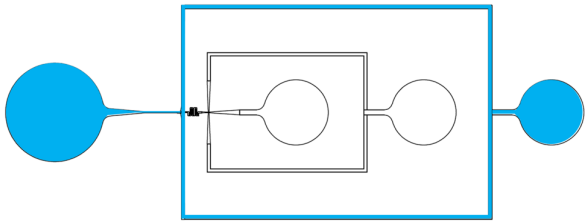

Figure 5.17: **Hydrophilic treatment of the microfluidic device.** The external channel (blue) was coated with PVA before GUVs formation, in order to make PDMS surface more hydrophilic and favour GUVs stabilisation.

Since PDMS is inherently hydrophobic, unfavourable interactions can occur between the PDMS walls and the phospholipid polar heads, resulting in the formed GUVs destabilisation. The external channel was thus coated with PVA, as shown in blue in Fig. 5.17. This treatment guaranteed the complete wetting of the PDMS walls by the aqueous phase and prevented GUVs rupture.

GUVs formation

GUVs formation was performed through the W/O/W double emulsion template. Solution composition was found to be crucial for the proper interactions among the different phases, as described in § 4.3. Texas Red, a red-fluorescent dye conjugated with dextran with a molecular weight of 40 kDa, was encapsulated within the GUVs by adding it to the internal aqueous

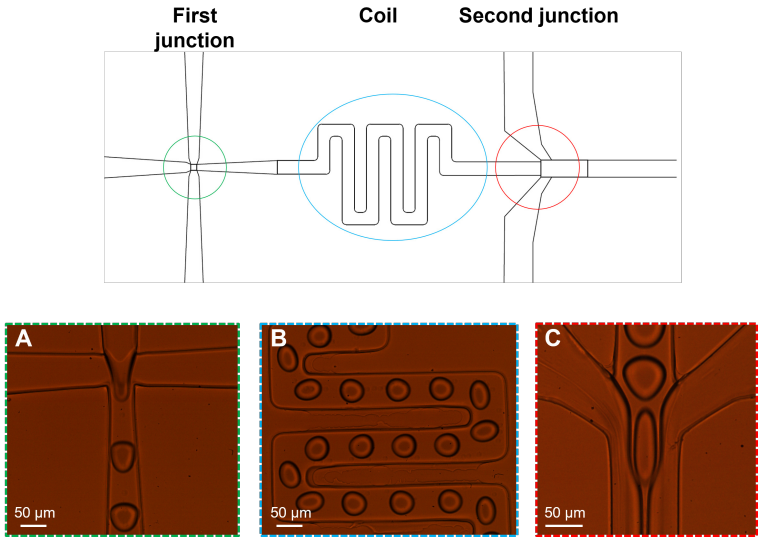

Figure 5.18: **GUVs formation within the microfluidic device.** Sketch of the core of the device geometry with the relative optical microscopy images acquired during GUVs formation process. **A.** First junction, where the W/O single emulsion is formed through the shearing of the internal aqueous solution by the oil phase. **B.** Channel meander, where W/O droplets are stabilised and lipids organise around the aqueous phase. **C.** Second junction. The intersection with the external aqueous phase allows the addition of the second phospholipid layer for GUVs formation through a W/O/W template.

phase. Its size prevents this molecule to cross phospholipid bilayers, hence, it allowed to observe the formed GUVs through fluorescence microscopy.

Upon solutions injection, the dynamics of GUVs formation was followed. At the first junction, the internal aqueous solution was sheared by the oil phase, eventually bringing to the detachment of a W/O droplet, as shown in Fig. 5.18A. The flow rate of the solutions was shown to crucially affect this step. Indeed, different tested combinations of flow rate values did not allow solution shearing and droplet formation. Finally, flow rate values of $1.7\,\mu\mathrm{l\,min^{-1}}$ and $2.1\,\mu\mathrm{l\,min^{-1}}$ were set for the inner aqueous and oil phases, respectively. Small variations from these values were also shown to influence GUVs size. The formed W/O droplet flowed through the channel meander between the two junctions, as in Fig. 5.18B. This structure was

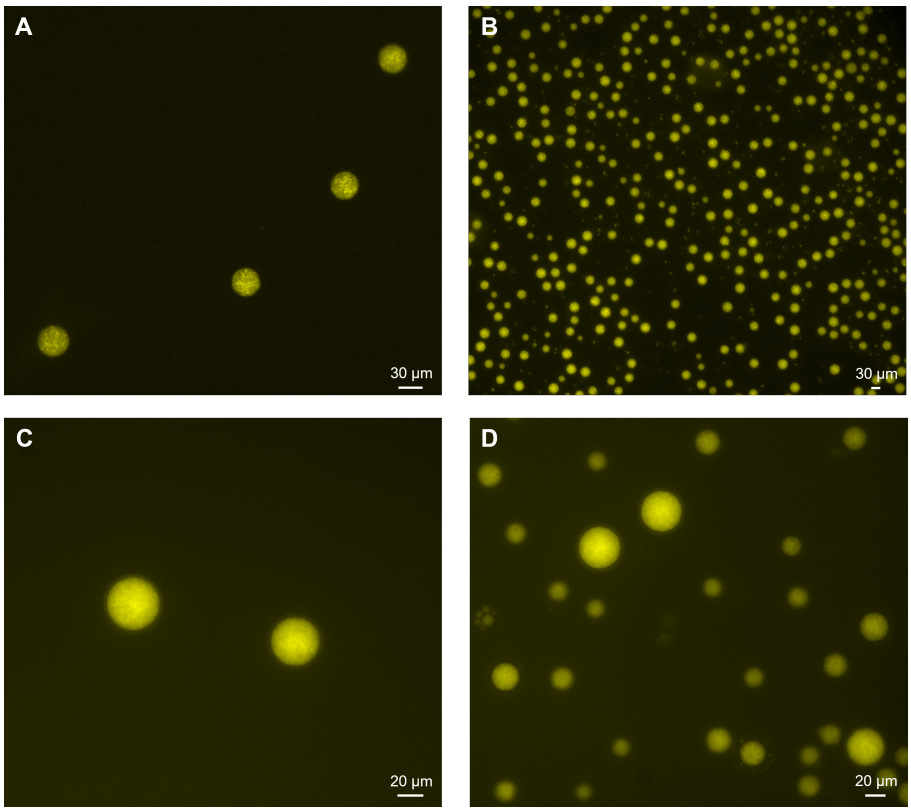

Figure 5.19: **Fluorescent bright-field images of the formed GUVs.** GUVs stained with Texas Red acquired at 10× (**A** and **B**) and 20× (**C** and **D**) magnifications.

shown to favour the organisation of a single phospholipid monolayer around the aqueous droplet [27]. At the second junction, Fig. 5.18C, the external lipid-carrying aqueous solution intersected with the flowing W/O droplets, adding the external phospholipid monolayer. Flow rates in the range of $50 - 70\,\mu l\,\mathrm{min}^{-1}$ successfully allowed the formation of the W/O/W, although a rate of $70\,\mu l\,\mathrm{min}^{-1}$ guaranteed a higher GUVs yield. The formed GUVs were thus collected. After the incubation for the extraction of oil residues, they were visualised through optical microscopy.

GUVs microscopy visualisation and size distribution

Once formed, GUVs were visualised through fluorescence and phase contrast microscopy. Image acquired at different magnifications are shown in Fig. 5.19 and Fig. 5.20, respectively.

Fluorescence images were analysed as described in § 5.3.1 to measure GUVs size and diameter distribution. Four images at different magnification (three at 10× magnification and one at 20× magnification) from three different experiments were processed and analysed and the size of 152 GUVs was measured. The normal distribution of their diameters is reported in Fig. 5.21. The mean diameter was estimated to be $29.76 \pm 0.39\,\mu$m, with a standard deviation $\sigma = 4.81 \pm 0.28\,\mu$m. In general, GUVs size was found to fall within the range of $20 - 40\,\mu$m, in accordance with the size of the two flow-focusing junctions. An image analysis code is currently under develop-

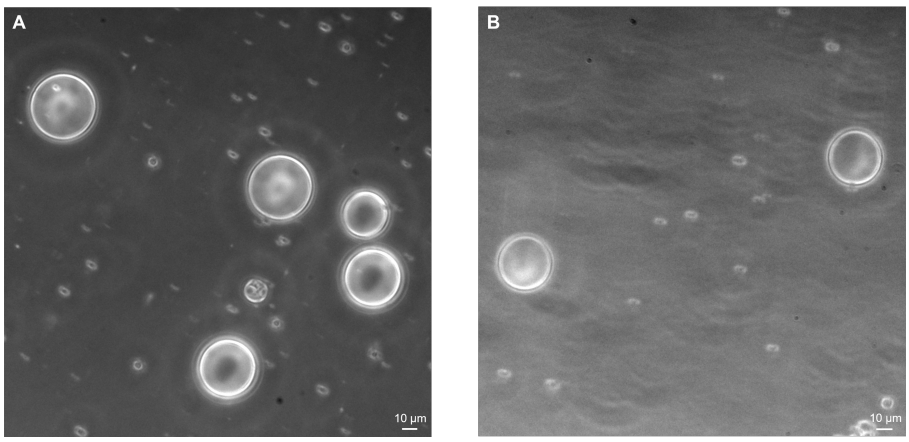

Figure 5.20: **Phase contrast images of the formed GUVs.** Phase contrast microscopy acquisition of GUVs at 40× magnification.

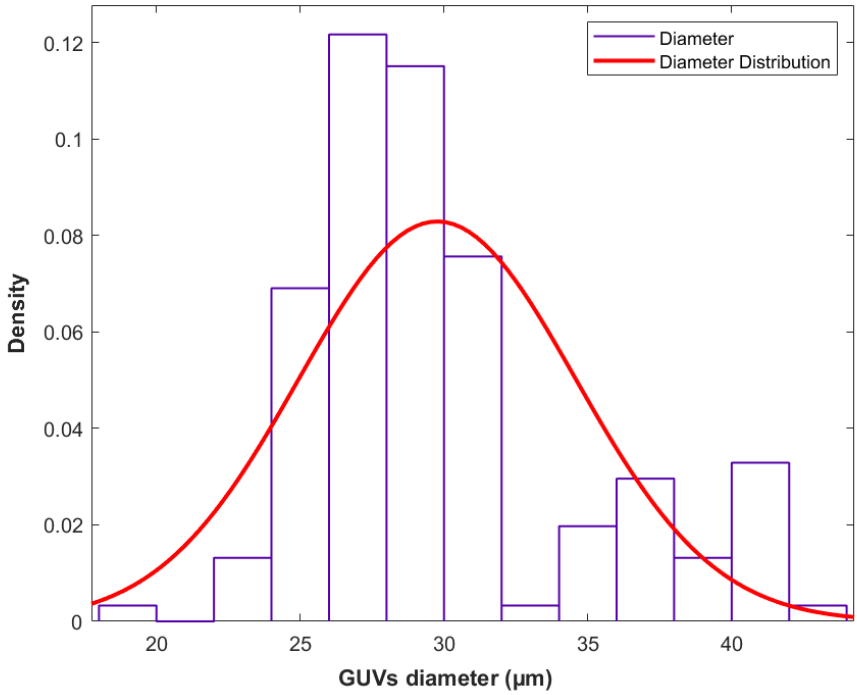

Figure 5.21: **GUVs diameter distribution.** Normal distribution of the diameters of formed GUVs, obtained through image processing and analysis of four fluorescence images at different magnification (10× and 20× from three different experiments). A total amount of 152 GUVs was analysed, with a mean diameter of $29.76 \pm 0.39\,\mu$m and standard deviation $\sigma = 4.81 \pm 0.28\,\mu$m.

ment to automatically identify vesicle shape and measure their size, in order to extract information about their physical features.

After GUVs formation, tests were made varying solute concentrations in the external solution. This was aimed at evaluating the effect on membrane behaviour, in order to find the best conditions for TFA experiments and bilayer biomechanical characterisation. For this purpose, glucose solutions at the concentration of 500 mM and at its solubility limit were used, adding them to the external solution after GUVs formation. Results are reported in Fig. 5.22. As it can be observed, increasing glucose concentration progressively exacerbated a peculiar membrane appearance, i.e. the thickening of the outermost vesicle portion. Two possible explanations were hypothesised for

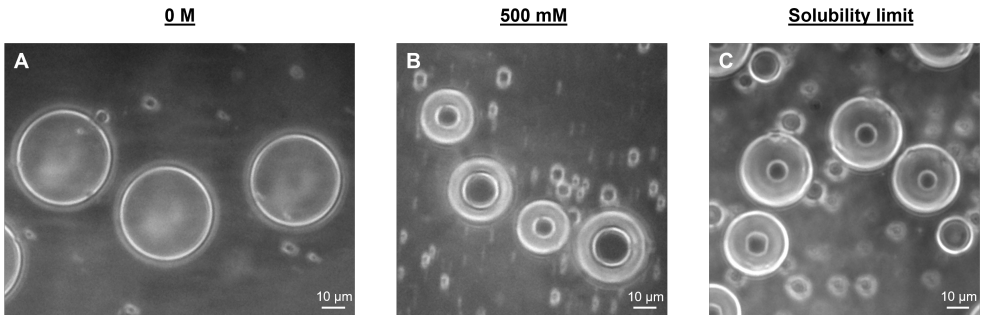

Figure 5.22: **GUVs at different glucose concentrations.** Upon GUVs formation, glucose solutions at different concentrations were added to the bulk solution to evaluate the effects on the membrane behaviour. Phase contrast microscopy images were acquired at 40× magnification. **A.** Untreated GUVs (no glucose addition). **B.** Addition of 500 mM glucose solution. **C.** Addition of glucose solution at its solubility limit.

this phenomenon. A first hypothesis involves the possibility of bilayer damage, as if the two leaflets tended to detach. Another explanation is related to a water flux from GUVs interior to the external solution, possibly triggered by the higher solute concentration. This might reduce vesicle swelling and determine an increase in membrane fluctuation amplitude, so that a different acquisition protocol may be required to detect the oscillations.

In general, optimisation of the microscopy set-up is in progress to carry out thermal fluctuation analysis. In parallel, an image analysis strategy is currently being designed for the standardised identification and extraction of membrane boundaries, in order to measure their fluctuations over time. This will allow the calculation of membrane bending rigidity modulus κ (discussed in Chapter 2, § 2.1.2 and § 2.1.3) and thus the characterisation of some membrane biomechanical features.

Chapter 6

Conclusions and future perspectives

Biological barriers impair the efficiency of currently employed therapeutic strategies by hindering drugs from reaching their target site. The development of drug delivery strategies to enhance their permeability has thus been a goal of pharmaceutical research. Since barrier biomechanical features regulate their behaviour and influence their permeability, suitable experimental *in vitro* models are necessary to recapitulate these characteristics and test new therapeutic approaches in biologically relevant contexts.

In this light, this PhD thesis consisted in two different project lines, employing microfluidics to develop experimental models recapitulating the characteristics of two fundamental biological barriers. The first one (the blood vessel-on-chip), part of an already ongoing work in our group, was intended to evaluate the dynamics of interendothelial junction opening upon USMB-mediated cavitation. The other one, which was developed *ex novo*, was devoted to the high-throughput production of GUVs to be employed to characterise some biomechanical features of phospholipid bilayers.

In the first project line, an endothelium lining the PDMS walls of the device microchannels, forming a perfusable lumen, was obtained. Initially, I contributed to the work in progress, based on immunofluorescence assays to quantitatively evaluate the endothelial permeabilisation after exposing the experimental system to US in presence or absence of MBs. In order to obtain the endothelial barrier, HUVECs were grown under constant flow exerting physiological levels of shear stress, which was proven to crucially affect their maturation and morphology. The relevance of this mechanical

stimulus was assessed through immunofluorescence assays, which highlighted the proper organisation of junction complexes and the characteristic VE-cadherin configuration in a linear pattern at the cell periphery.

This endothelial model system was employed to investigate the effect of USMB-triggered stable cavitation phenomena, with linear MBs oscillation and the consequent generation of microstreaming and related shear stress. Previous experimental evidence had already shown that this mechanical action induces the reorganisation of ECs junctions and the opening interendothelial gaps [17, 250]. Hence, we developed a self-customised image analysis code to quantitatively evaluate the number of gaps and their area opened upon endothelial exposure to US in presence or in absence of MBs. The opened gaps were visualised through immunofluorescence assays on cells fixed immediately after insonation. Interendothelial gaps were manually selected using rectangular ROIs which were successively processed through the image analysis code. In the present work, attention was focused on the gap area as the observable to quantify the effects of exposure to USMB on endothelial permeability. For this reason, the analysis was performed on 2D fluorescence images. In the future, it will be of interest to carry out a similar analysis on the 3D stacks of the endothelial barrier, so as to fully appreciate junction rearrangements on the whole tissue. Moreover, we are currently working on the code to implement the automatic recognition of the interendothelial gaps. Results show that, although the exposure to US alone already accounts for gap opening in the endothelium, the presence of MBs significantly strengthens this effect, inducing an increase in the total opened area by 360% compared to untreated conditions. Furthermore, the recovery of the endothelial barrier integrity was investigated re-exposing the endothelium to physiological levels of shear stress after the insonation. The complete closure of the interendothelial gaps was found after 45 minutes. On the basis of this result, we focused on the dynamics of these events, in order to shed light on the time scale of interendothelial junction reorganisation. The system employed initially was not suited for this investigation, since the endothelium needed to be fixed for the immunofluorescence assays to visualise the gaps. Hence, we adapted it for live imaging, by tagging VE-cadherin with fluorescence. This part was developed *ex novo* in this PhD project and was achieved through stable infection with a viral vector, for the insertion of a plasmid for fluorescent VE-cadherin expression. Genetically modified HUVECs were seeded within the microfluidic platform to perform live-imaging-based investigations. Indeed, we were able to follow

VE-cadherin dynamics over time, including during the endothelial maturation stages, confirming the suitability of this model for real-time imaging. The system capacity to reproduce a physiological endothelial barrier was assessed on the basis of the morphological and structural similarities with the previously characterised blood vessel-on-chip. The morphology of the engineered ECs was observed, confirming their elongation and the alignment of their long axis in the flow direction. In addition, VE-cadherin organised in a linear pattern, demonstrating proper junction organisation and responsiveness of the endothelium to physiological shear stress. These observations provided promising indications of the physiological behaviour of our system. The functional characterisation of this model is currently in progress to confirm the integrity and functionality of the genetically engineered endothelial barrier, through the assessment of its permeability, as described in § 4.2.1 (Fig. 4.5). After setting up the live-imaging system, USMB-induced stable cavitation experiments were performed while constantly monitoring the endothelium through confocal fluorescent microscopy. Experiments are currently in progress, along with the concomitant optimisation of the optical set-up and the image analysis procedure, to be adapted to the new dynamic investigation. Preliminary results align with previous evidence, showing an increase in the number of gaps and in the total area opened compared to control conditions. In particular, the presence of MBs seems to account for the opening of larger gaps, compared to the US only condition. Indeed, gap area seems to increase even after the end of insonation (Fig. 5.15B), possibly indicating general and constant VE-cadherin rearrangements, triggered by the USMB-mediated mechanical stimulation. Moreover, fluorescence time-lapse recordings allow to detect the reversion of these biological effects already 5 minutes after the end of insonation, suggesting that the dynamics of gap closure might be faster than previously assessed. In fact, while the adaptation of the system for live imaging was successfully accomplished, data collection is in progress to evaluate junction dynamics in the two experimental conditions, also in comparison with the previously obtained results (e.g. the trend of gap number in Fig. 5.14, which appears to differ from Fig. 5.11). This will also provide an accurate estimation of the recovery rate of the gaps.

Furthermore, the present investigation highlighted cavitation efficiency in enhancing endothelial permeability. Most importantly, this effect is temporary and reversible, making the cavitation-based approach suitable for possible employment as a drug delivery strategy. In this light, microfluidic platforms, like the one presented in this thesis, might be supporting tools for

the development of clinical protocols taking into account the safety and the potential hazard of tissue exposure to US (e.g. bleeding, apoptosis, necrosis). This is also endorsed by the flexibility of these devices. Beyond physiological models, they can be exploited to reproduce pathological microenvironments (e.g. tumour-vasculature interface) and to test the interactions of drugs and their carriers with the endothelial barrier.

The second PhD project line consisted in the realisation of a microfluidic platform for the production of an experimental model of plasma membrane. The aim is to carry out investigations on its biomechanical properties, through the measurement of the bending rigidity modulus, κ. GUVs were chosen as model system for their high biomimicry of natural membranes. Hence, we developed and tested an experimental set-up for their production. The W/O/W double emulsion template was chosen due to its easy implementation within microfluidic platforms and to its capacity to yield stable, monodispersed GUVs [26]. The device geometry was thus optimised for the double emulsion formation, thanks to the two consecutive flow-focusing junctions. They allowed the controlled interaction of the immiscible solutions and the consequent phospholipid organisation at the two interfaces between the oil and the aqueous phases. The composition of the three solutions was also tested and proven to be suitable for vesicle production. In particular, ethanol was a key component for the final GUVs formation, as it determines the extraction of oil residues from the bilayer. In other works, mixtures of organic solvents, i.e. toluene and chloroform or tetrahydrofurane, have been used to accomplish this step [26, 396]. The use of ethanol with oleic acid, reported in [390] for the first time, avoids the use of toxic solvents and also makes the produced GUVs biocompatible.

The high encapsulation efficiency provided by this method [26] was exploited to enclose dextran-conjugated Texas Red fluorescent dye within the vesicles for fluorescence microscopy visualisation.

The dimension of the two flow-focusing junctions as well as the flow rates of the oil and the external aqueous phases provided control over GUVs size. A preliminary image analysis allowed to estimate the diameter of the produced GUVs and the relative dispersion, through fluorescence images binarisation with a thresholding approach and the successive measure of GUVs physical quantities, including their radius. In particular, since GUVs did not always show perfect spherical shapes, their equivalent radius was quantified in this first analysis. The diameter of the formed GUVs ranged from 20 to 40 μm,

with a mean value of $29.76 \pm 0.39\,\mu$m and a standard deviation $\sigma = 4.81 \pm 0.28\,\mu$m. An image analysis algorithm is under development to automatise this measurement, identifying the fluorescent GUVs and characterising them in terms of shape and size.

We are also planning to evaluate whether changes in solute concentration in the formed GUVs solution can affect the movement of the phospholipid bilayer and, hence, its fluctuations. Moreover, the optimisation of the optical set-up for phase contrast microscopy is currently ongoing. The aim is to maximise the resolution of the acquisition for the successive thermal fluctuation analyses, which will be performed. Along with this, we are setting-up an appropriate image analysis protocol to isolate the vesicle contour (i.e., the phosphplipid bilayer) in order to easily measure its fluctuations from the equilibrium position. Indeed, by recording and measuring membrane motion over time, it is possible to extract information regarding the bilayer biomechanics. In particular, κ is an important indicator of membrane rigidity and resistance to variations from its spontaneous curvature. These biomechanical features have been shown to play a key role in several cell processes involving the membrane, such as endocytosis [58].

In conclusion, in this PhD project a new platform was developed, which provides a valid tool for the high-throughput production of monodispersed GUVs with adjustable characteristics. Possible future developments might exploit the versatility provided by this system to better mimic membrane composition in terms of lipids and embedded proteins, in order to measure κ in physiologically relevant conditions.

List of publications

- Grisanti, G., Caprini, D., Sinibaldi, G., Scognamiglio, C., Silvani, G., Peruzzi, G., & Casciola, C. M. (2021). "A Microfluidic Platform for Cavitation-Enhanced Drug Delivery". *Micromachines*, 12(6), 658.

- Parlato, S., Grisanti, G., Sinibaldi, G., Peruzzi, G., Casciola, C. M., & Gabriele, L. (2021). "Tumor-on-a-chip platforms to study cancer-immune system crosstalk in the era of immunotherapy". *Lab on a chip*, 21(2), 234–253.

Bibliography

[1] Vladimir P Torchilin. Drug targeting. *European Journal of Pharmaceutical Sciences*, 11:S81–S91, 2000.

[2] Anne Krüger-Genge, Anna Blocki, Ralf-Peter Franke, and Friedrich Jung. Vascular endothelial cell biology: an update. *International journal of molecular sciences*, 20(18):4411, 2019.

[3] Daniela Salomon, Oran Ayalon, Ramila Patel-King, Richard O Hynes, and Benjamin Geiger. Extrajunctional distribution of n-cadherin in cultured human endothelial cells. *Journal of cell science*, 102(1):7–17, 1992.

[4] Elisabetta Dejana et al. Endothelial adherens junctions: implications in the control of vascular permeability and angiogenesis. *The Journal of clinical investigation*, 98(9):1949–1953, 1996.

[5] Garth L Nicolson. The fluid—mosaic model of membrane structure: Still relevant to understanding the structure, function and dynamics of biological membranes after more than 40 years. *Biochimica et Biophysica Acta (BBA)-Biomembranes*, 1838(6):1451–1466, 2014.

[6] Anabel-Lise Le Roux, Xarxa Quiroga, Nikhil Walani, Marino Arroyo, and Pere Roca-Cusachs. The plasma membrane as a mechanochemical transducer. *Philosophical Transactions of the Royal Society B*, 374(1779):20180221, 2019.

[7] Jeffrey K Mills and David Needham. Targeted drug delivery. *Expert Opinion on Therapeutic Patents*, 9(11):1499–1513, 1999.

[8] Theresa M Allen and Pieter R Cullis. Drug delivery systems: entering the mainstream. *Science*, 303(5665):1818–1822, 2004.

[9] Rong Yang, Tuo Wei, Hannah Goldberg, Weiping Wang, Kathleen Cullion, and Daniel S Kohane. Getting drugs across biological barriers. *Advanced Materials*, 29(37):1606596, 2017.

[10] Klaus Strebhardt and Axel Ullrich. Paul ehrlich's magic bullet concept: 100 years of progress. *Nature Reviews Cancer*, 8(6):473–480, 2008.

[11] Yeon Hee Yun, Byung Kook Lee, and Kinam Park. Controlled drug delivery: historical perspective for the next generation. *Journal of Controlled Release*, 219:2–7, 2015.

[12] Martin P Stewart, Armon Sharei, Xiaoyun Ding, Gaurav Sahay, Robert Langer, and Klavs F Jensen. In vitro and ex vivo strategies for intracellular delivery. *Nature*, 538(7624):183–192, 2016.

[13] Christopher E Brennen. *Cavitation and bubble dynamics*. Cambridge University Press, 2014.

[14] Mingxi Wan, Yi Feng, and Gail ter Haar. Cavitation in biomedicine. *Principles and Techniques*, 23:1–503, 2015.

[15] Yaxin Hu, Jennifer MF Wan, and CH Alfred. Membrane perforation and recovery dynamics in microbubble-mediated sonoporation. *Ultrasound in medicine & biology*, 39(12):2393–2405, 2013.

[16] Ine Lentacker, Ine De Cock, R Deckers, SC De Smedt, and CTW Moonen. Understanding ultrasound induced sonoporation: definitions and underlying mechanisms. *Advanced drug delivery reviews*, 72:49–64, 2014.

[17] Lynda JM Juffermans, Annemieke van Dijk, Cees AM Jongenelen, Benjamin Drukarch, Arie Reijerkerk, Helga E de Vries, Otto Kamp, and René JP Musters. Ultrasound and microbubble-induced intra- and intercellular bioeffects in primary endothelial cells. *Ultrasound in medicine & biology*, 35(11):1917–1927, 2009.

[18] Giovanna Peruzzi, Giorgia Sinibaldi, Giulia Silvani, Giancarlo Ruocco, and Carlo Massimo Casciola. Perspectives on cavitation enhanced endothelial layer permeability. *Colloids and Surfaces B: Biointerfaces*, 168:83–93, 2018.

[19] Kayla Duval, Hannah Grover, Li-Hsin Han, Yongchao Mou, Adrian F Pegoraro, Jeffery Fredberg, and Zi Chen. Modeling physiological events in 2d vs. 3d cell culture. *Physiology*, 32(4):266–277, 2017.

[20] Peter F Davies, Jos A Spaan, and Robert Krams. Shear stress biology of the endothelium. *Annals of biomedical engineering*, 33(12):1714–1718, 2005.

[21] Rumiana Dimova. Giant vesicles: a biomimetic tool for membrane characterization. In *Advances in planar lipid bilayers and liposomes*, volume 16, pages 1–50. Elsevier, 2012.

[22] Rumiana Dimova. Giant vesicles and their use in assays for assessing membrane phase state, curvature, mechanics, and electrical properties. *Annual review of biophysics*, 48:93–119, 2019.

[23] George M Whitesides. The origins and the future of microfluidics. *nature*, 442(7101):368–373, 2006.

[24] Matthias Mehling and Savaş Tay. Microfluidic cell culture. *Current opinion in Biotechnology*, 25:95–102, 2014.

[25] Kristina Haase and Roger D Kamm. Advances in on-chip vascularization. *Regenerative medicine*, 12(3):285–302, 2017.

[26] Ho Cheung Shum, Daeyeon Lee, Insun Yoon, Tom Kodger, and David A Weitz. Double emulsion templated monodisperse phospholipid vesicles. *Langmuir*, 24(15):7651–7653, 2008.

[27] K Karamdad, RV Law, JM Seddon, NJ Brooks, and O Ces. Preparation and mechanical characterisation of giant unilamellar vesicles by a microfluidic method. *Lab on a Chip*, 15(2):557–562, 2015.

[28] Giulia Silvani, Chiara Scognamiglio, Davide Caprini, Luca Marino, Mauro Chinappi, Giorgia Sinibaldi, Giovanna Peruzzi, Mohammad F Kiani, and Carlo M Casciola. Reversible cavitation-induced junctional opening in an artificial endothelial layer. *Small*, 15(51):1905375, 2019.

[29] Giulia Grisanti, Davide Caprini, Giorgia Sinibaldi, Chiara Scognamiglio, Giulia Silvani, Giovanna Peruzzi, and Carlo Massimo Casciola. A microfluidic platform for cavitation-enhanced drug delivery. *Micromachines*, 12(6):658, 2021.

[30] István A Krizbai, Csilla Fazakas, János Haskó, Judit Molnár, Ádám Nyúl-Tóth, Attila E Farkas, and Imola Wilhelm. Molecular structure and function of biological barriers. *Acta Biologica Szegediensis*, 59(suppl. 1.):39–50, 2015.

[31] Gerald Karp. *Cell and molecular biology: concepts and experiments*. John Wiley & Sons, 2009.

[32] James Hillier and Joseph F Hoffman. On the ultrastructure of the plasma membrane as determined by the electron microscope. *Journal of cellular and comparative physiology*, 42(2):203–247, 1953.

[33] PL Yeagle. Cholesterol and related sterols: Roles in membrane structure and function. *The Membranes of Cells, 3rd ed.; Yeagle, PL, Ed*, pages 189–218, 2016.

[34] S Jonathan Singer and Garth L Nicolson. The fluid mosaic model of the structure of cell membranes. *Science*, 175(4023):720–731, 1972.

[35] Evert Gorter and FJEM Grendel. On bimolecular layers of lipoids on the chromocytes of the blood. *The Journal of experimental medicine*, 41(4):439, 1925.

[36] William L Duax, Jane F Griffin, Douglas C Rohrer, and Charles M Weeks. Conformational analysis of sterols: comparison of x-ray crystallographic observations with data from other sources. *Lipids*, 15(9):783–792, 1980.

[37] NP Franks. Structural analysis of hydrated egg lecithin and cholesterol bilayers i. x-ray diffraction. *Journal of molecular biology*, 100(3):345–358, 1976.

[38] DL Worcester and NP Franks. Structural analysis of hydrated egg lecithin and cholesterol bilayers ii. neutron diffraction. *Journal of molecular biology*, 100(3):359–378, 1976.

[39] James Frederic Danielli and Hugh Davson. A contribution to the theory of permeability of thin films. *Journal of cellular and comparative physiology*, 5(4):495–508, 1935.

[40] Garth L Nicolson and SJ Singer. Ferritin-conjugated plant agglutinins as specific saccharide stains for electron microscopy: application to saccharides bound to cell membranes. *Proceedings of the National Academy of Sciences*, 68(5):942–945, 1971.

[41] Hiroshi Hirano, Brenda Parkhouse, Garth L Nicolson, Edwin S Lennox, and SJ Singer. Distribution of saccharide residues on membrane fragments from a myeloma-cell homogenate: its implications for membrane biogenesis. *Proceedings of the National Academy of Sciences*, 69(10):2945–2949, 1972.

[42] Nicholas K Gonatas and Stratis Avrameas. Detection of plasma membrane carbohydrates with lectin peroxidase conjugates. *The Journal of cell biology*, 59(2):436–443, 1973.

[43] Walther Stoeckenius and Donald M Engelman. Current models for the structure of biological membranes. *The Journal of cell biology*, 42(3):613–646, 1969.

[44] Mark S Bretscher. Membrane structure: some general principles. *Science*, 181(4100):622–629, 1973.

[45] Marjorie L Wier and Michael Edidin. Effects of cell density and extracellular matrix on the lateral diffusion of major histocompatibility antigens in cultured fibroblasts. *The Journal of cell biology*, 103(1):215–222, 1986.

[46] David E Golan and William Veatch. Lateral mobility of band 3 in the human erythrocyte membrane studied by fluorescence photobleaching recovery: evidence for control by cytoskeletal interactions. *Proceedings of the National Academy of Sciences*, 77(5):2537–2541, 1980.

[47] Dennis Chapman. Phase transitions and fluidity characteristics of lipids and cell membranes. *Quarterly reviews of biophysics*, 8(2):185–235, 1975.

[48] J Hjort Ipsen, G Karlström, OG Mourtisen, H Wennerström, and MJ Zuckermann. Phase equilibria in the phosphatidylcholine-cholesterol system. *Biochimica et Biophysica Acta (BBA)-Biomembranes*, 905(1):162–172, 1987.

[49] Julita Kulbacka, Anna Choromańska, Joanna Rossowska, Joanna Weżgowiec, Jolanta Saczko, and Marie-Pierre Rols. Cell membrane transport mechanisms: Ion channels and electrical properties of cell membranes. *Transport across natural and modified biological membranes and its implications in physiology and therapy*, pages 39–58, 2017.

[50] Robert B Dean. Theories of electrolyte equilibrium in muscle. In *Biol. Symp*, volume 3, pages 331–348, 1941.

[51] J Chr SKou. Enzymatic basis for active transport of na+ and k+ across cell membrane. *Physiological reviews*, 45(3):596–618, 1965.

[52] W Stillwell. Membrane transport—chapter 19. *An Introduction to Biological Membranes (Second Edition) Composition, Structure and Function. Academic Press, London, UK*, pages 423–451, 2016.

[53] C De Duve. Ciba found. symp. lysosomes. *A. VS. de Reuck e MP Cameron ed., J. e A. Churchill Lid, Londra*, 1963.

[54] Thomas F Roth and Keith R Porter. Yolk protein uptake in the oocyte of the mosquito aedes aegypti. l. *Journal of Cell Biology*, 20(2):313–332, 1964.

[55] Gary J Doherty and Harvey T McMahon. Mechanisms of endocytosis. *Annual review of biochemistry*, 78:857–902, 2009.

[56] Wolfgang Helfrich. Elastic properties of lipid bilayers: theory and possible experiments. *Zeitschrift für Naturforschung C*, 28(11-12):693–703, 1973.

[57] Silke Lorenzen, Rolf-M Servuss, and Wolfgang Helfrich. Elastic torques about membrane edges: a study of pierced egg lecithin vesicles. *Biophysical journal*, 50(4):565–572, 1986.

[58] Tao Zhang, Rastko Sknepnek, Mark John Bowick, and Jennifer M Schwarz. On the modeling of endocytosis in yeast. *Biophysical journal*, 108(3):508–519, 2015.

[59] Hélène Bouvrais, Martin Holmstrup, Peter Westh, and John H Ipsen. Analysis of the shape fluctuations of reconstituted membranes using guvs made from lipid extracts of invertebrates. *Biology open*, 2(4):373–378, 2013.

[60] Amy C Rowat, Per Lyngs Hansen, and John Hjort Ipsen. Experimental evidence of the electrostatic contribution to membrane bending rigidity. *EPL (Europhysics Letters)*, 67(1):144, 2004.

[61] L Fernandez-Puente, I Bivas, MD Mitov, and P Méléard. Temperature and chain length effects on bending elasticity of phosphatidylcholine bilayers. *EPL (Europhysics Letters)*, 28(3):181, 1994.

[62] W Rawicz, K Cc Olbrich, T McIntosh, D Needham, and E Evans. Effect of chain length and unsaturation on elasticity of lipid bilayers. *Biophysical journal*, 79(1):328–339, 2000.

[63] Philippe Meleard, Claire Gerbeaud, Tanja Pott, Laurent Fernandez-Puente, Isak Bivas, Marin D Mitov, Jean Dufourcq, and Pierre Bothorel. Bending elasticities of model membranes: influences of temperature and sterol content. *Biophysical journal*, 72(6):2616–2629, 1997.

[64] Jonas Henriksen, Amy C Rowat, and John H Ipsen. Vesicle fluctuation analysis of the effects of sterols on membrane bending rigidity. *European Biophysics Journal*, 33(8):732–741, 2004.

[65] Hélène Bouvrais, Philippe Méléard, Tanja Pott, Knud J Jensen, Jesper Brask, and John H Ipsen. Softening of popc membranes by magainin. *Biophysical chemistry*, 137(1):7–12, 2008.

[66] Héléne Bouvrais, Philippe Méléard, Tanja Pott, and John Hjort Ipsen. Effects of sodium halide solutions of high concentrations on bending elasticity of popc guvs. *Biophysical journal*, 96(3):161a, 2009.

[67] Hélène Bouvrais, Lars Duelund, and John H Ipsen. Buffers affect the bending rigidity of model lipid membranes. *Langmuir*, 30(1):13–16, 2014.

[68] Sophie Pautot, Barbara J Frisken, and DA Weitz. Engineering asymmetric vesicles. *Proceedings of the National Academy of Sciences*, 100(19):10718–10721, 2003.

[69] Ariane Peyret, Hang Zhao, and Sébastien Lecommandoux. Preparation and properties of asymmetric synthetic membranes based on lipid and polymer self-assembly. *Langmuir*, 34(11):3376–3385, 2018.

[70] Yuting Huang, Shin-Hyun Kim, and Laura R Arriaga. Emulsion templated vesicles with symmetric or asymmetric membranes. *Advances in colloid and interface science*, 247:413–425, 2017.

[71] Adrienne A Brian and Harden M McConnell. Allogeneic stimulation of cytotoxic t cells by supported planar membranes. *Proceedings of the National Academy of Sciences*, 81(19):6159–6163, 1984.

[72] Tania H Watts, Adrienne A Brian, John W Kappler, Philippa Marrack, and Harden M McConnell. Antigen presentation by supported planar membranes containing affinity-purified i-ad. *Proceedings of the National Academy of Sciences*, 81(23):7564–7568, 1984.

[73] Michael L Wagner and Lukas K Tamm. Tethered polymer-supported planar lipid bilayers for reconstitution of integral membrane proteins: silane-polyethyleneglycol-lipid as a cushion and covalent linker. *Biophysical journal*, 79(3):1400–1414, 2000.

[74] Harden M McConnell, Tania H Watts, RM Weis, and Adrienne A Brian. Supported planar membranes in studies of cell-cell recognition in the immune system. *Biochimica et Biophysica Acta (BBA)-Reviews on Biomembranes*, 864(1):95–106, 1986.

[75] Erich Sackmann. Supported membranes: scientific and practical applications. *Science*, 271(5245):43–48, 1996.

[76] Ralf P Richter, Rémi Bérat, and Alain R Brisson. Formation of solid-supported lipid bilayers: an integrated view. *Langmuir*, 22(8):3497–3505, 2006.

[77] M Egger, SP Heyn, and HE Gaub. Two-dimensional recognition pattern of lipid-anchored fab'fragments. *Biophysical journal*, 57(3):669–673, 1990.

[78] Michael L Wagner and Lukas K Tamm. Reconstituted syntaxin1a/snap25 interacts with negatively charged lipids as measured by lateral diffusion in planar supported bilayers. *Biophysical journal*, 81(1):266–275, 2001.

[79] Edwin Kalb, Sammy Frey, and Lukas K Tamm. Formation of supported planar bilayers by fusion of vesicles to supported phospholipid

monolayers. *Biochimica et Biophysica Acta (BBA)-Biomembranes*, 1103(2):307–316, 1992.

[80] Christian Hennesthal and Claudia Steinem. Pore-spanning lipid bilayers visualized by scanning force microscopy. *Journal of the American Chemical Society*, 122(33):8085–8086, 2000.

[81] Christian Hennesthal, Janine Drexler, and Claudia Steinem. Membrane-suspended nanocompartments based on ordered pores in alumina. *ChemPhysChem*, 3(10):885–889, 2002.

[82] Ingo Mey, Milena Stephan, Eva K Schmitt, Martin Michael Müller, Martine Ben Amar, Claudia Steinem, and Andreas Janshoff. Local membrane mechanics of pore-spanning bilayers. *Journal of the American Chemical Society*, 131(20):7031–7039, 2009.

[83] Danilo D Lasic. The mechanism of vesicle formation. *Biochemical Journal*, 256(1):1–11, 1988.

[84] Aldo Jesorka and Owe Orwar. Liposomes: technologies and analytical applications. *Annu. Rev. Anal. Chem.*, 1:801–832, 2008.

[85] Pier Luigi Luisi and Peter Walde. *Giant vesicles*, volume 22. John Wiley & Sons, 2008.

[86] TJ Murphy and AE Shamoo. Reconstitution of ca-2+-mg-2+-atpase in giant vesicles. In *BIOPHYSICAL JOURNAL*, volume 21, pages A27–A27. BIOPHYSICAL SOCIETY 9650 ROCKVILLE PIKE, BETHESDA, MD 20814-3998, 1978.

[87] Alberto A Gabizon. Liposomal drug carrier systems in cancer chemotherapy: current status and future prospects. *Journal of drug targeting*, 10(7):535–538, 2002.

[88] Rumiana Dimova and Carlos Marques. *The Giant Vesicle Book*. CRC Press, 2019.

[89] Shia-Yen Teh, Ruba Khnouf, Hugh Fan, and Abraham P Lee. Stable, biocompatible lipid vesicle generation by solvent extraction-based droplet microfluidics. *Biomicrofluidics*, 5(4):044113, 2011.

[90] Roger Wick, Miglena I Angelova, Peter Walde, and Pier Luigi Luisi. Microinjection into giant vesicles and light microscopy investigation of enzyme-mediated vesicle transformations. *Chemistry & biology*, 3(2):105–111, 1996.

[91] NI Hristova, MI Angelova, and I Tsoneva. An experimental approach for direct observation of the interaction of polyanions with sphingosine-containing giant vesicles. *Bioelectrochemistry*, 58(1):65–73, 2002.

[92] Doris M Haverstick and Michael Glaser. Visualization of ca2+-induced phospholipid domains. *Proceedings of the National Academy of Sciences*, 84(13):4475–4479, 1987.

[93] Nicolas Rodriguez, Frédéric Pincet, and Sophie Cribier. Giant vesicles formed by gentle hydration and electroformation: a comparison by fluorescence microscopy. *Colloids and Surfaces B: Biointerfaces*, 42(2):125–130, 2005.

[94] Sarah L Veatch and Sarah L Keller. Organization in lipid membranes containing cholesterol. *Physical review letters*, 89(26):268101, 2002.

[95] MJ Sarmento, M Prieto, and Fábio Fernandes. Reorganization of lipid domain distribution in giant unilamellar vesicles upon immobilization with different membrane tethers. *Biochimica et Biophysica Acta (BBA)-Biomembranes*, 1818(11):2605–2615, 2012.

[96] Jonas Korlach, Petra Schwille, Watt W Webb, and Gerald W Feigenson. Characterization of lipid bilayer phases by confocal microscopy and fluorescence correlation spectroscopy. *Proceedings of the National Academy of Sciences*, 96(15):8461–8466, 1999.

[97] J Korlach, C Reichle, T Müller, T Schnelle, and WW Webb. Trapping, deformation, and rotation of giant unilamellar vesicles in octode dielectrophoretic field cages. *Biophysical journal*, 89(1):554–562, 2005.

[98] Tatyana M Konyakhina and Gerald W Feigenson. Phase diagram of a polyunsaturated lipid mixture: brain sphingomyelin/1-stearoyl-2-docosahexaenoyl-sn-glycero-3-phosphocholine/cholesterol. *Biochimica et Biophysica Acta (BBA)-Biomembranes*, 1858(1):153–161, 2016.

[99] Rafael B Lira, Jan Steinkühler, Roland L Knorr, Rumiana Dimova, and Karin A Riske. Posing for a picture: vesicle immobilization in agarose gel. *Scientific reports*, 6(1):1–12, 2016.

[100] Kévin Carvalho, Laurence Ramos, Christian Roy, and Catherine Picart. Giant unilamellar vesicles containing phosphatidylinositol (4, 5) bisphosphate: characterization and functionality. *Biophysical journal*, 95(9):4348–4360, 2008.

[101] LA Bagatolli and E Gratton. Two-photon fluorescence microscopy observation of shape changes at the phase transition in phospholipid giant unilamellar vesicles. *Biophysical Journal*, 77(4):2090–2101, 1999.

[102] Nicoletta Kahya and Petra Schwille. How phospholipid-cholesterol interactions modulate lipid lateral diffusion, as revealed by fluorescence correlation spectroscopy. *Journal of fluorescence*, 16(5):671–678, 2006.

[103] Thomas Litschel and Petra Schwille. Protein reconstitution inside giant unilamellar vesicles. *Annual Review of Biophysics*, 50:525–548, 2021.

[104] Jorge Daniel Cortese, Bill Schwab, Carl Frieden, and Elliot L Elson. Actin polymerization induces a shape change in actin-containing vesicles. *Proceedings of the National Academy of Sciences*, 86(15):5773–5777, 1989.

[105] Hidetake Miyata and Hirokazu Hotani. Morphological changes in liposomes caused by polymerization of encapsulated actin and spontaneous formation of actin bundles. *Proceedings of the National Academy of Sciences*, 89(23):11547–11551, 1992.

[106] Dennis Merkle, Nicoletta Kahya, and Petra Schwille. Reconstitution and anchoring of cytoskeleton inside giant unilamellar vesicles. *ChemBioChem*, 9(16):2673–2681, 2008.

[107] Philippe Girard, Jacques Pécréaux, Guillaume Lenoir, Pierre Falson, Jean-Louis Rigaud, and Patricia Bassereau. A new method for the reconstitution of membrane proteins into giant unilamellar vesicles. *Biophysical journal*, 87(1):419–429, 2004.

[108] Miho Yanagisawa, Masayuki Iwamoto, Ayako Kato, Kenichi Yoshikawa, and Shigetoshi Oiki. Oriented reconstitution of a membrane protein in a giant unilamellar vesicle: experimental verification with the potassium channel kcsa. *Journal of the American Chemical Society*, 133(30):11774–11779, 2011.

[109] Kirsten Bacia, Eugene Futai, Simone Prinz, Annette Meister, Sebastian Daum, Daniela Glatte, John AG Briggs, and Randy Schekman. Multibudded tubules formed by copii on artificial liposomes. *Scientific reports*, 1(1):1–6, 2011.

[110] Marcus R Helfrich, Lauren K Mangeney-Slavin, M Scott Long, Karrera Y Djoko, and Christine D Keating. Aqueous phase separation in giant vesicles. *Journal of the American Chemical Society*, 124(45):13374–13375, 2002.

[111] M Scott Long, Clinton D Jones, Marcus R Helfrich, Lauren K Mangeney-Slavin, and Christine D Keating. Dynamic microcompartmentation in synthetic cells. *Proceedings of the National Academy of Sciences*, 102(17):5920–5925, 2005.

[112] Aline Fischer, Andrea Franco, and Thomas Oberholzer. Giant vesicles as microreactors for enzymatic mrna synthesis. *ChemBioChem*, 3(5):409–417, 2002.

[113] Vincent Noireaux and Albert Libchaber. A vesicle bioreactor as a step toward an artificial cell assembly. *Proceedings of the National Academy of Sciences*, 101(51):17669–17674, 2004.

[114] Yuval Elani, Robert V Law, and Oscar Ces. Vesicle-based artificial cells as chemical microreactors with spatially segregated reaction pathways. *Nature communications*, 5(1):1–5, 2014.

[115] Yuval Elani, Robert V Law, and Oscar Ces. Protein synthesis in artificial cells: using compartmentalisation for spatial organisation in vesicle bioreactors. *Physical Chemistry Chemical Physics*, 17(24):15534–15537, 2015.

[116] Petra Schwille, Joachim Spatz, Katharina Landfester, Eberhard Bodenschatz, Stephan Herminghaus, Victor Sourjik, Tobias J Erb, Philippe

Bastiaens, Reinhard Lipowsky, Anthony Hyman, et al. Maxsynbio: avenues towards creating cells from the bottom up. *Angewandte Chemie International Edition*, 57(41):13382–13392, 2018.

[117] Rumiana Dimova, Said Aranda, Natalya Bezlyepkina, Vesselin Nikolov, Karin A Riske, and Reinhard Lipowsky. A practical guide to giant vesicles. probing the membrane nanoregime via optical microscopy. *Journal of Physics: Condensed Matter*, 18(28):S1151, 2006.

[118] Rumiana Dimova. Recent developments in the field of bending rigidity measurements on membranes. *Advances in colloid and interface science*, 208:225–234, 2014.

[119] Evan A Evans. Bending elastic modulus of red blood cell membrane derived from buckling instability in micropipet aspiration tests. *Biophysical journal*, 43(1):27–30, 1983.

[120] Evan Evans and David Needham. Physical properties of surfactant bilayer membranes: thermal transitions, elasticity, rigidity, cohesion and colloidal interactions. *Journal of Physical Chemistry*, 91(16):4219–4228, 1987.

[121] F Brochard and JF Lennon. Frequency spectrum of the flicker phenomenon in erythrocytes. *Journal de Physique*, 36(11):1035–1047, 1975.

[122] RM Servuss, V Harbich, and W Helfrich. Measurement of the curvature-elastic modulus of egg lecithin bilayers. *Biochimica et biophysica acta (BBA)-biomembranes*, 436(4):900–903, 1976.

[123] MB Schneider, JT Jenkins, and WW Webb. Thermal fluctuations of large quasi-spherical bimolecular phospholipid vesicles. *Journal de Physique*, 45(9):1457–1472, 1984.

[124] Philippe Méléard and Tanja Pott. Overview of a quest for bending elasticity measurement. In *Advances in planar lipid bilayers and liposomes*, volume 17, pages 55–75. Elsevier, 2013.

[125] Kenneth S Saladin. Anatomy & physiology: the unity of form and function. 2004.

[126] CC Michel and FE Curry. Microvascular permeability. *Physiological reviews*, 1999.

[127] Yulia A Komarova, Kevin Kruse, Dolly Mehta, and Asrar B Malik. Protein interactions at endothelial junctions and signaling mechanisms regulating endothelial permeability. *Circulation research*, 120(1):179–206, 2017.

[128] Maria Grazia Lampugnani, Monica Corada, Luis Caveda, Ferruccio Breviario, Oran Ayalon, Benjamin Geiger, and Elisabetta Dejana. The molecular organization of endothelial cell to cell junctions: differential association of plakoglobin, beta-catenin, and alpha-catenin with vascular endothelial cadherin (ve-cadherin). *Journal of Cell Biology*, 129(1):203–217, 1995.

[129] Shintaro Suzuki, Kenji Sano, and Hidenobu Tanihara. Diversity of the cadherin family: evidence for eight new cadherins in nervous tissue. *Cell regulation*, 2(4):261–270, 1991.

[130] Kazumasa Morita, Mikio Furuse, Kazushi Fujimoto, and Shoichiro Tsukita. Claudin multigene family encoding four-transmembrane domain protein components of tight junction strands. *Proceedings of the National Academy of Sciences*, 96(2):511–516, 1999.

[131] Mikio Furuse, Kazushi Fujimoto, Naruki Sato, Tetsuaki Hirase, Sachiko Tsukita, and Shoichiro Tsukita. Overexpression of occludin, a tight junction-associated integral membrane protein, induces the formation of intracellular multilamellar bodies bearing tight junction-like structures. *Journal of cell science*, 109(2):429–435, 1996.

[132] Inés Martìn-Padura, Susan Lostaglio, Markus Schneemann, Lisa Williams, Maria Romano, Paolo Fruscella, Carla Panzeri, Antonella Stoppacciaro, Luigi Ruco, Antonello Villa, et al. Junctional adhesion molecule, a novel member of the immunoglobulin superfamily that distributes at intercellular junctions and modulates monocyte transmigration. *Journal of Cell Biology*, 142(1):117–127, 1998.

[133] Xin Cong and Wei Kong. Endothelial tight junctions and their regulatory signaling pathways in vascular homeostasis and disease. *Cellular signalling*, 66:109485, 2020.

[134] Elisabetta Dejana, Fabrizio Orsenigo, Cinzia Molendini, Peter Baluk, and Donald M McDonald. Organization and signaling of endothelial cell-to-cell junctions in various regions of the blood and lymphatic vascular trees. *Cell and tissue research*, 335(1):17–25, 2009.

[135] J David Robertson. The occurrence of a subunit pattern in the unit membranes of club endings in mauthner cell synapses in goldfish brains. *The Journal of cell biology*, 19(1):201–221, 1963.

[136] Daniel A Goodenough. Bulk isolation of mouse hepatocyte gap junctions: Characterization of the principal protein, connexin. *The Journal of cell biology*, 61(2):557–563, 1974.

[137] HAZEL Lum and ASRAR B Malik. Regulation of vascular endothelial barrier function. *American Journal of Physiology-Lung Cellular and Molecular Physiology*, 267(3):L223–L241, 1994.

[138] John R Pappenheimer, EM Renkin, and LM Borrero. Filtration, diffusion and molecular sieving through peripheral capillary membranes: a contribution to the pore theory of capillary permeability. *American Journal of Physiology-Legacy Content*, 167(1):13–46, 1951.

[139] Yulia Komarova and Asrar B Malik. Regulation of endothelial permeability via paracellular and transcellular transport pathways. *Annual review of physiology*, 72:463–493, 2010.

[140] Nicolae Ghinea, Anton Fixman, Dorin Alexandru, Doina Popov, Mirela Hasu, Lucian Ghitescu, Monica Eskenasy, Maya Simionescu, and Nicolae Simionescu. Identification of albumin-binding proteins in capillary endothelial cells. *The Journal of cell biology*, 107(1):231–239, 1988.

[141] N Ghinea, Monica Eskenasy, Maya Simionescu, and Nicolae Simionescu. Endothelial albumin binding proteins are membrane-associated components exposed on the cell surface. *Journal of Biological Chemistry*, 264(9):4755–4758, 1989.

[142] George L King and Sandra M Johnson. Receptor-mediated transport of insulin across endothelial cells. *Science*, 227(4694):1583–1586, 1985.

[143] Jan E Schnitzer, Phil Oh, Emmett Pinney, and Jenny Allard. Filipin-sensitive caveolae-mediated transport in endothelium: reduced transcytosis, scavenger endocytosis, and capillary permeability of select macromolecules. *Journal of Cell Biology*, 127(5):1217–1232, 1994.

[144] Wilfred A Jefferies, Malcolm R Brandon, Simon V Hunt, Alan F Williams, Kevin C Gatter, and David Y Mason. Transferrin receptor on endothelium of brain capillaries. *Nature*, 312(5990):162–163, 1984.

[145] Lucian Ghitescu, Anton Fixman, Maya Simionescu, and Nicolae Simionescu. Specific binding sites for albumin restricted to plasmalemmal vesicles of continuous capillary endothelium: receptor-mediated transcytosis. *The Journal of cell biology*, 102(4):1304–1311, 1986.

[146] F Breviario, L Caveda, M Corada, I Martin-Padura, P Navarro, J Golay, M Introna, D Gulino, MG Lampugnani, and E Dejana. Functional properties of human vascular endothelial cadherin (7b4/cadherin-5), an endothelium-specific cadherin. *Arteriosclerosis, thrombosis, and vascular biology*, 15(8):1229–1239, 1995.

[147] Eleni Tzima, Mohamed Irani-Tehrani, William B Kiosses, Elizabetta Dejana, David A Schultz, Britta Engelhardt, Gaoyuan Cao, Horace DeLisser, and Martin Alexander Schwartz. A mechanosensory complex that mediates the endothelial cell response to fluid shear stress. *Nature*, 437(7057):426–431, 2005.

[148] Brian G Coon, Nicolas Baeyens, Jinah Han, Madhusudhan Budatha, Tyler D Ross, Jennifer S Fang, Sanguk Yun, Jeon-Leon Thomas, and Martin A Schwartz. Intramembrane binding of ve-cadherin to vegfr2 and vegfr3 assembles the endothelial mechanosensory complex. *Journal of Cell Biology*, 208(7):975–986, 2015.

[149] Daniel E Conway, Mark T Breckenridge, Elizabeth Hinde, Enrico Gratton, Christopher S Chen, and Martin A Schwartz. Fluid shear stress on endothelial cells modulates mechanical tension across ve-cadherin and pecam-1. *Current Biology*, 23(11):1024–1030, 2013.

[150] Fabrizio Orsenigo, Costanza Giampietro, Aldo Ferrari, Monica Corada, Ariane Galaup, Sara Sigismund, Giuseppe Ristagno, Luigi Maddaluno,

Gou Young Koh, Davide Franco, et al. Phosphorylation of ve-cadherin is modulated by haemodynamic forces and contributes to the regulation of vascular permeability in vivo. *Nature communications*, 3(1):1–15, 2012.

[151] Zhijun Liu, John L Tan, Daniel M Cohen, Michael T Yang, Nathan J Sniadecki, Sami Alom Ruiz, Celeste M Nelson, and Christopher S Chen. Mechanical tugging force regulates the size of cell–cell junctions. *Proceedings of the National Academy of Sciences*, 107(22):9944–9949, 2010.

[152] Jochen Seebach, Abdallah Abu Taha, Janine Lenk, Nico Lindemann, Xiaoyi Jiang, Klaus Brinkmann, Sven Bogdan, and Hans-Joachim Schnittler. The cellbordertracker, a novel tool to quantitatively analyze spatiotemporal endothelial junction dynamics at the subcellular level. *Histochemistry and cell biology*, 144(6):517–532, 2015.

[153] Abdallah Abu Taha, Muna Taha, Jochen Seebach, and Hans-J Schnittler. Arp2/3-mediated junction-associated lamellipodia control ve-cadherin–based cell junction dynamics and maintain monolayer integrity. *Molecular biology of the cell*, 25(2):245–256, 2014.

[154] Jochen Seebach, Gerald Donnert, Romy Kronstein, Sebastian Werth, Beata Wojciak-Stothard, Darryl Falzarano, Christof Mrowietz, Stefan W Hell, and Hans-J Schnittler. Regulation of endothelial barrier function during flow-induced conversion to an arterial phenotype. *Cardiovascular research*, 75(3):598–607, 2007.

[155] Sudong Kim, Hyunjae Lee, Minhwan Chung, and Noo Li Jeon. Engineering of functional, perfusable 3d microvascular networks on a chip. *Lab on a Chip*, 13(8):1489–1500, 2013.

[156] TS Reese and Morris J Karnovsky. Fine structural localization of a blood-brain barrier to exogenous peroxidase. *Journal of Cell Biology*, 34(1):207–217, 1967.

[157] MW Brightman and TS2107650 Reese. Junctions between intimately apposed cell membranes in the vertebrate brain. *The Journal of cell biology*, 40(3):648–677, 1969.

[158] Hartwig Wolburg and Andrea Lippoldt. Tight junctions of the blood–brain barrier: development, composition and regulation. *Vascular pharmacology*, 38(6):323–337, 2002.

[159] Roberta Paolinelli, Monica Corada, Fabrizio Orsenigo, and Elisabetta Dejana. The molecular basis of the blood brain barrier differentiation and maintenance. is it still a mystery? *Pharmacological research*, 63(3):165–171, 2011.

[160] N Joan Abbott, Lars Rönnbäck, and Elisabeth Hansson. Astrocyte–endothelial interactions at the blood–brain barrier. *Nature reviews neuroscience*, 7(1):41–53, 2006.

[161] Harold K Kimelberg, Thomas F Tracy, Sandra M Biddlecome, and Robert S Bourke. The effect of entrapment in liposomes on the in vivo distribution of [3h] methotrexate in a primate. *Cancer research*, 36(8):2949–2957, 1976.

[162] George Poste and Demetrios Papahadjopoulos. Lipid vesicles as carriers for introducing materials into cultured cells: influence of vesicle lipid composition on mechanism (s) of vesicle incorporation into cells. *Proceedings of the National Academy of Sciences*, 73(5):1603–1607, 1976.

[163] Rudy L Juliano and Dennis Stamp. Pharmacokinetics of liposome-encapsulated anti-tumor drugs: studies with vinblastine, actinomycin d, cytosine arabinoside, and daunomycin. *Biochemical pharmacology*, 27(1):21–27, 1978.

[164] Suresh K Alahari, Robert DeLong, Michael H Fisher, Nicholas M Dean, Pierre Viliet, and RL Juliano. Novel chemically modified oligonucleotides provide potent inhibition of p-glycoprotein expression. *Journal of Pharmacology and Experimental Therapeutics*, 286(1):419–428, 1998.

[165] PR Cullis. Lateral diffusion rates of phosphatidylcholine in vesicle membranes: Eeffects of cholesterol and hydrocarbon phase transitions. *FEBS letters*, 70(1-2):223–228, 1976.

[166] PR Cullis and MJ Hope. The bilayer stabilizing role of sphingomyelin in the presence of cholesterol. a 31p nmr study. *Biochimica et Biophysica Acta (BBA)-Biomembranes*, 597(3):533–542, 1980.

[167] G Storm, FH Roerdink, PA Steerenberg, WH De Jong, and DJA Crommelin. Influence of lipid composition on the antitumor activity exerted by doxorubicin-containing liposomes in a rat solid tumor model. *Cancer research*, 47(13):3366–3372, 1987.

[168] Bohdana M Discher, You-Yeon Won, David S Ege, James CM Lee, Frank S Bates, Dennis E Discher, and Daniel A Hammer. Polymersomes: tough vesicles made from diblock copolymers. *Science*, 284(5417):1143–1146, 1999.

[169] Timothy D Heath, Robert T Fraley, and Demetrios Papahdjopoulos. Antibody targeting of liposomes: cell specificity obtained by conjugation of f (ab') 2 to vesicle surface. *Science*, 210(4469):539–541, 1980.

[170] Robert J Lee and Philip S Low. Delivery of liposomes into cultured kb cells via folate receptor-mediated endocytosis. *Journal of Biological Chemistry*, 269(5):3198–3204, 1994.

[171] Alexander L Klibanov, Kazuo Maruyama, Vladimir P Torchilin, and Leaf Huang. Amphipathic polyethyleneglycols effectively prolong the circulation time of liposomes. *FEBS letters*, 268(1):235–237, 1990.

[172] TM Allen, C Hansen, F Martin, C Redemann, and A Yau-Young. Liposomes containing synthetic lipid derivatives of poly (ethylene glycol) show prolonged circulation half-lives in vivo. *Biochimica et Biophysica Acta (BBA)-Biomembranes*, 1066(1):29–36, 1991.

[173] Amarnath Sharma and Uma S Sharma. Liposomes in drug delivery: progress and limitations. *International journal of pharmaceutics*, 154(2):123–140, 1997.

[174] Sinil Kim and George M Martin. Preparation of cell-size unilamellar liposomes with high captured volume and defined size distribution. *Biochimica et Biophysica Acta (BBA)-Biomembranes*, 646(1):1–9, 1981.

[175] Tomer Noyhouzer, Chloé L'Homme, Isabelle Beaulieu, Stephanie Mazurkiewicz, Sabine Kuss, Heinz-Bernhard Kraatz, Sylvain Canesi, and Janine Mauzeroll. Ferrocene-modified phospholipid: an innovative precursor for redox-triggered drug delivery vesicles selective to cancer cells. *Langmuir*, 32(17):4169–4178, 2016.

[176] Yogita P Patil, Mrunmayi D Kumbhalkar, and Sameer Jadhav. Extrusion of electroformed giant unilamellar vesicles through track-etched membranes. *Chemistry and physics of lipids*, 165(4):475–481, 2012.

[177] Rakesh K Jain. Transport of molecules across tumor vasculature. *Cancer and Metastasis Reviews*, 6(4):559–593, 1987.

[178] Alberto A Gabizon. Selective tumor localization and improved therapeutic index of anthracyclines encapsulated in long-circulating liposomes. *Cancer research*, 52(4):891–896, 1992.

[179] MB Yatvin, W Kreutz, BA Horwitz, and M Shinitzky. ph-sensitive liposomes: possible clinical implications. *Science*, 210(4475):1253–1255, 1980.

[180] John N Weinstein, RL Magin, MB Yatvin, and DS Zaharko. Liposomes and local hyperthermia: selective delivery of methotrexate to heated tumors. *Science*, 204(4389):188–191, 1979.

[181] Garheng Kong, Rod D Braun, and Mark W Dewhirst. Hyperthermia enables tumor-specific nanoparticle delivery: effect of particle size. *Cancer research*, 60(16):4440–4445, 2000.

[182] VP Torchilin, MI Papisov, NM Orekhova, AA Belyaev, AD Petrov, and SE Ragimov. Magnetically driven thrombolytic preparation containing immobilized streptokinase-targeted transport and action. *Pathophysiology of Haemostasis and Thrombosis*, 18(2):113–116, 1988.

[183] Ronald W Holz and Ruth A Senter. Plasma membrane and chromaffin granule characteristics in digitonin-treated chromaffin cells. *Journal of neurochemistry*, 45(5):1548–1557, 1985.

[184] Kalwant S Authi, BeverlyJ Evenden, and Neville Crawford. Metabolic and functional consequences of introducing inositol 1, 4, 5-trisphosphate into saponin-permeabilized human platelets. *Biochemical Journal*, 233(3):707–718, 1986.

[185] Steve J Ludtke, Ke He, William T Heller, Thad A Harroun, Lin Yang, and Huey W Huang. Membrane pores induced by magainin. *Biochemistry*, 35(43):13723–13728, 1996.

[186] Katsumi Matsuzaki, Osamu Murase, Nobutaka Fujii, and Koichiro Miyajima. An antimicrobial peptide, magainin 2, induced rapid flip-flop of phospholipids coupled with pore formation and peptide translocation. *Biochemistry*, 35(35):11361–11368, 1996.

[187] Hsiao S Liu, Miguel F Refojo, Henry D Perry, and Daniel M Albert. Direct delivery of anticancer agents: experimental treatment of intraocular malignancy. *Investigative ophthalmology & visual science*, 17(10):993–1004, 1978.

[188] Ted M Klein, Edward D Wolf, Ray Wu, and John C Sanford. High-velocity microprojectiles for delivering nucleic acids into living cells. *Nature*, 327(6117):70–73, 1987.

[189] Tai-Kin Wong and Eberhard Neumann. Electric field mediated gene transfer. *Biochemical and biophysical research communications*, 107(2):584–587, 1982.

[190] Eberhard Neumann, M Schaefer-Ridder, Y Wang, and PhH Hofschneider. Gene transfer into mouse lyoma cells by electroporation in high electric fields. *The EMBO journal*, 1(7):841–845, 1982.

[191] Ryo Shirakashi, Vladimir L Sukhorukov, Randolph Reuss, Alexander Schulz, and Ulrich Zimmermann. Effects of a pulse electric field on electrofusion of giant unilamellar vesicle (guv)-jurkat cell (measurement of fusion ratio and electric field analysis of pulsed guv-jurkat cell). *Journal of Thermal Science and Technology*, 7(4):589–602, 2012.

[192] Akira C Saito, Toshihiko Ogura, Kei Fujiwara, Satoshi Murata, and Shin-ichiro M Nomura. Introducing micrometer-sized artificial objects into live cells: A method for cell–giant unilamellar vesicle electrofusion. *PloS one*, 9(9):e106853, 2014.

[193] Marcus Fechheimer, John F Boylan, Sandra Parker, Jesse E Sisken, Gordhan L Patel, and Stephen G Zimmer. Transfection of mammalian cells with plasmid dna by scrape loading and sonication loading. *Proceedings of the National Academy of Sciences*, 84(23):8463–8467, 1987.

[194] Keyvan Keyhani, Héctor R Guzmán, Aimee Parsons, Thomas N Lewis, and Mark R Prausnitz. Intracellular drug delivery using low-frequency

ultrasound: quantification of molecular uptake and cell viability. *Pharmaceutical research*, 18(11):1514–1520, 2001.

[195] Sophie Mehier-Humbert, Feng Yan, Peter Frinking, Michel Schneider, Richard H Guy, and Thierry Bettinger. Ultrasound-mediated gene delivery: influence of contrast agent on transfection. *Bioconjugate chemistry*, 18(3):652–662, 2007.

[196] Francis A Duck. The propagation of ultrasound through tissue. *The safe use of ultrasound in medical diagnosis*, pages 4–18, 2012.

[197] GT Clement. Perspectives in clinical uses of high-intensity focused ultrasound. *Ultrasonics*, 42(10):1087–1093, 2004.

[198] Tanguy Boissenot, Alexandre Bordat, Elias Fattal, and Nicolas Tsapis. Ultrasound-triggered drug delivery for cancer treatment using drug delivery systems: from theoretical considerations to practical applications. *Journal of Controlled Release*, 241:144–163, 2016.

[199] Francis A Duck and G Ter Haar. *The safe use of ultrasound in medical diagnosis*. 2000.

[200] Douglas L Miller, Nadine B Smith, Michael R Bailey, Gregory J Czarnota, Kullervo Hynynen, Inder Raj S Makin, and Bioeffects Committee of the American Institute of Ultrasound in Medicine. Overview of therapeutic ultrasound applications and safety considerations. *Journal of ultrasound in medicine*, 31(4):623–634, 2012.

[201] Stuart J Warden, Robyn K Fuchs, Chris K Kessler, Keith G Avin, Ryan E Cardinal, and Rena L Stewart. Ultrasound produced by a conventional therapeutic ultrasound unit accelerates fracture repair. *Physical Therapy*, 86(8):1118–1127, 2006.

[202] Dieter Gebauer, Edgar Mayr, Ernst Orthner, and John P Ryaby. Low-intensity pulsed ultrasound: effects on nonunions. *Ultrasound in medicine & biology*, 31(10):1391–1402, 2005.

[203] Emmanuel S Papadopoulos and Raj Mani. The role of ultrasound therapy in the management of musculoskeletal soft tissue pain. *The International Journal of Lower Extremity Wounds*, 19(4):350–358, 2020.

[204] Nancy N Byl. The use of ultrasound as an enhancer for transcutaneous drug delivery: phonophoresis. *Physical therapy*, 75(6):539–553, 1995.

[205] Samir Mitragotri and Joseph Kost. Low-frequency sonophoresis: a review. *Advanced drug delivery reviews*, 56(5):589–601, 2004.

[206] James E Kennedy. High-intensity focused ultrasound in the treatment of solid tumours. *Nature reviews cancer*, 5(4):321–327, 2005.

[207] Charles C Church and Stanley B Barnett. Ultrasound-induced heating and its biological consequences. *The safe use of ultrasound in medical diagnosis*, pages 46–63, 2012.

[208] Farzaneh Ahmadi, Ian V McLoughlin, Sunita Chauhan, and Gail ter-Haar. Bio-effects and safety of low-intensity, low-frequency ultrasonic exposure. *Progress in biophysics and molecular biology*, 108(3):119–138, 2012.

[209] Chang W Song. Effect of local hyperthermia on blood flow and microenvironment: a review. *Cancer research*, 44(10 Supplement):4721s–4730s, 1984.

[210] James R Lepock. Measurement of protein stability and protein denaturation in cells using differential scanning calorimetry. *Methods*, 35(2):117–125, 2005.

[211] Joseph L Roti Roti. Cellular responses to hyperthermia (40–46 c): Cell killing and molecular events. *International Journal of hyperthermia*, 24(1):3–15, 2008.

[212] James R Jago. Exposure criteria for medical diagnostic ultrasound: I. criteria based on thermal mechanisms: Ncrp report no. 113, bethesda, md. 1992, 278 pp, 1995.

[213] Francis A Duck. Medical and non-medical protection standards for ultrasound and infrasound. *Progress in biophysics and molecular biology*, 93(1-3):176–191, 2007.

[214] Mouna El Mekki Azouzi, Claire Ramboz, Jean-François Lenain, and Frédéric Caupin. A coherent picture of water at extreme negative pressure. *Nature Physics*, 9(1):38–41, 2013.

[215] L Rayleigh. On the pressure developed in a liquid during the collapse of a spherical cavity: Philosophical magazine series 6, 34, 94–98, 1917.

[216] Emilio Quaia. Physical basis and principles of action of microbubble-based contrast agents. In *Contrast media in ultrasonography*, pages 15–30. Springer, 2005.

[217] FG BLAKE jr. The onset of cavitation in liquids harvard univ. *Acoust. Res. Lab., Techn. Memor*, 12, 1949.

[218] Milton S Plesset and Richard B Chapman. Collapse of an initially spherical vapour cavity in the neighbourhood of a solid boundary. *Journal of Fluid Mechanics*, 47(2):283–290, 1971.

[219] Francesco Magaletti, Luca Marino, and Carlo Massimo Casciola. Shock wave formation in the collapse of a vapor nanobubble. *Physical Review Letters*, 114(6):064501, 2015.

[220] Alexander A Doinikov, Leila Aired, and Ayache Bouakaz. Acoustic scattering from a contrast agent microbubble near an elastic wall of finite thickness. *Physics in Medicine & Biology*, 56(21):6951, 2011.

[221] James Collis, Richard Manasseh, Petar Liovic, Paul Tho, Andrew Ooi, Karolina Petkovic-Duran, and Yonggang Zhu. Cavitation microstreaming and stress fields created by microbubbles. *Ultrasonics*, 50(2):273–279, 2010.

[222] TG Leighton, AJ Walton, and MJW Pickworth. Primary bjerknes forces. *European Journal of Physics*, 11(1):47, 1990.

[223] Nikolaos A Pelekasis, Alexandra Gaki, Alexander Doinikov, and John A Tsamopoulos. Secondary bjerknes forces between two bubbles and the phenomenon of acoustic streamers. *Journal of Fluid Mechanics*, 500:313–347, 2004.

[224] Christopher W Barney, Carey E Dougan, Kelly R McLeod, Amir Kazemi-Moridani, Yue Zheng, Ziyu Ye, Sacchita Tiwari, Ipek Sacligil, Robert A Riggleman, Shengqiang Cai, et al. Cavitation in soft matter. *Proceedings of the National Academy of Sciences*, 117(17):9157–9165, 2020.

[225] Robert E Apfel and Christy K Holland. Gauging the likelihood of cavitation from short-pulse, low-duty cycle diagnostic ultrasound. *Ultrasound in medicine & biology*, 17(2):179–185, 1991.

[226] AIUM Clinical Standards Committee. How to interpret the ultrasound output display standard for higher acoustic output diagnostic ultrasound devices. *Journal of Ultrasound in Medicine*, 23(5):723–726, 2004.

[227] Klazina Kooiman, Hendrik J Vos, Michel Versluis, and Nico de Jong. Acoustic behavior of microbubbles and implications for drug delivery. *Advanced drug delivery reviews*, 72:28–48, 2014.

[228] Mark W Keller, William Glasheen, and Sanjiv Kaul. Albunex: a safe and effective commercially produced agent for myocardial contrast echocardiography. *Journal of the American Society of Echocardiography*, 2(1):48–52, 1989.

[229] Barbara A Carroll, Richard J Turner, E GLENN Tickner, Douglass B Boyle, and Stuart W Young. Gelatin encapsulated nitrogen microbubbles as ultrasonic contrast agents. *Investigative radiology*, 15(3):260–266, 1980.

[230] Evan C Unger, Thomas P McCreery, Robert H Sweitzer, DeKang Shen, and GuanLi Wu. In vitro studies of a new thrombus-specific ultrasound contrast agent. *The American journal of cardiology*, 81(12):58G–61G, 1998.

[231] Mario Meza, Yigal Greener, Roberta Hunt, Bret Perry, Susan Revall, Wayne Barbee, Joseph P Murgo, and Jorge Cheirif. Myocardial contrast echocardiography: reliable, safe, and efficacious myocardial perfusion assessment after intravenous injections of a new echocardiographic contrast agent. *American heart journal*, 132(4):871–881, 1996.

[232] Michel Schneider, Marcel Arditi, Marie-Bernadette Barrau, Jean Brochot, Anne Broillet, Roger Ventrone, and Feng Yan. Br1: a new ultrasonographic contrast agent based on sulfur hexafluoride-filled microbubbles. *Investigative radiology*, 30(8):451–457, 1995.

[233] Hayat Alkan-Onyuksel, Sasha M Demos, Gregory M Lanza, Michael J Vonesh, Melvin E Klegerman, Bonnie J Kane, Jer Kuszak, and David D

McPherson. Development of inherently echogenic liposomes as an ultrasonic contrast agent. *Journal of pharmaceutical sciences*, 85(5):486–490, 1996.

[234] Margaret A Wheatley, Beth Schrope, and Peng Shen. Contrast agents for diagnostic ultrasound: development and evaluation of polymer-coated microbubbles. *Biomaterials*, 11(9):713–717, 1990.

[235] BB Goldberg, JB Liu, PN Burns, DA Merton, and F Forsberg. Galactose-based intravenous sonographic contrast agent: experimental studies. *Journal of ultrasound in medicine*, 12(8):463–470, 1993.

[236] MW Keller, SB Feinstein, and DD Watson. Successful left ventricular opacification following peripheral venous injection of sonicated contrast agent: an experimental evaluation. *American heart journal*, 114(3):570–575, 1987.

[237] Raymond Gramiak and Pravin M Shah. Echocardiography of the aortic root. *Investigative radiology*, 3(5):356–366, 1968.

[238] Shengping Qin, Charles F Caskey, and Katherine W Ferrara. Ultrasound contrast microbubbles in imaging and therapy: physical principles and engineering. *Physics in medicine & biology*, 54(6):R27, 2009.

[239] Emilio Quaia. Classification and safety of microbubble-based contrast agents. In *Contrast media in ultrasonography*, pages 3–14. Springer, 2005.

[240] Philippe Marmottant, Sander Van Der Meer, Marcia Emmer, Michel Versluis, Nico De Jong, Sascha Hilgenfeldt, and Detlef Lohse. A model for large amplitude oscillations of coated bubbles accounting for buckling and rupture. *The Journal of the Acoustical Society of America*, 118(6):3499–3505, 2005.

[241] Israelachvili Jacob. *Molecular and surface forces*. Academic Press, 1997.

[242] Katsuro Tachibana, Toshiki Uchida, Koichi Ogawa, Nobuya Yamashita, and Kazuo Tamura. Induction of cell-membrane porosity by ultrasound. *The Lancet*, 353(9162):1409, 1999.

[243] Klazina Kooiman, Miranda Foppen-Harteveld, Antonius FW van der Steen, and Nico de Jong. Sonoporation of endothelial cells by vibrating targeted microbubbles. *Journal of controlled release*, 154(1):35–41, 2011.

[244] Zhenzhen Fan, Haiyan Liu, Michael Mayer, and Cheri X Deng. Spatiotemporally controlled single cell sonoporation. *Proceedings of the National Academy of Sciences*, 109(41):16486–16491, 2012.

[245] Yuanyuan Qiu, Yi Luo, Yanli Zhang, Weicheng Cui, Dong Zhang, Junru Wu, Junfeng Zhang, and Juan Tu. The correlation between acoustic cavitation and sonoporation involved in ultrasound-mediated dna transfection with polyethylenimine (pei) in vitro. *Journal of Controlled Release*, 145(1):40–48, 2010.

[246] William J Greenleaf, Mark E Bolander, Gobinda Sarkar, Mary B Goldring, and James F Greenleaf. Artificial cavitation nuclei significantly enhance acoustically induced cell transfection. *Ultrasound in medicine & biology*, 24(4):587–595, 1998.

[247] Paul Prentice, Alfred Cuschieri, Kishan Dholakia, Mark Prausnitz, and Paul Campbell. Membrane disruption by optically controlled microbubble cavitation. *Nature physics*, 1(2):107–110, 2005.

[248] Bernadet DM Meijering, Lynda JM Juffermans, Annemieke van Wamel, Rob H Henning, Inge S Zuhorn, Marcia Emmer, Amanda MG Versteilen, Walter J Paulus, Wiek H van Gilst, Klazina Kooiman, et al. Ultrasound and microbubble-targeted delivery of macromolecules is regulated by induction of endocytosis and pore formation. *Circulation research*, 104(5):679–687, 2009.

[249] Cheri X Deng, Fred Sieling, Hua Pan, and Jianmin Cui. Ultrasound-induced cell membrane porosity. *Ultrasound in medicine & biology*, 30(4):519–526, 2004.

[250] Boris Krasovitski, Victor Frenkel, Shy Shoham, and Eitan Kimmel. Intramembrane cavitation as a unifying mechanism for ultrasound-induced bioeffects. *Proceedings of the National Academy of Sciences*, 108(8):3258–3263, 2011.

[251] Hong Chen, Wayne Kreider, Andrew A Brayman, Michael R Bailey, and Thomas J Matula. Blood vessel deformations on microsecond time scales by ultrasonic cavitation. *Physical review letters*, 106(3):034301, 2011.

[252] Charles F Caskey, Susanne M Stieger, Shengping Qin, Paul A Dayton, and Katherine W Ferrara. Direct observations of ultrasound microbubble contrast agent interaction with the microvessel wall. *The Journal of the Acoustical Society of America*, 122(2):1191–1200, 2007.

[253] Susanne M Stieger, Charles F Caskey, Roger H Adamson, Shengping Qin, Fitz-Roy E Curry, Erik R Wisner, and Katherine W Ferrara. Enhancement of vascular permeability with low-frequency contrast-enhanced ultrasound in the chorioallantoic membrane model. *Radiology*, 243(1):112–121, 2007.

[254] Bernd Nilius and GUY Droogmans. Ion channels and their functional role in vascular endothelium. *Physiological reviews*, 81(4):1415–1459, 2001.

[255] Srinivas Ghatta, Deepthi Nimmagadda, Xiaoping Xu, and Stephen T O'Rourke. Large-conductance, calcium-activated potassium channels: structural and functional implications. *Pharmacology & therapeutics*, 110(1):103–116, 2006.

[256] Lynda JM Juffermans, Otto Kamp, Pieter A Dijkmans, Cees A Visser, and Rene JP Musters. Low-intensity ultrasound-exposed microbubbles provoke local hyperpolarization of the cell membrane via activation of bkca channels. *Ultrasound in medicine & biology*, 34(3):502–508, 2008.

[257] Yun Zhou, Ronald E Kumon, Cheri X Deng, and Jianmin Cui. The size of sonoporation pores on the cell membrane. In *2008 IEEE Ultrasonics Symposium*, pages 558–561. IEEE, 2008.

[258] PF Costa, Mg G Emilio, PL Fernandes, H Gil Ferreira, and K Gil Ferreira. Determination of ionic permeability coefficients of the plasma membrane of xenopus laevis oocytes under voltage clamp. *The Journal of physiology*, 413(1):199–211, 1989.

[259] Annemieke Van Wamel, Klazina Kooiman, Miranda Harteveld, Marcia Emmer, J Folkert, Michel Versluis, and Nico De Jong. Vibrating

microbubbles poking individual cells: drug transfer into cells via sonoporation. *Journal of controlled release*, 112(2):149–155, 2006.

[260] Sophie Mehier-Humbert, Thierry Bettinger, Feng Yan, and Richard H Guy. Plasma membrane poration induced by ultrasound exposure: implication for drug delivery. *Journal of controlled release*, 104(1):213–222, 2005.

[261] Annemieke van Wamel, Ayache Bouakaz, Bert Bernard, Folkert ten Cate, and Nico de Jong. Radionuclide tumour therapy with ultrasound contrast microbubbles. *Ultrasonics*, 42(1-9):903–906, 2004.

[262] Manabu Kinoshita and Kullervo Hynynen. Intracellular delivery of bak bh3 peptide by microbubble-enhanced ultrasound. *Pharmaceutical research*, 22(5):716–720, 2005.

[263] Isao Kondo, Koji Ohmori, Akira Oshita, Hiroto Takeuchi, Sachiko Fuke, Kaori Shinomiya, Takahisa Noma, Tsunetatsu Namba, and Masakazu Kohno. Treatment of acute myocardial infarction by hepatocyte growth factor gene transfer: the first demonstration of myocardial transfer of a "functional" gene using ultrasonic microbubble destruction. *Journal of the American College of Cardiology*, 44(3):644–653, 2004.

[264] Sayan Mullick Chowdhury, Lotfi Abou-Elkacem, Taehwa Lee, Jeremy Dahl, and Amelie M Lutz. Ultrasound and microbubble mediated therapeutic delivery: Underlying mechanisms and future outlook. *Journal of Controlled Release*, 326:75–90, 2020.

[265] Evan C Unger, Terry Onichi Matsunaga, Thomas McCreery, Patricia Schumann, Robert Sweitzer, and Rachel Quigley. Therapeutic applications of microbubbles. *European journal of Radiology*, 42(2):160–168, 2002.

[266] Sophie Hernot and Alexander L Klibanov. Microbubbles in ultrasound-triggered drug and gene delivery. *Advanced drug delivery reviews*, 60(10):1153–1166, 2008.

[267] J-M Escoffre, A Novell, Sophie Serriere, Thierry Lecomte, and Ayache Bouakaz. Irinotecan delivery by microbubble-assisted ultrasound: in

vitro validation and a pilot preclinical study. *Molecular pharmaceutics*, 10(7):2667–2675, 2013.

[268] Peter Hauff, Stefanie Seemann, Regina Reszka, Marcus Schultze-Mosgau, Michael Reinhardt, Tivadar Buzasi, Thomas Plath, Stefan Rosewicz, and Michael Schirner. Evaluation of gas-filled microparticles and sonoporation as gene delivery system: feasibility study in rodent tumor models. *Radiology*, 236(2):572–578, 2005.

[269] Thierry Bettinger and François Tranquart. Design of microbubbles for gene/drug delivery. *Therapeutic Ultrasound*, pages 191–204, 2016.

[270] Mark A Borden, Charles F Caskey, Erika Little, Robert J Gillies, and Katherine W Ferrara. Dna and polylysine adsorption and multilayer construction onto cationic lipid-coated microbubbles. *Langmuir*, 23(18):9401–9408, 2007.

[271] Evan C Unger, Thomas P McCreery, Robert H Sweitzer, Veronica E Caldwell, and Yunqiu Wu. Acoustically active lipospheres containing paclitaxel: a new therapeutic ultrasound contrast agent. *Investigative radiology*, 33(12):886–892, 1998.

[272] Azadeh Kheirolomoom, Paul A Dayton, Aaron FH Lum, Erika Little, Eric E Paoli, Hairong Zheng, and Katherine W Ferrara. Acoustically-active microbubbles conjugated to liposomes: characterization of a proposed drug delivery vehicle. *Journal of Controlled Release*, 118(3):275–284, 2007.

[273] Bart Geers, Ine Lentacker, Niek N Sanders, Joseph Demeester, Stephen Meairs, and Stefaan C De Smedt. Self-assembled liposome-loaded microbubbles: The missing link for safe and efficient ultrasound triggered drug-delivery. *Journal of controlled release*, 152(2):249–256, 2011.

[274] Patricia A Schumann, Jonathan P Christiansen, Rachel M Quigley, Thomas P McCreery, Robert H Sweitzer, Evan C Unger, Jonathan R Lindner, and Terry O Matsunaga. Targeted-microbubble binding selectively to gpiib iiia receptors of platelet thrombi. *Investigative radiology*, 37(11):587–593, 2002.

[275] A Lawrie, AF Brisken, SE Francis, DC Cumberland, DC Crossman, and CM Newman. Microbubble-enhanced ultrasound for vascular gene delivery. *Gene therapy*, 7(23):2023–2027, 2000.

[276] Masahiko Takahashi, Kanta Kido, Atsuko Aoi, Hiroshi Furukawa, Masao Ono, and Tetsuya Kodama. Spinal gene transfer using ultrasound and microbubbles. *Journal of controlled release*, 117(2):267–272, 2007.

[277] Klazina Kooiman, Silke Roovers, Simone AG Langeveld, Robert T Kleven, Heleen Dewitte, Meaghan A O'Reilly, Jean-Michel Escoffre, Ayache Bouakaz, Martin D Verweij, Kullervo Hynynen, et al. Ultrasound-responsive cavitation nuclei for therapy and drug delivery. *Ultrasound in medicine & biology*, 46(6):1296–1325, 2020.

[278] Hong Yuan, Haiqiang Hu, Jindong Sun, Mingjuan Shi, Huamin Yu, Cairong Li, YU Sun, Zhijian Yang, and Robert M Hoffman. Ultrasound microbubble delivery targeting intraplaque neovascularization inhibits atherosclerotic plaque in an apoe-deficient mouse model. *in vivo*, 32(5):1025–1032, 2018.

[279] Ying-Zheng Zhao, Ming Zhang, Ho Lun Wong, Xin-Qiao Tian, Lei Zheng, Xi-Chong Yu, Fu-Rong Tian, Kai-Li Mao, Zi-Liang Fan, Pian-Pian Chen, et al. Prevent diabetic cardiomyopathy in diabetic rats by combined therapy of afgf-loaded nanoparticles and ultrasound-targeted microbubble destruction technique. *Journal of Controlled Release*, 223:11–21, 2016.

[280] Lijun Qian, Barsha Thapa, Jian Hong, Yanmei Zhang, Menglin Zhu, Ming Chu, Jing Yao, and Di Xu. The present and future role of ultrasound targeted microbubble destruction in preclinical studies of cardiac gene therapy. *Journal of thoracic disease*, 10(2):1099, 2018.

[281] Cedric M Panje, David S Wang, and Jürgen K Willmann. Ultrasound and microbubble–mediated gene delivery in cancer: Progress and perspectives. *Investigative radiology*, 48(11):755–769, 2013.

[282] Wayne M Moreau. *Semiconductor lithography: principles, practices, and materials*. Springer Science & Business Media, 2012.

[283] Andréas Manz, N Graber, and H áM Widmer. Miniaturized total chemical analysis systems: a novel concept for chemical sensing. *Sensors and actuators B: Chemical*, 1(1-6):244–248, 1990.

[284] Stephen C Terry, John H Jerman, and James B Angell. A gas chromatographic air analyzer fabricated on a silicon wafer. *IEEE transactions on electron devices*, 26(12):1880–1886, 1979.

[285] A Manz, Y Miyahara, J Miura, Y Watanabe, H Miyagi, and K Sato. Design of an open-tubular column liquid chromatograph using silicon chip technology. *Sensors and actuators B: Chemical*, 1(1-6):249–255, 1990.

[286] Antonio Francesko, Vanessa F Cardoso, and Senentxu Lanceros-Méndez. Lab-on-a-chip technology and microfluidics. In *Microfluidics for Pharmaceutical Applications*, pages 3–36. Elsevier, 2019.

[287] P Abgrall and AM Gue. Lab-on-chip technologies: making a microfluidic network and coupling it into a complete microsystem—a review. *Journal of micromechanics and microengineering*, 17(5):R15, 2007.

[288] Younan Xia and George M Whitesides. Soft lithography. *Annual review of materials science*, 28(1):153–184, 1998.

[289] Janelle R Anderson, Daniel T Chiu, Rebecca J Jackman, Oksana Cherniavskaya, J Cooper McDonald, Hongkai Wu, Sue H Whitesides, and George M Whitesides. Fabrication of topologically complex three-dimensional microfluidic systems in pdms by rapid prototyping. *Analytical chemistry*, 72(14):3158–3164, 2000.

[290] J Cooper McDonald, David C Duffy, Janelle R Anderson, Daniel T Chiu, Hongkai Wu, Olivier JA Schueller, and George M Whitesides. Fabrication of microfluidic systems in poly (dimethylsiloxane). *ELECTROPHORESIS: An International Journal*, 21(1):27–40, 2000.

[291] Emmanuel Delamarche, Andre Bernard, Heinz Schmid, Bruno Michel, and Hans Biebuyck. Patterned delivery of immunoglobulins to surfaces using microfluidic networks. *Science*, 276(5313):779–781, 1997.

[292] Hou-Pu Chou, Charles Spence, Axel Scherer, and Stephen Quake. A microfabricated device for sizing and sorting dna molecules. *Proceedings of the National Academy of Sciences*, 96(1):11–13, 1999.

[293] Samuel K Sia and George M Whitesides. Microfluidic devices fabricated in poly (dimethylsiloxane) for biological studies. *Electrophoresis*, 24(21):3563–3576, 2003.

[294] Nikin Patel, Robert Padera, Giles HW Sanders, Scott M Cannizzaro, Martyn C Davies, Robert Langer, Clive J Roberts, Saul JB Tendler, Philip M Williams, and Kevin M Shakesheff. Spatially controlled cell engineering on biodegradable polymer surfaces. *The FASEB journal*, 12(14):1447–1454, 1998.

[295] Robert H Carlson, Christopher V Gabel, Shirley S Chan, Robert H Austin, James P Brody, and James W Winkelman. Self-sorting of white blood cells in a lattice. *Physical review letters*, 79(11):2149, 1997.

[296] Walter G Hertlein. Practical photolithography for modern semiconductor production. In *Optical Microlithographic Technology for Integrated Circuit Fabrication and Inspection*, volume 811, pages 48–54. International Society for Optics and Photonics, 1987.

[297] George M Whitesides, Emanuele Ostuni, Shuichi Takayama, Xingyu Jiang, and Donald E Ingber. Soft lithography in biology and biochemistry. *Annual review of biomedical engineering*, 3(1):335–373, 2001.

[298] Dong Qin, Younan Xia, and George M Whitesides. Soft lithography for micro-and nanoscale patterning. *Nature protocols*, 5(3):491, 2010.

[299] Weng Sing Beh, In Tae Kim, Dong Qin, Younan Xia, and George M Whitesides. Formation of patterned microstructures of conducting polymers by soft lithography, and applications in microelectronic device fabrication. *Advanced Materials*, 11(12):1038–1041, 1999.

[300] HOLGER Moritz. High-resolution lithography with projection printing. *IEEE Transactions on Electron Devices*, 26(4):705–710, 1979.

[301] Mordechai Rothschild. Projection optical lithography. *Materials Today*, 8(2):18–24, 2005.

[302] Werayut Srituravanich, Liang Pan, Yuan Wang, Cheng Sun, David B Bogy, and Xiang Zhang. Flying plasmonic lens in the near field for high-speed nanolithography. *Nature nanotechnology*, 3(12):733–737, 2008.

[303] Jianjie Dong, Juan Liu, Guoguo Kang, Jinghui Xie, and Yongtian Wang. Pushing the resolution of photolithography down to 15nm by surface plasmon interference. *Scientific reports*, 4(1):1–6, 2014.

[304] Elisa Mele and Dario Pisignano. Nanobiotechnology: soft lithography. In *Biosilica in Evolution, Morphogenesis, and Nanobiotechnology*, pages 341–358. Springer, 2009.

[305] Younan Xia, Jabez J McClelland, Rajeev Gupta, Dong Qin, Xiao-Mei Zhao, Lydia L Sohn, Robert J Celotta, and George M Whitesides. Replica molding using polymeric materials: A practical step toward nanomanufacturing. *Advanced Materials*, 9(2):147–149, 1997.

[306] Scott Brittain, Karteri Paul, Xiao-Mei Zhao, and George Whitesides. Soft lithography and microfabrication. *Physics World*, 11(5):31, 1998.

[307] Byron D Gates and George M Whitesides. Replication of vertical features smaller than 2 nm by soft lithography. *Journal of the american chemical society*, 125(49):14986–14987, 2003.

[308] Younan Xia, Enoch Kim, Xiao-Mei Zhao, John A Rogers, Mara Prentiss, and George M Whitesides. Complex optical surfaces formed by replica molding against elastomeric masters. *Science*, 273(5273):347–349, 1996.

[309] Eric K Sackmann, Anna L Fulton, and David J Beebe. The present and future role of microfluidics in biomedical research. *Nature*, 507(7491):181–189, 2014.

[310] Jorge Almodóvar, Thomas Crouzier, Šeila Selimović, Thomas Boudou, Ali Khademhosseini, and Catherine Picart. Gradients of physical and biochemical cues on polyelectrolyte multilayer films generated via microfluidics. *Lab on a Chip*, 13(8):1562–1570, 2013.

[311] Daniel T Chiu, Noo Li Jeon, Sui Huang, Ravi S Kane, Christopher J Wargo, Insung S Choi, Donald E Ingber, and George M Whitesides.

Patterned deposition of cells and proteins onto surfaces by using three-dimensional microfluidic systems. *Proceedings of the National Academy of Sciences*, 97(6):2408–2413, 2000.

[312] Eric Gottwald, Stefan Giselbrecht, Caroline Augspurger, Brigitte Lahni, Nina Dambrowsky, Roman Truckenmüller, Volker Piotter, Thomas Gietzelt, Oliver Wendt, Wilhelm Pfleging, et al. A chip-based platform for the in vitro generation of tissues in three-dimensional organization. *Lab on a Chip*, 7(6):777–785, 2007.

[313] Hang Lu, Lily Y Koo, Wechung M Wang, Douglas A Lauffenburger, Linda G Griffith, and Klavs F Jensen. Microfluidic shear devices for quantitative analysis of cell adhesion. *Analytical chemistry*, 76(18):5257–5264, 2004.

[314] Joshua T Morgan, Joshua A Wood, Nihar M Shah, Marissa L Hughbanks, Paul Russell, Abdul I Barakat, and Christopher J Murphy. Integration of basal topographic cues and apical shear stress in vascular endothelial cells. *Biomaterials*, 33(16):4126–4135, 2012.

[315] Musundi B Wabuyele, Sean M Ford, Wieslaw Stryjewski, James Barrow, and Steven A Soper. Single molecule detection of double-stranded dna in poly (methylmethacrylate) and polycarbonate microfluidic devices. *Electrophoresis*, 22(18):3939–3948, 2001.

[316] Stefan Metz, Raphael Holzer, and Philippe Renaud. Polyimide-based microfluidic devices. *Lab on a Chip*, 1(1):29–34, 2001.

[317] Susan LR Barker, Michael J Tarlov, Heather Canavan, James J Hickman, and Laurie E Locascio. Plastic microfluidic devices modified with polyelectrolyte multilayers. *Analytical Chemistry*, 72(20):4899–4903, 2000.

[318] Qiaosheng Pu, Olufemi Oyesanya, Bowlin Thompson, Shantang Liu, and Julio C Alvarez. On-chip micropatterning of plastic (cylic olefin copolymer, coc) microfluidic channels for the fabrication of biomolecule microarrays using photografting methods. *Langmuir*, 23(3):1577–1583, 2007.

[319] Saurabh Vyawahare, Andrew D Griffiths, and Christoph A Merten. Miniaturization and parallelization of biological and chemical assays in microfluidic devices. *Chemistry & biology*, 17(10):1052–1065, 2010.

[320] Rafael Gómez-Sjöberg, Anne A Leyrat, Dana M Pirone, Christopher S Chen, and Stephen R Quake. Versatile, fully automated, microfluidic cell culture system. *Analytical chemistry*, 79(22):8557–8563, 2007.

[321] Luoran Shang, Yao Cheng, and Yuanjin Zhao. Emerging droplet microfluidics. *Chemical reviews*, 117(12):7964–8040, 2017.

[322] Shia-Yen Teh, Robert Lin, Lung-Hsin Hung, and Abraham P Lee. Droplet microfluidics. *Lab on a Chip*, 8(2):198–220, 2008.

[323] Jessamine MK Ng, Irina Gitlin, Abraham D Stroock, and George M Whitesides. Components for integrated poly (dimethylsiloxane) microfluidic systems. *Electrophoresis*, 23(20):3461–3473, 2002.

[324] Noo Li Jeon, Harihara Baskaran, Stephan KW Dertinger, George M Whitesides, Livingston Van De Water, and Mehmet Toner. Neutrophil chemotaxis in linear and complex gradients of interleukin-8 formed in a microfabricated device. *Nature biotechnology*, 20(8):826–830, 2002.

[325] Xinyu Zhang and Michael G Roper. Microfluidic perfusion system for automated delivery of temporal gradients to islets of langerhans. *Analytical chemistry*, 81(3):1162–1168, 2009.

[326] Joong Yull Park, Sung Ju Yoo, Chang Mo Hwang, and Sang-Hoon Lee. Simultaneous generation of chemical concentration and mechanical shear stress gradients using microfluidic osmotic flow comparable to interstitial flow. *Lab on a Chip*, 9(15):2194–2202, 2009.

[327] Monica L Moya, Yu-Hsiang Hsu, Abraham P Lee, Christopher CW Hughes, and Steven C George. In vitro perfused human capillary networks. *Tissue Engineering Part C: Methods*, 19(9):730–737, 2013.

[328] Hanbin Mao, Tinglu Yang, and Paul S Cremer. A microfluidic device with a linear temperature gradient for parallel and combinatorial measurements. *Journal of the American Chemical Society*, 124(16):4432–4435, 2002.

[329] Yung-Ann Chen, Andrew D King, Hsiu-Chen Shih, Chien-Chung Peng, Chueh-Yu Wu, Wei-Hao Liao, and Yi-Chung Tung. Generation of oxygen gradients in microfluidic devices for cell culture using spatially confined chemical reactions. *Lab on a Chip*, 11(21):3626–3633, 2011.

[330] Zhang Lin, Tan Cherng-Wen, Partha Roy, and Dieter Trau. In-situ measurement of cellular microenvironments in a microfluidic device. *Lab on a Chip*, 9(2):257–262, 2009.

[331] Javier Atencia, Jayne Morrow, and Laurie E Locascio. The microfluidic palette: a diffusive gradient generator with spatio-temporal control. *Lab on a Chip*, 9(18):2707–2714, 2009.

[332] Mario Rothbauer, Helene Zirath, and Peter Ertl. Recent advances in microfluidic technologies for cell-to-cell interaction studies. *Lab on a Chip*, 18(2):249–270, 2018.

[333] Rahul Singhvi, Amit Kumar, Gabriel P Lopez, Gregory N Stephanopoulos, DI Wang, George M Whitesides, and Donald E Ingber. Engineering cell shape and function. *Science*, 264(5159):696–698, 1994.

[334] Christopher S Chen, Milan Mrksich, Sui Huang, George M Whitesides, and Donald E Ingber. Geometric control of cell life and death. *Science*, 276(5317):1425–1428, 1997.

[335] Laura E Dike, Christopher S Chen, Milan Mrksich, Joe Tien, George M Whitesides, and Donald E Ingber. Geometric control of switching between growth, apoptosis, and differentiation during angiogenesis using micropatterned substrates. *In Vitro Cellular & Developmental Biology-Animal*, 35(8):441–448, 1999.

[336] Colin L Walsh, Brett M Babin, Rachel W Kasinskas, Jean A Foster, Marissa J McGarry, and Neil S Forbes. A multipurpose microfluidic device designed to mimic microenvironment gradients and develop targeted cancer therapeutics. *Lab on a chip*, 9(4):545–554, 2009.

[337] Kyeonggon Shin, Brett S Klosterhoff, and Bumsoo Han. Characterization of cell-type-specific drug transport and resistance of breast cancers using tumor-microenvironment-on-chip. *Molecular pharmaceutics*, 13(7):2214–2223, 2016.

[338] Stefania Parlato, Giulia Grisanti, Giorgia Sinibaldi, Giovanna Peruzzi, Carlo Massimo Casciola, and Lucia Gabriele. Tumor-on-a-chip platforms to study cancer–immune system crosstalk in the era of immunotherapy. *Lab on a Chip*, 2020.

[339] Sangeeta N Bhatia and Donald E Ingber. Microfluidic organs-on-chips. *Nature biotechnology*, 32(8):760–772, 2014.

[340] Kathrin Herrmann, Francesca Pistollato, and Martin L Stephens. Beyond the 3rs: Expanding the use of human-relevant replacement methods in biomedical research. *ALTEX-Alternatives to animal experimentation*, 36(3):343–352, 2019.

[341] Michael Shin, Kant Matsuda, Osamu Ishii, Hidetomi Terai, Mohammed Kaazempur-Mofrad, Jeffrey Borenstein, Michael Detmar, and Joseph P Vacanti. Endothelialized networks with a vascular geometry in microfabricated poly (dimethyl siloxane). *Biomedical microdevices*, 6(4):269–278, 2004.

[342] Vernella Vickerman, Jennifer Blundo, Seok Chung, and Roger Kamm. Design, fabrication and implementation of a novel multi-parameter control microfluidic platform for three-dimensional cell culture and real-time imaging. *Lab on a Chip*, 8(9):1468–1477, 2008.

[343] Duc-Huy T Nguyen, Sarah C Stapleton, Michael T Yang, Susie S Cha, Colin K Choi, Peter A Galie, and Christopher S Chen. Biomimetic model to reconstitute angiogenic sprouting morphogenesis in vitro. *Proceedings of the National Academy of Sciences*, 110(17):6712–6717, 2013.

[344] Ju Hun Yeon, Hyun Ryul Ryu, Minhwan Chung, Qing Ping Hu, and Noo Li Jeon. In vitro formation and characterization of a perfusable three-dimensional tubular capillary network in microfluidic devices. *Lab on a Chip*, 12(16):2815–2822, 2012.

[345] T Satoh, G Narazaki, R Sugita, H Kobayashi, S Sugiura, and T Kanamori. A pneumatic pressure-driven multi-throughput microfluidic circulation culture system. *Lab on a Chip*, 16(12):2339–2348, 2016.

[346] Hanjoong Jo, Randal O Dull, Theodore M Hollis, and John M Tarbell. Endothelial albumin permeability is shear dependent, time dependent,

and reversible. *American Journal of Physiology-Heart and Circulatory Physiology*, 260(6):H1992–H1996, 1991.

[347] Venkatraman Siddharthan, Yuri V Kim, Suyi Liu, and Kwang Sik Kim. Human astrocytes/astrocyte-conditioned medium and shear stress enhance the barrier properties of human brain microvascular endothelial cells. *Brain research*, 1147:39–50, 2007.

[348] Sudhir P Deosarkar, Balabhaskar Prabhakarpandian, Bin Wang, Joel B Sheffield, Barbara Krynska, and Mohammad F Kiani. A novel dynamic neonatal blood-brain barrier on a chip. *PloS one*, 10(11), 2015.

[349] Tori B Terrell-Hall, Amanda G Ammer, Jessica IG Griffith, and Paul R Lockman. Permeability across a novel microfluidic blood-tumor barrier model. *Fluids and Barriers of the CNS*, 14(1):1–10, 2017.

[350] Yuan Tang, Fariborz Soroush, Shuang Sun, Elisabetta Liverani, Jordan C Langston, Qingliang Yang, Laurie E Kilpatrick, and Mohammad F Kiani. Protein kinase c-delta inhibition protects blood-brain barrier from sepsis-induced vascular damage. *Journal of neuroinflammation*, 15(1):1–12, 2018.

[351] Jackson G DeStefano, Zinnia S Xu, Ashley J Williams, Nahom Yimam, and Peter C Searson. Effect of shear stress on ipsc-derived human brain microvascular endothelial cells (dhbmecs). *Fluids and Barriers of the CNS*, 14(1):1–15, 2017.

[352] Mandy B Esch, David J Post, Michael L Shuler, and Tracy Stokol. Characterization of in vitro endothelial linings grown within microfluidic channels. *Tissue Engineering Part A*, 17(23-24):2965–2971, 2011.

[353] John P Reeves and Robert M Dowben. Formation and properties of thin-walled phospholipid vesicles. *Journal of cellular physiology*, 73(1):49–60, 1969.

[354] Peter Walde, Katia Cosentino, Helen Engel, and Pasquale Stano. Giant vesicles: preparations and applications. *ChemBioChem*, 11(7):848–865, 2010.

[355] Dirk van Swaay and Andrew DeMello. Microfluidic methods for forming liposomes. *Lab on a Chip*, 13(5):752–767, 2013.

[356] JN Israelachvili, S Marčelja, and Roger G Horn. Physical principles of membrane organization. *Quarterly reviews of biophysics*, 13(2):121–200, 1980.

[357] X Armengol and J Estelrich. Physical stability of different liposome compositions obtained by extrusion method. *Journal of microencapsulation*, 12(5):525–535, 1995.

[358] Jacob N Israelachvili and D John Mitchell. A model for the packing of lipids in bilayer membranes. *Biochimica et Biophysica Acta (BBA)-Biomembranes*, 389(1):13–19, 1975.

[359] Takayuki Kitagawa, Keizo Inoue, and Shoshichi Nojima. Properties of liposomal membranes containing lysolecithin. *The Journal of Biochemistry*, 79(6):1123–1133, 1976.

[360] Yunko Lee and Sunney I Chan. Effect of lysolecithin on the structure and permeability of lecithin bilayer vesicles. *Biochemistry*, 16(7):1303–1309, 1977.

[361] G Vanlerberghe, RM Handjani-Vila, and A Ribier. Les niosomes, une nouvelle famille de vesicules a'base d'amphiphiles non ioniques. *Colloques nationaux du CNRS*, 938:304, 1978.

[362] LF Uchegbu. *Synthetic surfactant vesicles: niosomes and other non-phospholipid vesicular systems*. CRC Press, 2000.

[363] Dennis E Discher and Adi Eisenberg. Polymer vesicles. *Science*, 297(5583):967–973, 2002.

[364] Jing Li, Xuling Wang, Ting Zhang, Chunling Wang, Zhenjun Huang, Xiang Luo, and Yihui Deng. A review on phospholipids and their main applications in drug delivery systems. *Asian journal of pharmaceutical sciences*, 10(2):81–98, 2015.

[365] WW Sułkowski, D Pentak, K Nowak, and A Sułkowska. The influence of temperature, cholesterol content and ph on liposome stability. *Journal of molecular structure*, 744:737–747, 2005.

[366] Peter Walde and Sosaku Ichikawa. Enzymes inside lipid vesicles: preparation, reactivity and applications. *Biomolecular engineering*, 18(4):143–177, 2001.

[367] HeeTae Jung, B Coldren, JA Zasadzinski, DJ Iampietro, and EW Kaler. The origins of stability of spontaneous vesicles. *Proceedings of the national academy of sciences*, 98(4):1353–1357, 2001.

[368] A Gomez-Hens and JM Fernandez-Romero. Analytical methods for the control of liposomal delivery systems. *TrAC Trends in Analytical Chemistry*, 25(2):167–178, 2006.

[369] Charles F Kulpa and Thomas J Tinghitella. Encapsulation of polyuridylic acid in phospholipid vesicles. *Life sciences*, 19(12):1879–1888, 1976.

[370] Pheakdey Yun, Sakamon Devahastin, and Naphaporn Chiewchan. Microstructures of encapsulates and their relations with encapsulation efficiency and controlled release of bioactive constituents: A review. *Comprehensive Reviews in Food Science and Food Safety*, 20(2):1768–1799, 2021.

[371] Fumiyoshi Ishii and Yoshihide Nagasaka. Simple and convenient method for estimation of marker entrapped in liposomes. *Journal of dispersion science and technology*, 22(1):97–101, 2001.

[372] Markus Müller, Stefan Mackeben, and Christel C Müller-Goymann. Physicochemical characterisation of liposomes with encapsulated local anaesthetics. *International journal of pharmaceutics*, 274(1-2):139–148, 2004.

[373] Arthur R Nicholas, Matthew J Scott, Nigel I Kennedy, and Malcolm N Jones. Effect of grafted polyethylene glycol (peg) on the size, encapsulation efficiency and permeability of vesicles. *Biochimica et Biophysica Acta (BBA)-Biomembranes*, 1463(1):167–178, 2000.

[374] SB Kulkarni, GV Betageri, and M Singh. Factors affecting microencapsulation of drugs in liposomes. *Journal of microencapsulation*, 12(3):229–246, 1995.

[375] Demetrios Papahadjopoulos and N Miller. Phospholipid model membranes. i. structural characteristics of hydrated liquid crystals. *Biochimica et Biophysica Acta (BBA)-Biomembranes*, 135(4):624–638, 1967.

[376] Kanta Tsumoto, Hideki Matsuo, Masahiro Tomita, and Tetsuro Yoshimura. Efficient formation of giant liposomes through the gentle hydration of phosphatidylcholine films doped with sugar. *Colloids and Surfaces B: Biointerfaces*, 68(1):98–105, 2009.

[377] Ken-ichirou Akashi, Hidetake Miyata, Hiroyasu Itoh, and Kazuhiko Kinosita Jr. Preparation of giant liposomes in physiological conditions and their characterization under an optical microscope. *Biophysical journal*, 71(6):3242–3250, 1996.

[378] Hannah Stein, Susann Spindler, Navid Bonakdar, Chun Wang, and Vahid Sandoghdar. Production of isolated giant unilamellar vesicles under high salt concentrations. *Frontiers in physiology*, 8:63, 2017.

[379] Miglena I Angelova and Dimiter S Dimitrov. Liposome electroformation. *Faraday discussions of the Chemical Society*, 81:303–311, 1986.

[380] Lorenzo Capretto, Dario Carugo, Stefania Mazzitelli, Claudio Nastruzzi, and Xunli Zhang. Microfluidic and lab-on-a-chip preparation routes for organic nanoparticles and vesicular systems for nanomedicine applications. *Advanced drug delivery reviews*, 65(11-12):1496–1532, 2013.

[381] Feng Kong, Xu Zhang, and Mingtan Hai. Microfluidics fabrication of monodisperse biocompatible phospholipid vesicles for encapsulation and delivery of hydrophilic drug or active compound. *Langmuir*, 30(13):3905–3912, 2014.

[382] K Kuribayashi, G Tresset, Ph Coquet, H Fujita, and S Takeuchi. Electroformation of giant liposomes in microfluidic channels. *Measurement science and technology*, 17(12):3121, 2006.

[383] Yu-Cheng Lin, Min Li, Yu-Tsung Wang, Tzung-Heng Lai, Jen-Ta Chiang, and Keng-Shiang Huang. A new method for the preparation of self-assembled phospholipid microtubes using microfluidic technology. In *The 13th International Conference on Solid-State Sensors, Actuators and Microsystems, 2005. Digest of Technical Papers. TRANSDUCERS'05.*, volume 2, pages 1592–1595. IEEE, 2005.

[384] Yu-Cheng Lin, Keng-Shiang Huang, Jen-Ta Chiang, Chih-Hui Yang, and Tzung-Heng Lai. Manipulating self-assembled phospholipid microtubes using microfluidic technology. *Sensors and actuators b: chemical*, 117(2):464–471, 2006.

[385] Petra S Dittrich, Martin Heule, Philippe Renaud, and Andreas Manz. On-chip extrusion of lipid vesicles and tubes through microsized apertures. *Lab on a Chip*, 6(4):488–493, 2006.

[386] Andreas Jahn, Wyatt N Vreeland, Michael Gaitan, and Laurie E Locascio. Controlled vesicle self-assembly in microfluidic channels with hydrodynamic focusing. *Journal of the American Chemical Society*, 126(9):2674–2675, 2004.

[387] M Mijajlovic, D Wright, Vladimir Zivkovic, JX Bi, and MJ Biggs. Microfluidic hydrodynamic focusing based synthesis of popc liposomes for model biological systems. *Colloids and surfaces B: biointerfaces*, 104:276–281, 2013.

[388] Kei Funakoshi, Hiroaki Suzuki, and Shoji Takeuchi. Formation of giant lipid vesiclelike compartments from a planar lipid membrane by a pulsed jet flow. *Journal of the American chemical society*, 129(42):12608–12609, 2007.

[389] Jeanne C Stachowiak, David L Richmond, Thomas H Li, Allen P Liu, Sapun H Parekh, and Daniel A Fletcher. Unilamellar vesicle formation and encapsulation by microfluidic jetting. *Proceedings of the national academy of sciences*, 105(12):4697–4702, 2008.

[390] Yung-Chieh Tan, Kanaka Hettiarachchi, Maria Siu, Yen-Ru Pan, and Abraham Phillip Lee. Controlled microfluidic encapsulation of cells, proteins, and microbeads in lipid vesicles. *Journal of the American Chemical Society*, 128(17):5656–5658, 2006.

[391] Peichi C Hu, Su Li, and Noah Malmstadt. Microfluidic fabrication of asymmetric giant lipid vesicles. *ACS applied materials & interfaces*, 3(5):1434–1440, 2011.

[392] Sandro Matosevic and Brian M Paegel. Stepwise synthesis of giant unilamellar vesicles on a microfluidic assembly line. *Journal of the American Chemical Society*, 133(9):2798–2800, 2011.

[393] Sadao Ota, Satoko Yoshizawa, and Shoji Takeuchi. Microfluidic formation of monodisperse, cell-sized, and unilamellar vesicles. *Angewandte chemie international edition*, 48(35):6533–6537, 2009.

[394] Siddharth Deshpande, Yaron Caspi, Anna EC Meijering, and Cees Dekker. Octanol-assisted liposome assembly on chip. *Nature communications*, 7(1):1–9, 2016.

[395] Julien Petit, Ingmar Polenz, Jean-Christophe Baret, Stephan Herminghaus, and Oliver Bäumchen. Vesicles-on-a-chip: A universal microfluidic platform for the assembly of liposomes and polymersomes. *The European Physical Journal E*, 39(6):1–6, 2016.

[396] Tobias Foster, Kevin D Dorfman, and H Ted Davis. Giant biocompatible and biodegradable peg–pmcl vesicles and microcapsules by solvent evaporation from double emulsion droplets. *Journal of colloid and interface science*, 351(1):140–150, 2010.

[397] K Karamdad, RV Law, JM Seddon, NJ Brooks, and O Ces. Studying the effects of asymmetry on the bending rigidity of lipid membranes formed by microfluidics. *Chemical Communications*, 52(30):5277–5280, 2016.

[398] Mikhail Kozlov, Mamle Quarmyne, Wei Chen, and Thomas J McCarthy. Adsorption of poly (vinyl alcohol) onto hydrophobic substrates. a general approach for hydrophilizing and chemically activating surfaces. *Macromolecules*, 36(16):6054–6059, 2003.

[399] Srinath Muppalaneni and Hossein Omidian. Polyvinyl alcohol in medicine and pharmacy: a perspective. *J. Dev. Drugs*, 2(3):1–5, 2013.

[400] Marian Weiss, Johannes Patrick Frohnmayer, Lucia Theresa Benk, Barbara Haller, Jan-Willi Janiesch, Thomas Heitkamp, Michael Börsch, Rafael B Lira, Rumiana Dimova, Reinhard Lipowsky, et al. Sequential bottom-up assembly of mechanically stabilized synthetic cells by microfluidics. *Nature materials*, 17(1):89–96, 2018.

[401] Flurin Sturzenegger, Tom Robinson, David Hess, and Petra S Dittrich. Membranes under shear stress: visualization of non-equilibrium domain patterns and domain fusion in a microfluidic device. *Soft Matter*, 12(23):5072–5076, 2016.

[402] Bárbara Herranz-Blanco, Laura R Arriaga, Ermei Mäkilä, Alexandra Correia, Neha Shrestha, Sabiruddin Mirza, David A Weitz, Jarno Salonen, Jouni Hirvonen, and Hélder A Santos. Microfluidic assembly of multistage porous silicon–lipid vesicles for controlled drug release. *Lab on a Chip*, 14(6):1083–1086, 2014.

[403] Nathan M Belliveau, Jens Huft, Paulo JC Lin, Sam Chen, Alex KK Leung, Timothy J Leaver, Andre W Wild, Justin B Lee, Robert J Taylor, Ying K Tam, et al. Microfluidic synthesis of highly potent limit-size lipid nanoparticles for in vivo delivery of sirna. *Molecular Therapy-Nucleic Acids*, 1:e37, 2012.

[404] Igor V Zhigaltsev, Ying K Tam, Alex KK Leung, and Pieter R Cullis. Production of limit size nanoliposomal systems with potential utility as ultra-small drug delivery agents. *Journal of liposome research*, 26(2):96–102, 2016.

[405] Theresa M Allen and Pieter R Cullis. Liposomal drug delivery systems: from concept to clinical applications. *Advanced drug delivery reviews*, 65(1):36–48, 2013.

[406] Oskar Staufer, Silvia Antona, Dennis Zhang, Júlia Csatári, Martin Schröter, Jan-Willi Janiesch, Sebastian Fabritz, Imre Berger, Ilia Platzman, and Joachim P Spatz. Microfluidic production and characterization of biofunctionalized giant unilamellar vesicles for targeted intracellular cargo delivery. *Biomaterials*, 264:120203, 2021.

[407] Kanaka Hettiarachchi, Esra Talu, Marjorie L Longo, Paul A Dayton, and Abraham P Lee. On-chip generation of microbubbles as a practical technology for manufacturing contrast agents for ultrasonic imaging. *Lab on a Chip*, 7(4):463–468, 2007.

[408] Esra Talu, Kanaka Hettiarachchi, Robert L Powell, Abraham P Lee, Paul A Dayton, and Marjorie L Longo. Maintaining monodispersity in a microbubble population formed by flow-focusing. *Langmuir*, 24(5):1745–1749, 2008.

[409] Milad Azarmanesh, Mousa Farhadi, and Pooya Azizian. Double emulsion formation through hierarchical flow-focusing microchannel. *Physics of Fluids*, 28(3):032005, 2016.

[410] Amir Hossein Askari, Mehrzad Shams, and Pierre E Sullivan. Numerical simulation of double emulsion formation in cross-junctional flow-focusing microfluidic device using lattice boltzmann method. *Journal of Dispersion Science and Technology*, 2019.

[411] Douglas B Weibel, Willow R DiLuzio, and George M Whitesides. Microfabrication meets microbiology. *Nature Reviews Microbiology*, 5(3):209–218, 2007.

[412] Arnold Hayer, Lin Shao, Mingyu Chung, Lydia-Marie Joubert, Hee Won Yang, Feng-Chiao Tsai, Anjali Bisaria, Eric Betzig, and Tobias Meyer. Engulfed cadherin fingers are polarized junctional structures between collectively migrating endothelial cells. *Nature cell biology*, 18(12):1311–1323, 2016.

[413] Balabhaskar Prabhakarpandian, Kapil Pant, Robert C Scott, Christopher B Patillo, Daniel Irimia, Mohammad F Kiani, and Shivshankar Sundaram. Synthetic microvascular networks for quantitative analysis of particle adhesion. *Biomedical microdevices*, 10(4):585–595, 2008.

[414] Johannes Schindelin, Ignacio Arganda-Carreras, Erwin Frise, Verena Kaynig, Mark Longair, Tobias Pietzsch, Stephan Preibisch, Curtis Rueden, Stephan Saalfeld, Benjamin Schmid, et al. Fiji: an open-source platform for biological-image analysis. *Nature methods*, 9(7):676–682, 2012.

[415] Klazina Kooiman, Marcia Emmer, Miranda Foppen-Harteveld, Annemieke van Wamel, and Nico de Jong. Increasing the endothelial layer permeability through ultrasound-activated microbubbles. *IEEE transactions on biomedical engineering*, 57(1):29–32, 2009.

[416] Sylvie Lelu, Mercy Afadzi, Sigrid Berg, AKO Åslund, Sverre Helge Torp, Wolfgang Sattler, and C de L Davies. Primary porcine brain endothelial cells as in vitro model to study effects of ultrasound and microbubbles on blood–brain barrier function. *IEEE transactions on ultrasonics, ferroelectrics, and frequency control*, 64(1):281–290, 2016.

[417] KP Ivanov, MK Kalinina, and Yu I Levkovich. Blood flow velocity in capillaries of brain and muscles and its physiological significance. *Microvascular research*, 22(2):143–155, 1981.

[418] Nuria Jiménez, Vincent JD Krouwer, and Jan A Post. A new, rapid and reproducible method to obtain high quality endothelium in vitro. *Cytotechnology*, 65(1):1–14, 2013.

[419] Mouwen Cheng, Fan Li, Tao Han, CH Alfred, and Peng Qin. Effects of ultrasound pulse parameters on cavitation properties of flowing microbubbles under physiologically relevant conditions. *Ultrasonics sonochemistry*, 52:512–521, 2019.

[420] Tatiana Trantidou, Yuval Elani, Edward Parsons, and Oscar Ces. Hydrophilic surface modification of pdms for droplet microfluidics using a simple, quick, and robust method via pva deposition. *Microsystems & nanoengineering*, 3(1):1–9, 2017.